MEMS EARTHWORM:
THE DESIGN AND TESTING OF A BIO-INSPIRED HIGH PRECISION, HIGH SPEED, LONG RANGE PERISTALTIC MICRO-MOTOR

by

Craig Arthur

Submitted in partial fulfilment of the requirements
for the degree of Master of Applied Science

at

Dalhousie University
Halifax, Nova Scotia
November 2010

DALHOUSIE UNIVERSITY

DEPARTMENT OF MECHANICAL ENGINEERING

The undersigned hereby certify that they have read and recommend to the Faculty of Graduate Studies for acceptance a thesis entitled "MEMS EARTHWORM: THE DESIGN AND TESTING OF A BIO-INSPIRED HIGH PRECISION, HIGH SPEED, LONG RANGE PERISTALTIC MICRO-MOTOR" by Craig Arthur in partial fulfilment of the requirements for the degree of Master of Applied Science.

Dated: November 10, 2010

Supervisors: _____

_____

Readers: _____

_____

DALHOUSIE UNIVERSITY

DATE: November 10, 2010

AUTHOR: Craig Arthur

TITLE: MEMS EARTHWORM: THE DESIGN AND TESTING OF A BIO-INSPIRED HIGH PRECISION, HIGH SPEED, LONG RANGE PERISTALTIC MICRO-MOTOR

DEPARTMENT OR SCHOOL: Department of Mechanical Engineering

DEGREE: MASc CONVOCATION: May YEAR: 2011

Table of Contents

List of Tables

List of Figures

List of Equations

Abstract

This work examined the design, fabrication, and testing of a bio-mimetic MEMS earthworm crawler with external actuators. The micro-earthworm consisted of a passive mobile shuttle with two flexible diamond shaped segments; each segment was independently squeezed by a pair of stationary chevron-shaped thermal actuators. By applying a specific sequence of squeezes to the earthworm segments, the shuttle could be driven backwards or forwards. Unlike existing inchworm drives, which use separate clamping and thrusting motors, the earthworm motor applies only clamping forces and lateral thrust is produced by the shuttle's compliant geometry. A study of existing crawler work was performed; to the author's knowledge, this was the first micro-crawler to achieve both clamping force and lateral motion using the same actuators.

The earthworm assembly was fabricated using the POLYMUMPs process, with planar dimensions of 400 μm wide by 800 μm long. The stationary earthworm motors operated within the range of 4-9 V, and 0-10 kHz; these motors provided a maximum shuttle range of motion of 350 μm (~half the size of the device), a maximum shuttle speed of 17,000 μm /s at 10 kHz, and a maximum DC shuttle force of 80 μN. The shuttle speed was found to vary linearly with both input voltage and input frequency; the shuttle force was found to vary linearly with actuator voltage. The tested design had higher force, range, and speed (per device footprint) than most other existing designs.

Future work recommendations included the implementation of multiple motors and a closed loop control system to allow an indefinite range of motion, as well as the investigation of a two degree of freedom crawler.

List of Symbols and Abbreviations

3D	Three-Dimensional
A	Area
BSAC	University of California's Berkley Sensors and Actuators Center
C	Specific heat
CCD	Charge-Coupled Device
CMC	Canadian Microsystems Corporation
D	Needle diameter
DAQ	Data Acquisition Card
DC	Direct Current
DLP	Digital Light Processing
DOF	Degree Of Freedom
DRC	Design Rule Check
E	Young's Modulus
ECD	Electrostatic Comb Drive actuators
ES	Electrostatic
ET	Electrothermal
F	Force output
g	Spacing between electrostatic fingers
HF	Hydrofluoric acid
I	Moment of Inertia
k	Thermal conductivity; Stiffness
L	Arm length
l	Stroke length

L-Edit	Layout-Editor
LCD	Linear Comb Drive
MEMS	Micro Electro Mechanical Systems
MetalMUMPs	A metal-based MEMS process
MUMPs	Multi-User MEMS Process
n	number of electrostatic fingers
N	Number of steps taken
P	Cross-sectional perimeter
PDMS	Polydimethylsiloxane
PGA	Pin Grid Array
PolyMUMPs	A multi-layer polysilicon based MEMS process
PWT	Pulse Width Train
PZ	Piezoelectric
PZT	A piezoelectric material made from lead, zirconium, and titanium
q	Heat transfer rate
R	Resistance
ROI	Region Of Interest
SEM	Scanning Electron Microscope
SMA	Shape-Memory Alloy
SOIMUMPs	A single layer silicon-on-insulator MEMS process
t	Electrostatic finger thickness
T	Temperature
TA	Thermal Actuator
UHMWPE	Ultra-High Molecular Weight Polyethylene
UUV	Unmanned Underwater Remotely-Operated Vehicle

V	Voltage
VI	Labview Virtual Instrument
VTA	Vertical Thermal Actuator
ZIF	Zero Insertion Force
α	Coefficient of thermal expansion
Δ	Displacement
Δ_z	Vertical spacing between the actuator and the chip's substrate
ε	Relative dielectric constant of medium electrostatic array is in; Strain
ε_0	Dielectric constant of a vacuum
ρ	Density
σ	Stress
τ	Thermal time constant

Acknowledgements

So many people have helped me along my academic path that it is truly hard to know where to start. When looking back over the last two years, I have many fond memories: working in the Lab, being a teaching assistant, spending time in the machine shop, and Friday lunch hour discussions (just to name a few).

I would like to thank my supervisors Dr. Hubbard and Dr. Kujath, who gave me the opportunity to pursue my masters, and the guidance to complete it. Dr. Doman and Dr. Ma, my thesis committee, thank you for your time and assistance in helping me to complete my work. A thank you to Neil and Rene, for your invaluable assistance in the Lab; as well Jon, whose electrical knowledge we could not do without. A thank you to Mark, Angus, and Peter, who have helped me ground my academic knowledge with a significant dose of hands-on work. To Morgyn and Sandra; you have helped me more over the years than you will ever know; thank you.

Finally, and perhaps most importantly, to my friends and family for your support during my studies, I cannot thank you enough. Without you, this would never have been possible.

Thank you all.

Chapter 1: Introduction

1.1 Objective

The objectives of this work are to design, build, and test a micro-scale crawler based on the motion of earthworms, specifically:

- To research existing micro-crawler designs.
- To analyze the motion of an earthworm.
- To construct and test a macro-scale model of a robotic crawler based on the motion of an earthworm.
- To design and build a micro-scale earthworm using the MUMPS processes.
- To test the micro-earthworm's performance and compare it to other micro-crawlers

1.1.1 Project Scope

This work includes the basic theory behind the motion of the earthworm crawler, as well as the design and testing of both macro-scale models, and micro-scale prototypes. It focuses on the crawler itself, with no in-depth analysis of the actuators used to drive the crawler. Although the crawler is capable of being driven by any type of MEMS actuator, only chevron-style thermal actuators will be used. This study will show results from testing the crawler's velocity response to a change in either voltage or frequency, as well as its stall force response to a change in voltage.

1.1.2 Author Main Contributions

While a variety of different micro-crawlers designs exist, to the author's knowledge, the micro-crawler discussed here is the first one based on bio-mimicry of the peristaltic motion of the earthworm. While this work is not the first to report a squeezing MEMS micro-motor, it is believed to be the first one which employs the same set of actuators to provide both lateral (clamping), and transverse (forward) motion. The studied micro crawler was compared to other crawlers and found to provide both high force and high speed relative to its size.

1.2 MEMS Background

Micro Electro-Mechanical Systems (MEMS) are small devices that use technology derived from the microelectronics industry to combine electrical and mechanical principles in order to construct and operate physical devices at the μm scale. MEMS have features that are generally in the 1-3 μm range, with entire devices frequently measuring between 10-1000 μm in breadth. MEMS are generally considered planar due to their extremely low device thickness-to-area ratios, with typical material thicknesses measuring from 2-25 μm in thickness.

MEMS technology is quickly becoming an ever more important field, with new MEMS devices finding their way into people's lives every day. These devices are used in everything from high-tech space satellites to cars, communication devices, and even electronic gaming systems. For the space industry, MEMS offers options for re-configuring optical telescope lenses and mirrors while satellites are deployed; in the telecommunications industry, they offer new options for high-speed optical switching. People drive automobiles which employ

MEMS accelerometers to control their airbags, and watch images from DLP televisions and projectors which use arrays of microscopic mirrors to project their images. They send e-mails using their smartphones, which have MEMS devices to automatically change their screen's orientation when they rotate the phone, and print pages using ink-jet printers that rely on MEMS arrays to distribute the ink droplets at the correct moment. The biomedical industry and the military have began deploying fields of MEMS devices to do everything from alerting troops to biological and chemical agents to measuring blood pressures, and developing new ultrasound devices that are smaller and provide better resolution that those currently available. MEMS devices generally fall under two main categories: those of sensors, and those if actuators; sensors produce signals when they detect changes in operating conditions, and actuators provide motion when they are fed a signal.

MEMS devices have many advantages over their macro-scale counterparts. Due to their extremely small size, products using MEMS devices can be made more portable. They can also offer greater redundancy; devices that used to rely on the proper operation of one sensor can now pull data from an array of hundreds of small sensors and not take up any more space. Devices can become fully integrated, with both mechanical structure and electronic circuitry being found on the same small, disposable device. Due to their very small mass, devices constructed at the micro-scale are capable of responding nearly instantaneously when compared with those at the macroscopic scale. They are also cheap; devices are made in batches, meaning thousands upon thousands of devices can be made extremely inexpensively.

Although there are a number of advantages to the use of MEMS devices, they are not without their drawbacks. Due to their planar nature, 3D structures fabricated with MEMS

technology frequently requires post-processing and assembly. MEMS fabrication facilities are extraordinarily complex and expensive to set-up and operate, and thus there are frequently a limited number of fabrication processes available. Due to the same scaling laws that allow incredibly fast response time, MEMS actuators are ruled not by inertial forces, but by frictional forces. Unfortunately, unless they are sealed, they may be susceptible to issues that arise from their environment; a few examples being dust, humidity, air currents, and static electricity.

1.3 Existing Crawler Work

Most micro actuators provide short ranges of motion, typically a only few μm; while this range can be extended using motion amplification mechanisms, this is done at the expense of the output force and is generally limited to ranges of 10's of μm. To provide longer ranges (100's of μm or larger), while maintaining high forces, multiple micro-actuators can be combined into stepping micro-motors that accumulate or 'add up' shorter steps. A wide variety of these stepping micro-motor architectures exist; the two most common types are inchworm motors [1; 2] and the related walking motors [3; 4] which will be discussed in detail below. Other less common modes of locomotion can also be used, such as: impact motors [5], scratch drive motors [6], and frictional motors [7]. These less-common modes will not be discussed within this literature review.

To overcome existing actuator limitations, most long range micro motors utilize a mobile shuttle or carrier which is pushed or pulled by stationary actuators. The actuators are usually placed on both sides of the shuttle and apply longitudinal (pushing/pulling) forces to

move the shuttle. In order to allow a net motion, the actuators must also be able to apply transverse (squeezing) forces for holding and releasing the shuttle during each step. Stepping micro-motors can be classified by the types of forces they apply (transverse or longitudinal) and the actuation order/sequence during each step. Figure 1.3.1 shows simplified motion diagrams of two most common motor types: inchworm and walking motors. The large notched red arrows represent the actuators and the small black arrows show the actuator strokes: solid lines for the power stroke and dashed lines for the retraction stroke.

Figure 1.3.1A shows a schematic of an inchworm motor; it is so called because it mimics the movement of an inchworm with clamping, extending, and releasing phases of the motion. The motor assembly consists of two pairs of actuators: a pair of two-axis (x/y) thrust actuators on the left (they can apply transverse (y) and longitudinal (x) forces), and a pair of single-axis (y) clamping actuators on the right that apply only transverse (squeezing) forces. The most frequently found actuators for these crawlers are thermal and electrostatic, with electrostatic actuation being the more common of the two. The shuttle is moved to the right by activating the thrust actuators transversely and then extending them (strokes are illustrated by black solid arrows); this is followed by squeezing the clamp actuators on the right, and then releasing the thrust actuators completely, the retraction strokes are illustrated by black dashed arrows. Reverse motion is accomplished by reversing the sequence of the steps.

Figure 1.3.1B shows a walking motor; it is so called because it mimics a walking gait where the actuators act like feet traveling on the shuttle. The motor consists of two pairs of actuators: a pair of two-axis (x/y) transverse/longitudinal thrust actuators on the left, and a

mirror-image pair of actuators on the right. The shuttle is moved to the right by squeezing (y) the left actuators, then extending (x) them, followed by squeezing the right actuators, that is succeeded by first releasing the left actuators completely, and after that, extending the right actuators and finally releasing them completely. Reverse motion is accomplished by switching the left/right sequence of the steps. In walking motors there are no dedicated clamp actuators as the gait motion of each actuator includes the clamping in turns.

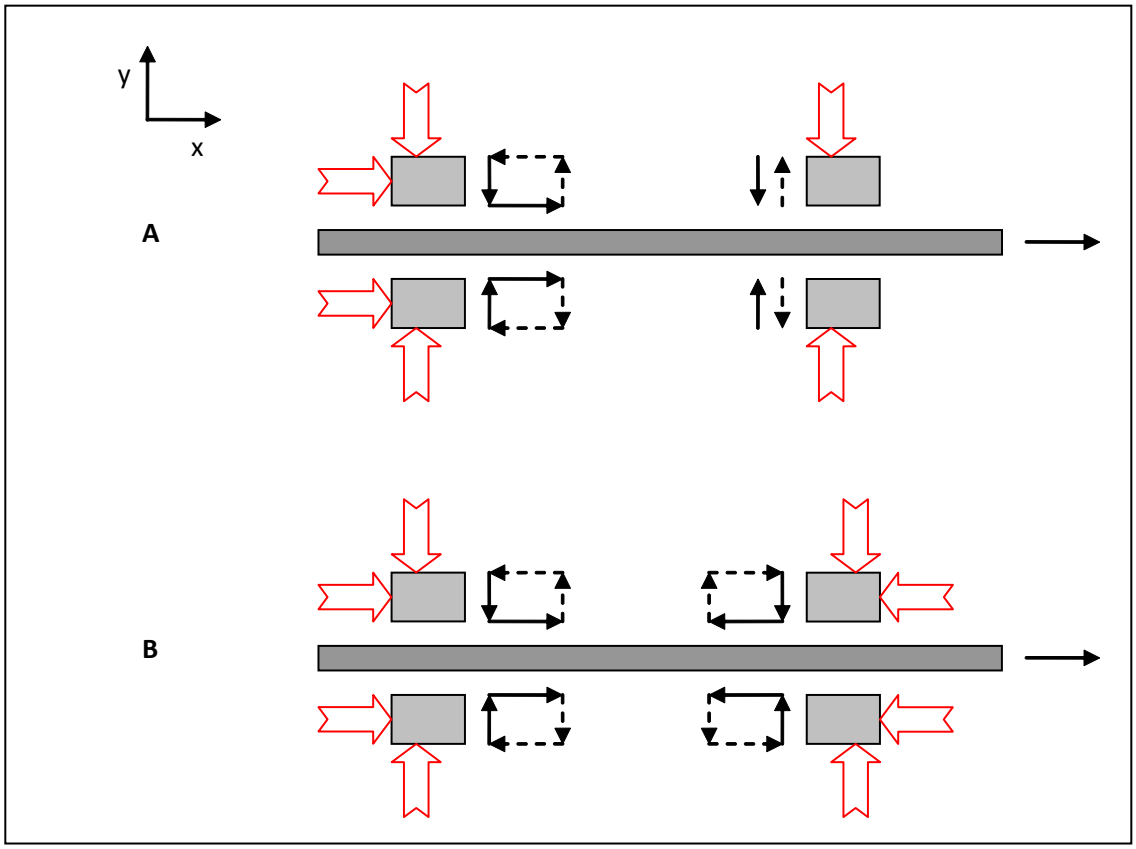

Figure 1.3.1 – Motion Schematic of (A) Inchworm, and (B) Walking Motors

Figure 1.3.1 shows the basic configurations demonstrating the underlying principles of operation, but many different implementations exist: multiple thrust actuators, multiple

clamps, clamping systems which are closed shut by default, etc. In these cases, the step sequencing is different, but the principle of operation is the same. Similarly, some walking motors use alternative gaits or additional redundant feet, but again the principles of motion are the same.

The above motor configurations and many other arrangements use a combination of 1-DOF and 2-DOF actuators. It would be advantageous to have a motor that uses only single-axis actuators; a 1-DOF actuator, such as a clamp, is straightforward and simple to fabricate. However, in order to produce motion in a perpendicular direction to the actuation axis, a more complex shuttle design is required. The two actuator pairs must be coupled through a flexible structure that allows motion in one axis without restricting motion in the other axis.

A number of groups have investigated flexible shuttles for use in micro-motors: Dai *et al.* [8] used parallelograms to change the direction of electrostatic actuator forces by 90 degrees, and Erismis *et al.* [9] fabricated a novel inchworm incorporating diamond shaped compliant structure, as shown in Figure 1.3.2A. The inchworm consisted of a shuttle with a diamond element in the middle, and three pairs of 1-DOF actuators: two pairs of clamping actuators (one on each the left and the right), with lateral-motion actuators in the middle pushing on the diamond feature. When the transverse squeezing forces are applied to the diamond, it is distorted and expands laterally in both directions, producing longitudinal forces. By first clamping the left side of the shuttle, then squeezing the middle diamond, lateral motion to the right is produced. After that, the right clamp is engaged, and both the middle and left actuators are released. With this design, reverse motion is produced by simply reversing the step order. The design has the advantage of using only 1-DOF

actuators that develop solely transverse forces: this design is classified as an inchworm as there is 1 pair of dedicated thrust actuators and 2 pairs of dedicated clamp actuators.

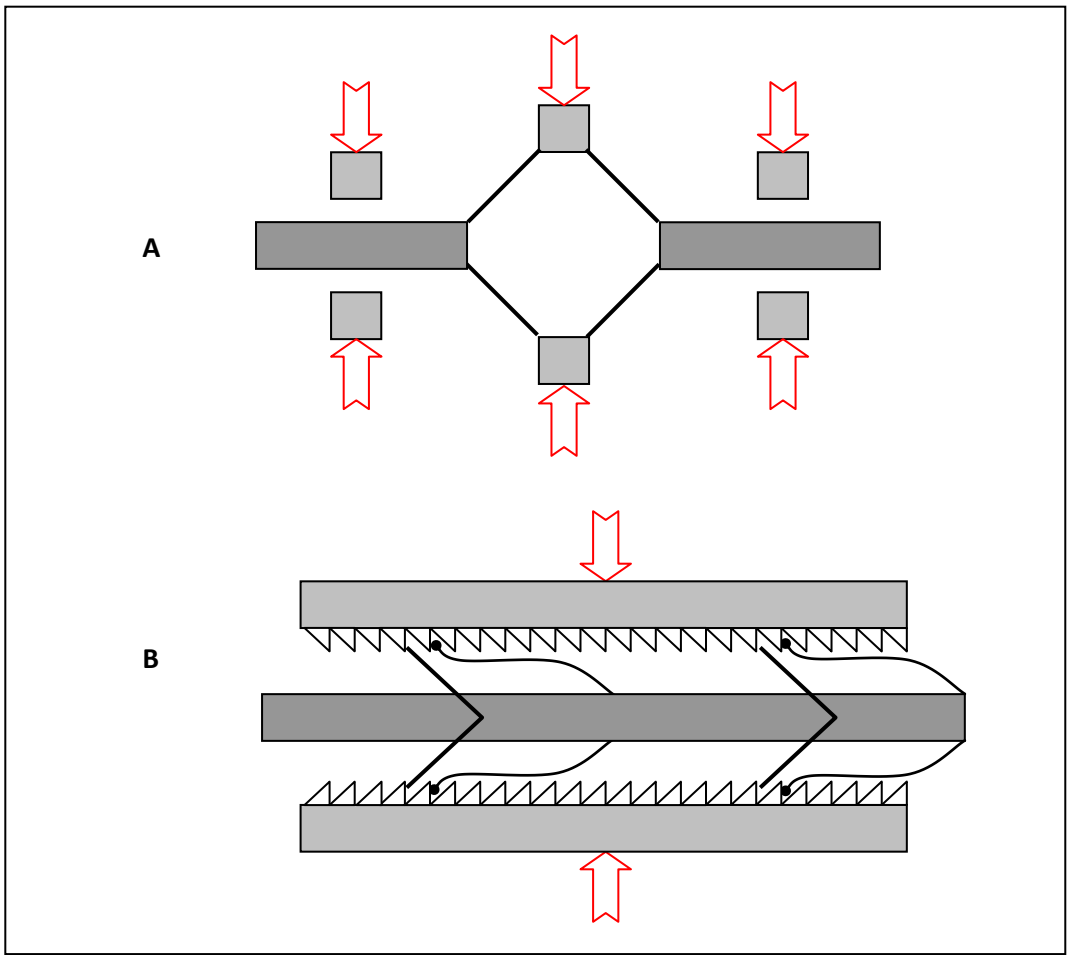

Figure 1.3.2 - Simplified Diagram of Existing Crawler Designs

Pham et al. [10] utilized a one-directional shuttle with a '>' shaped element acting as a half diamond, and a pair of clamping actuators equipped with ratcheting teeth plus a pair of curved pawls attached to the shuttle as shown schematically in Figure 1.3.2B. The doubling

of the basic design elements is necessary to prevent shuttle rotation. The curved pawl arms are more compliant than the '>' shaped element and the arms are at a shallower angle, therefore they do not contribute to actively thrusting the shuttle forward. By squeezing the '>'element the shuttle moves forward more than a single tooth distance until the pawls lock one pitch ahead, and constrain the shuttle's motion backward when the squeezing actuators retract. Therefore, during the actuator retraction the '>'element's arms disengage from the teeth and swing forward as well. While this design is unidirectional, it is of interest because it shows again that single axis actuators can be used to perform both thrust and clamping, rather than using dedicated clamps and dedicated thrust actuators.

A search of existing work that operates on similar principles has been completed, with the results shown in Table 1.3.1; in the table, 'ET' stands for Electrothermal, 'ES' for Electrostatic, and 'PZ' for Piezoelectric. It is often difficult to compare works that are similar in operation, but vary widely in size and shape. Therefore, in order to have a basis for comparison, the devices are first normalized by their size. The resulting device range per unit size is then plotted against device force per unit size (as shown in Figure 1.3.3), and device speed per unit size (as shown in Figure 1.3.4). The specifics of these actuator types will be discussed later in this work. It should be noted that in Table 1.3.1, Figure 1.3.3, and Figure 1.3.4, only the primary author's name is listed for each entry.

Paper	Voltage (V)	Range (µm)	Speed (µm/s)	Force (µN)	Length (µm)	Width (µm)	Area (mm^2)	Type	Range/ Area (m/m^2)	Force/ Area (N/m^2)	Speed/ Area ([m/s]/m^2)
Kwon [3]		50	400	50	1,750	1,750	3.06	ES	16.3	16	131
Brown [7]	3	140	700	138	1,500	500	0.75	ET	187	184	933
Erismis [9]	7	36		30	3,700	1,800	6.66		5.41	4.5	-
Erismis [9]	10	48		50	3,700	1,800	6.66		7.21	7.5	-
Erismis [9]	16	70	300	110	4,800	2,200	10.6		6.63	10	28
Pham [10]	4	225	190		600	800	0.48	ET	167	-	396
Toda [11]	200	600		16,000	20,000	6,000	120	PZ / ES	5.00	133	-
Yeh [12]	33	80		260	2,000	1,500	3.00	ES	26.7	87	-
Yeh [12]		52	4,000		1,500	1,000	1.50	ES	34.7	-	2,667
de Boer [13]	150	140	4,400	450	1,500	600	0.90	ES	156	500	4,889
Sarajlic [14]	55	140	3,600	1,700	412	286	0.12	ES	1,188	14,427	30,552
Tas [15]	40	15		3	500	400	0.20	ES	75.0	15	-

Table 1.3.1 - Comparison of Existing Crawler Designs

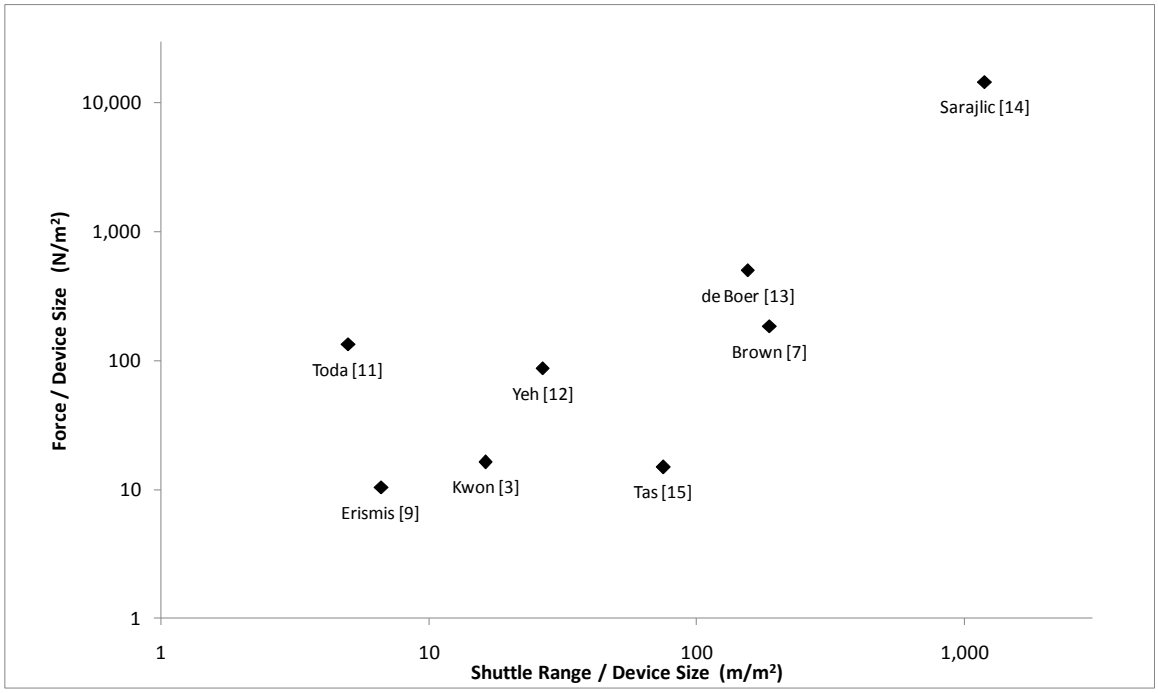

Figure 1.3.3 - Comparison of Existing Crawler Forces

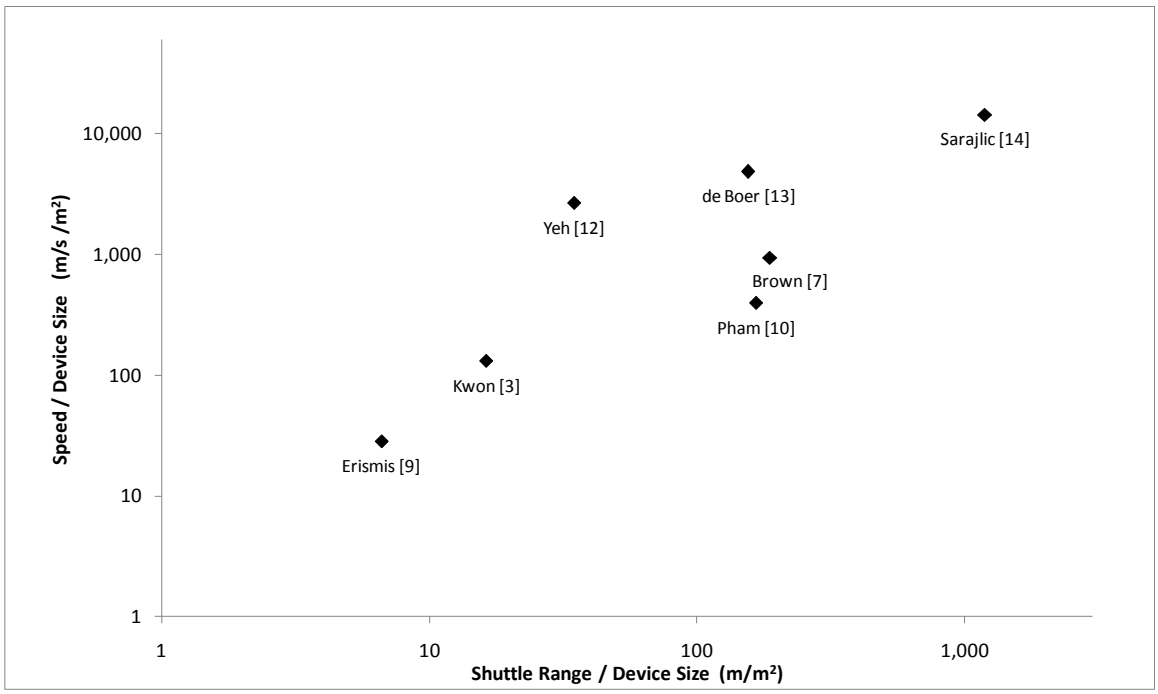

Figure 1.3.4 - Comparison of Existing Crawler Speeds

1.4 Biological Inspiration

The work contained in this thesis was based off of the motion of a common earthworm. This section will explain why more scientists and engineers are turning towards the natural world to solve our problems, and cover the basic locomotive biology of an earthworm.

1.4.1 Biomimicry

A common step in the design of systems and products is for engineers and scientists to look towards other systems that have solved a similar problem. For this reason, many

people are currently turning towards systems that have been perfected over millions of years; those of the natural world. Biomimicry is the science of taking design cues from nature, and applying those principles to man-made systems to solve problems in a more efficient manner.

Perhaps the most well-known example of biomimicry is the invention of Velcro: this hook-and-loop fastener was developed in 1941, after George de Mestral observed how well the flowers of the mountain thistle stuck to his clothing due to the flower's tiny hooks [16]. Other examples of how engineers have turned to nature include everything from new blade designs for fans and turbines based on the fins of a humpback whale which have tubercles (bumps) on their leading edge to delay stall [17], to cars with ultra-low drag coefficients based on the body of a Boxfish [18], to paint which mimics the surface of the lotus flower's ability to keep itself clean [19], and much more [20].

Even the field of robotics has begun taking cues from the natural world. Examples of biomimicry in hardware include the development of 'soft' robots which are able to flex in ways previously not possible without introducing large levels of complexity. These 'soft' robots use hydrostatic skeletons based on the motion of elephant trunks and octopus arms [21]. Examples of biomimicry in programming development include the use of swarm theory, taken from observations of groups of creatures such as the bees, fish, birds, and ants. Examples of where swarm theory is being applied include process optimization, network routing, algorithms for creating more realistic groups of creatures in 3D animation, groups of small Unmanned Underwater Remotely Operated Vehicles (UUVs), and groups of small spacecraft which communicate with each other to explore and collect data [22].

The goal of this work is to investigate alternative micro-motor designs based on bio-inspired modes of locomotion. As one such example, Chan built two robotic snails several centimetres long [23; 24], with one being driven by an electric motor and one being driven by shape memory alloy. Both of these, like their biological namesakes, moved on a thin layer of fluid. Biomimicry can be just as easily applied to large-scale objects as those at the microscopic level; small organism & MEMS make a good fit: the world of small organisms and MEMS is both dominated by surface and friction forces, and they often use modes of locomotion that are less common at the macro scale. Smaller organisms are less likely to move by walking, and more likely to move in other ways such as sliding, or by peristaltic action where sequential contraction and expansion produces motion. Bio-mimicry has been used in MEMS before: as the name implies, inchworm motors mimic the motion of inchworms. Brown developed a micro crawler based on the motion of snails [7], and Shay developed planar micro conveyors that used locomotion modes derived from crabs [25]. Peristaltic motion has also been used in MEMS, for example Jeong [26] fabricated peristaltic micro-pumps from PDMS, with three flexible pneumatic actuators that sequentially pushed fluids through a micro-channel.

1.4.2 Earthworm Biology

Earthworms are small invertebrates, ranging in size from the very small earthworms which can barely be seen by the eye, to the very large Megascolides australis which average 75 cm in length [27]. The common earthworm, Lumbricus terrestris, averages a few inches in length [28], and can be seen in Figure 1.4.1. The cylindrical body of a large earthworm

can contain between 100 and 200 individual segments [29]; these segments can be seen in Figure 1.4.2.

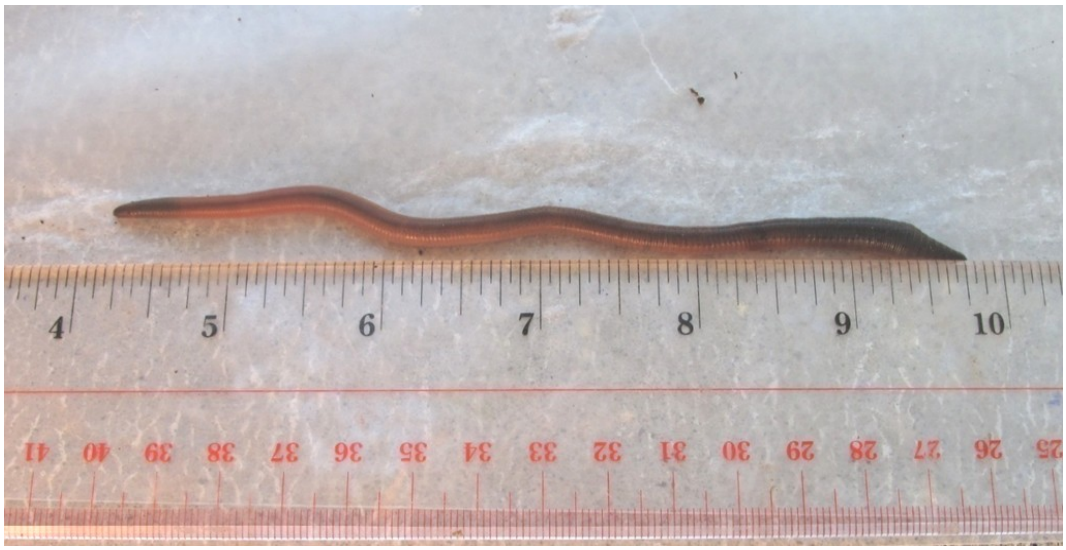

Figure 1.4.1 - A Common Earthworm

Figure 1.4.2 - Earthworm Segments

Earthworms fall under three main categories: Endogenic worms which spend most of their time around the roots of plants and rarely surface, Anecic worms which live beneath the soil but surface occasionally, and Epigeic worms which generally live in piles of leaves or plant matter found on the surface [30].

As seen in Figure 1.4.3, each segment of the earthworm has two sets of muscles that surround a closed sack of coelomic fluid. Since the fluid is incompressible, it serves as a hydrostatic skeleton; as the circular muscles contract they make the segment longer and thinner, and as the longitudinal muscles contract they make the segment shorter and fatter. The earthworm can move forward by anchoring its tail while it moves its head, then anchoring its forward sections and pulling its tail forward; rearward motion is simply the reverse. To aide in its motion, earthworms have sets of bristle-like hairs called setae, typically with 8-12 per segment [30], which can assist in grip by being extended into the soil. To allow more fluid motion, the worm expands and contracts the segments like a travelling wave; by repeating this peristaltic wave, the peristaltic wave 'steps' are summed, yielding a net motion in either direction; a graphic of this motion can be seen in Figure 1.4.4. Internal coelomic pressures of 1 kg/cm^3 have been recorded, with thrust forces between 2 and 8g [31]. A large adult earthworm can move with waves at a frequency of approximately 0.3 Hz, allowing linear motion in the range of 5-10 mm/s [32].

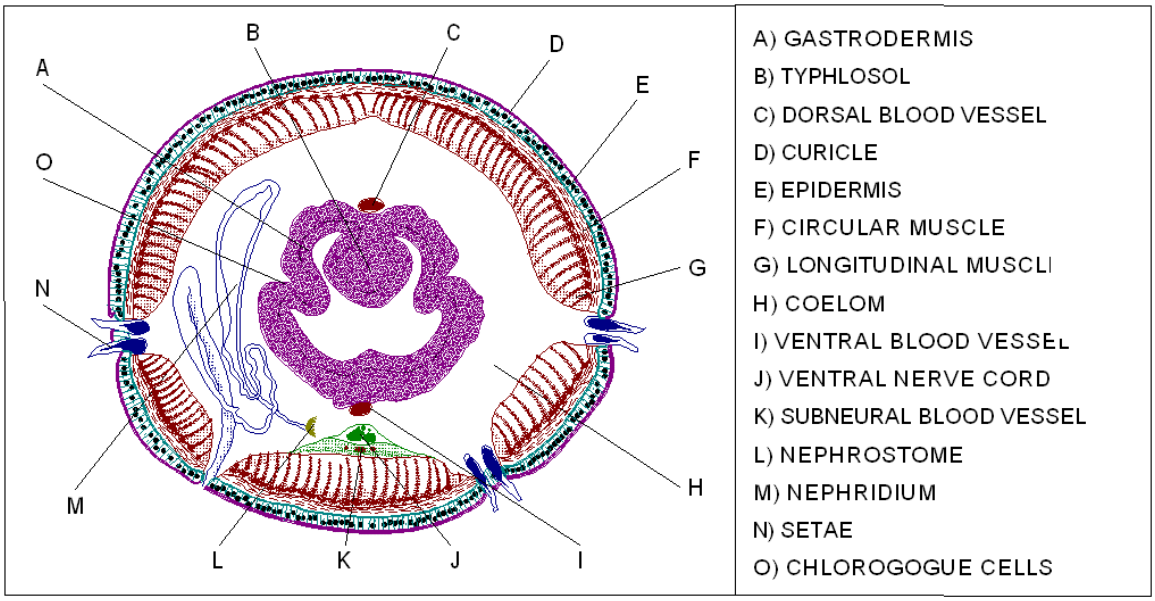

Figure 1.4.3 - Earthworm Cross-Section [33]

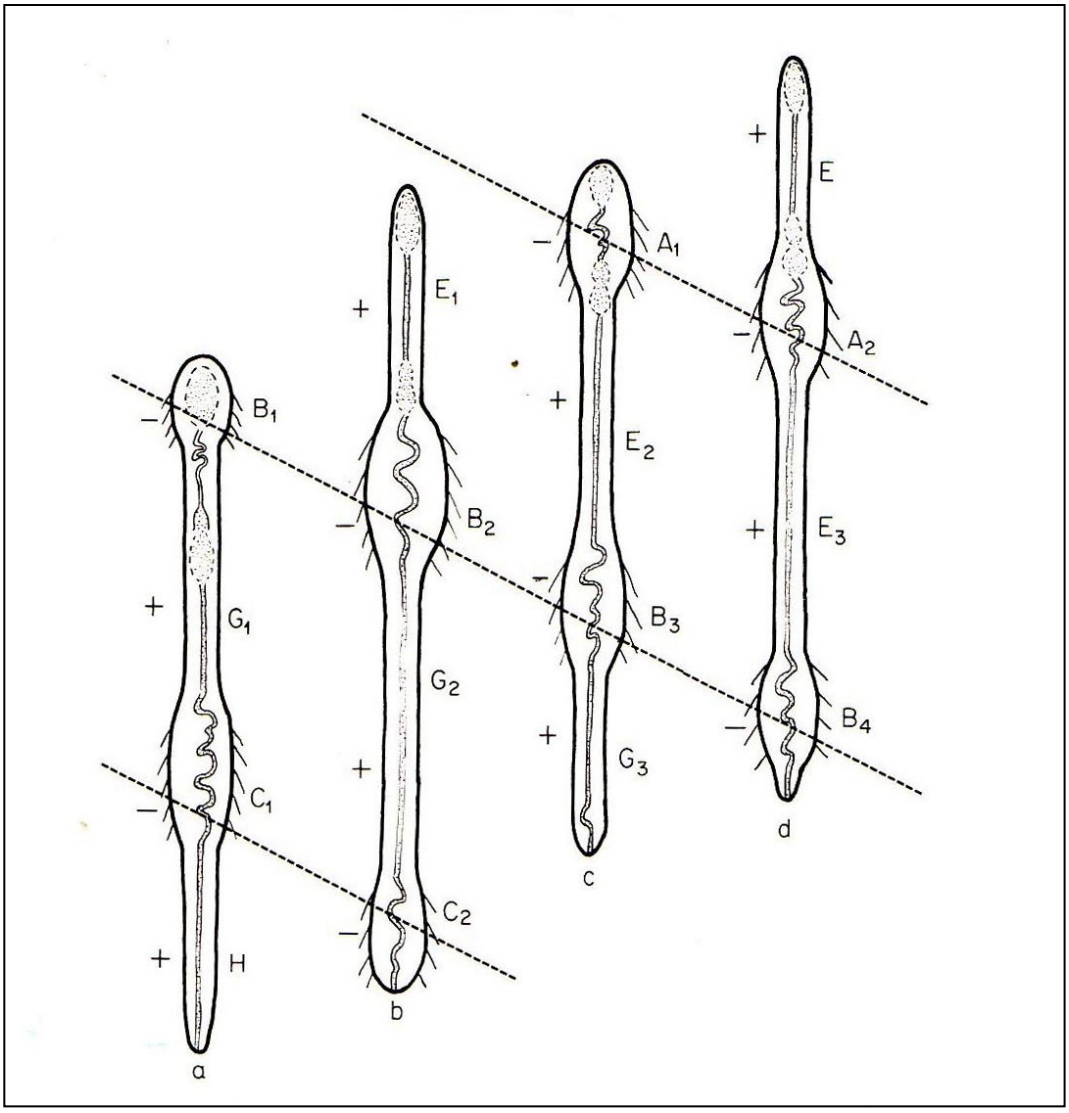

Figure 1.4.4 - Earthworm Motion [31]

1.5 MEMS Actuators

MEMS actuators are devices that convert electrical signals into motion. There are many different types of MEMS actuators, with the most commonly found being those that use electrostatic or electrothermal principles; these two actuator types will be discussed in greater

detail later in this work. Other MEMS actuators include piezoelectrics, magnetic actuators, and fluid pumps, which will be briefly discussed further in this section.

Piezoelectric actuators utilize a special material that reacts by producing an electric charge when a force is applied to it, or reacts with a force when an electric charge is applied. Unfortunately, silicon (the most common MEMS material) is non-piezoelectric; to overcome this, a piezoelectric material, most commonly PZT (made from lead, zirconium, and titanium), is laid as a thin film in combination with silicon components [34]. Piezoelectrics are not found as frequently as other actuators due to the cost and complexity of the specialized manufacturing process required to produce them. They are capable of outputting large forces (typically between 10-1000 μN) with a small device footprint, but this often comes at the expense of reduced displacements (typically between 0.1-1000 μm). This trade-off is due to the nature of the material itself; a higher piezoelectric strain coefficient implies lower Young's modulus [35]. Due to their high force densities, high-frequency capabilities, and low operating voltages, these actuators can be found in switching applications, and ultrasound transducers.

Magnetic MEMS actuators have one underlying weakness: at the micro-scale, magnetic forces are very relatively weak. These weak forces, combined with the fact that silicon is non-magnetic, means that they are not commonly found in most MEMS devices. Magnetic MEMS materials are still being developed, as are the processes used to fabricate the actuators themselves. Typical expected forces for these actuators are in the range of 0.1-100 μN, with typical displacements lying in the range of 10-1000 μm [35]. The magnetic forces used to drive these actuators can be located either directly on the MEMS chip, or the devices can react to a magnetic source located off-chip. Applications of this technology can be

found in the recording head of a hard-disk drive, magnetic field sensors, and high-speed switching [36].

MEMS actuators based on the motion or expansion of fluid have been developed and proven, with actuator designs varying widely from electrokinetic arrays that propel particles encapsulated within a fluid [37; 38], to micro bladders that expand and contract [39; 40]. Forces and displacements are completely dependent on the fluidic actuator type, and vary widely, but are capable of offering a high force and displacement [35]. Microfluidic actuators can be designed using standard MEMS processes; however systems that require micro-valving can run into issues due to the fact that micro valves are extraordinarily complicated and micro-tolerances are poor, often leading to leaky valves.

1.5.1 Electrostatic Drive

One of the most common types of MEMS actuator is the electrostatic drive actuator. Electrostatic actuators offer much higher operating frequencies and greater efficiencies than their thermal counterparts, and have a proven reliability record; however, these benefits are often accompanied by a requirement for a larger device footprint and higher operating voltages. These devices are also susceptible to issues with dust and humidity, as well as charge accumulation. While there are other electrostatic device types, such as the electrostatic rotary motor and scratch-drive actuator, two are the most commonly found: Linear Comb Drive (LCD) arrays, and Parallel Plate arrays.

Of the two types of arrays, LCD are the most common, with their primary advantage being that their force is independent of displacement, allowing large actuator deflection ranges (typically around 10-20 μm [35]) without a varying force to account for [41]. To

achieve motion, LCD arrays employ large numbers of evenly spaced inter-laced 'fingers,' as seen in Figure 1.5.1, that are charged so that they attract one other. They must be designed to be very rigid perpendicular to the direction of the fingers, to prevent the array from twisting and the fingers making contact with one-another. Typically, this is achieved through the use of a folded-spring suspension; which is stiff in one direction, while remaining soft in another. Another consideration that must be taken into account in the design of LCD arrays is that stops must be implemented to limit the actuator's travel to prevent the two combs from contacting one another, and shorting. The ideal force output of a LCD array [41] is:

$$F = \frac{n\varepsilon\varepsilon_0 t}{g} V^2$$

Equation 1.5.1

Where: F is the force output (N), n is the number of fingers, ε_0 is the dielectric constant of a vacuum ($8.85X10^{-12}$ F/m), ε is the relative dielectric constant of the medium the array is in (air, water, etc.), t is the finger thickness (m), g is the spacing between fingers (m), and V is the voltage potential across the comb pair (V).

This means that the LCD array shown in Figure 1.5.1, running at typical voltages (>100V) will produce forces in the range of ~5 μN.

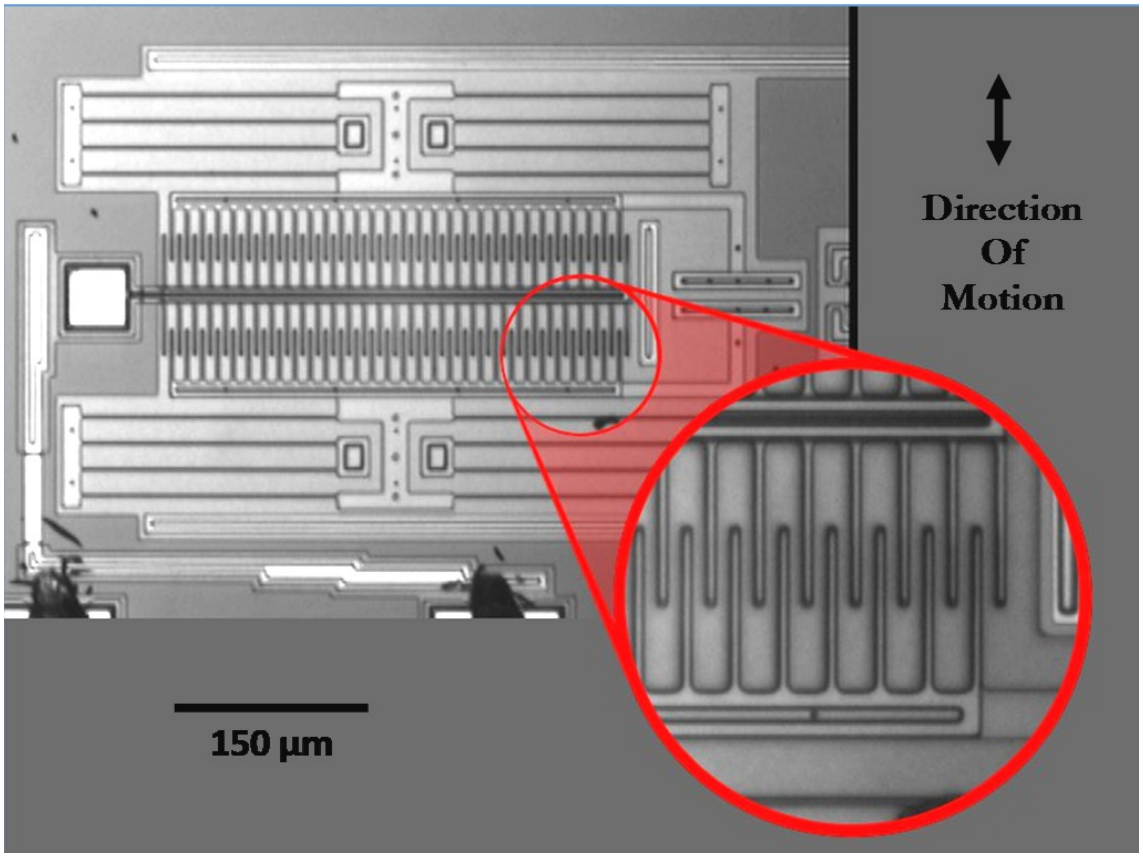

Figure 1.5.1 - Electrostatic Comb Drive Actuator

Parallel Plate arrays yield greater forces than their LCD counterparts, but do so at the expense of a much smaller travel distance (typically <1um [35]). As well, the force output varies with the actuator distance traveled. As shown in Figure 1.5.2, Parallel Plate arrays use inter-laced combs that are slightly offset, creating a closer gap on one side of a finger than the other. The total theoretical distance before the device becomes unstable is 1/3 the initial gap; past this point, the combs tend to 'snap in,' meaning they snap together. To avoid the issues with 'snap in,' stops are generally added before this limiting point. The ideal force output of a Parallel Plate array [41] is:

$$F = \frac{n\varepsilon\varepsilon_0 A}{2} V^2 \left(\frac{1}{{g_1}^2} - \frac{1}{{g_2}^2}\right)$$

Equation 1.5.2

Where: F is the force output (N), n is the number of fingers, ε_0 is the dielectric constant of a vacuum ($8.85X10^{-12}$ F/m), ε is the relative dielectric constant of the medium the array is in (air, water, etc.), A is overlapping area of the fingers (m^2), V is the voltage potential across the comb pair (V), g_1 is the smaller of the two gaps between the fingers (m), and g_2 is the larger of the two gaps between the fingers (m)

This means that the Parallel Plate array as shown in Figure 1.5.2, running at typical voltages (<40V) will produce forces in the range of ~10-50 μN.

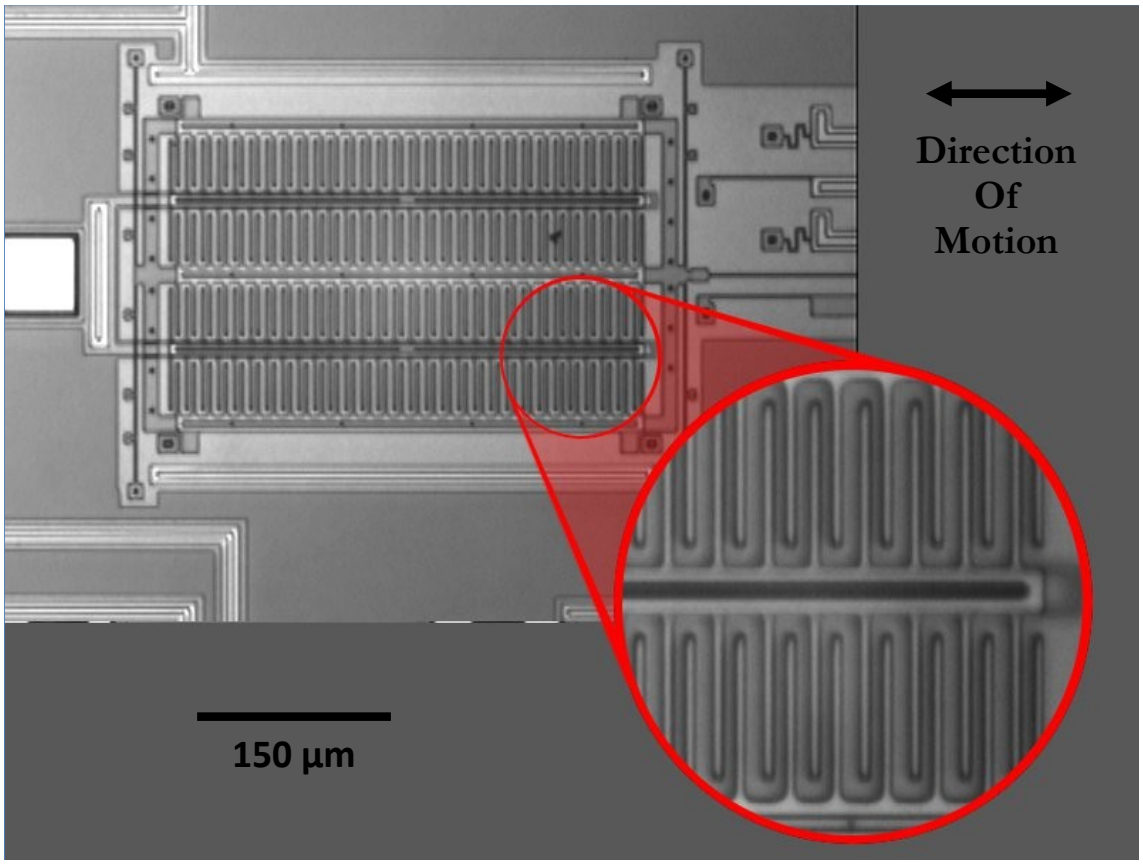

Figure 1.5.2 - Electrostatic Parallel Plate Actuator which direction is motion

1.5.2 Thermal Actuators

Thermal actuators operate by passing a current through the actuator; the effects of Joule heating cause the actuators to expand, creating motion. There are many different types of thermal actuators (TAs), with classifications generally being made by material type and actuator geometry. While most thermal actuators are generally made from silicon (often polysilicon), they can also be made from other materials such as: polymers, metals, and Shape Memory Alloys (SMAs). The most commonly found thermal actuators are chevron-style actuators and thermal bimorph actuators, with variances on basic designs to accomplish

different motion types. Forces and displacements from TAs can vary widely depending on the actuator's geometry and material.

Almost every MEMS TA operates by passing an electrical current through a structure. Due to the structure's electrical resistance, heat is produced (joule heating), as calculated by the following equation:

$$q = \frac{V_i^2}{R_i}$$

Equation 1.5.3

Where: V_i is the voltage across the actuator's i^{th} arm, and R_i is the resistance of the actuator's i^{th} arm. This heat causes the actuator's arms to expand which, with the exception of SMA actuators, is how a TA produces its motion.

By changing the structure's geometry, one can predictably change how the structure will deform and optimize it to suit a particular application. TAs are reliable, simple, and small; but they are extremely inefficient due to the heat generated by their operation. While they can operate at relatively high frequencies, they cannot operate as fast as their electrostatic or piezoelectric counterparts.

1.5.2.1 Thermal Actuator Material

The most common material for use in thermal actuators is polysilicon due to its availability, reliability, ease of fabrication, and well-known material properties. Polysilicon is the most common MEMS structural material, so using it for actuators generally does not require any special material choice or post-processing for their implementation.

Micro-actuators made from conductive polymers can be advantageous due to their high rate of thermal expansion [42; 43], which often yields larger displacements than their silicon counterparts (strains in the range of 12%), but some compounds can deteriorate after less than a million operation cycles [44]. However, producing the conductive polymer compounds required for these actuators can be difficult and thus, the process is not widely used. Also, some of the polymeric compounds used have issues with plastic deformations when exposed to high temperatures.

Shape Memory Alloy (SMA) actuators can provide very high force capacities and displacements (0.01-1.0N, and 10-100 μm [35]) by employing specialized materials which exhibits shape recovery during a phase transition. Nitinol, a nickel-titanium alloy, is an example of one such material; when it is at a temperature less than its transition temperature it has a martensitic crystal structure, but it changes to an austenitic crystal structure when its temperature is raised above that point. This change in structure causes the Nitinol to revert back to the position that it has been 'trained' for by undergoing a heating and cooling process while being restrained in the desired position [45]. Like their piezo-electric counterparts, shape memory alloys are often used in conjunction with another material to produce actuators. Nitinol has some unfortunate downsides; it's electrical resistivity changes with its phase, and cycled actuators tend to show decreased force and displacement, as well as increased plastic deformation and changes in transition temperature [46], and the amount of time it takes for them to cool below transition temperatures severely limit their operating frequencies. These material problems, coupled with process complexities, have resulted in shape memory alloys not being a widely used actuator in today's Micro Electro-Mechanical Systems.

1.5.2.2 Thermal Actuator Geometry

There are two main geometries of TAs: bimorph actuators and chevron actuators, although other designs do exist that combine attributes of each geometry, or produce out-of-plane motion.

Thermal Bimorph TAs are U-shaped, with one arm being much wider and/or thicker than the other. Figure 1.5.3 shows a schematic of a bimorph-style TA, with the left hand bimorph being in the unpowered state and the right hand bimorph being in the powered state. In a bimorph TA the entire actuator acts as a loop of resistive wire, but since one arm has a larger cross-sectional area it has a lower resistance than the smaller arm. This means that the two arms have different current densities; since both arms are made from the same material, they have different rates of heating, and thus have different rates of expansion. In Figure 1.5.3, the hot arm is coloured red, the cold arm yellow, the flexure (the small piece that allows the cold arm to rotate) orange, and the locations where the actuator is anchored to the chip's surface are blue.

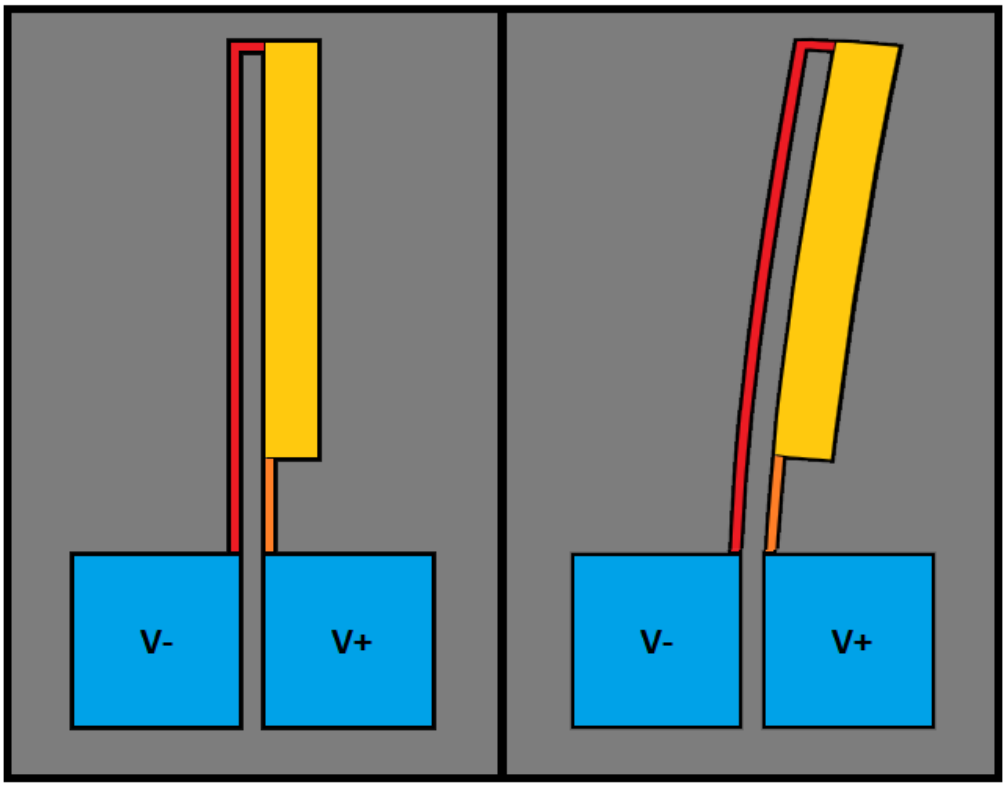

Figure 1.5.3 - Thermal Bimorph Actuator (Actuator Length ~150 μm)

Polysilicon actuators typically used in the Dalhousie MEMS Lab with a bimorph geometry provide fairly large displacements (~10 μm), but relatively low forces (~10μN), and are typically 200-300 μm in length. Bimorph actuators can also be modified to produce out-of-plane (z) motion as opposed to in-plane motion (x, y); these Vertical TAs (VTAs) still operate with the principle of having one thin (hot) arm, and one thicker (cold) arm.

The other main geometry for a TA is the chevron-style actuator, as seen in Figure 1.5.4. Since all of the arms on a standard chevron TA are the same size, they all heat equally; and thus, they expand equally (red arrows). This expansion is amplified due to a small bend in the beam (typically 3-6 degrees); since the arms are anchored on the ends, this bend forces

the beam to buckle in one direction (black arrow). In order to achieve greater force, more arms may be added to the actuator.

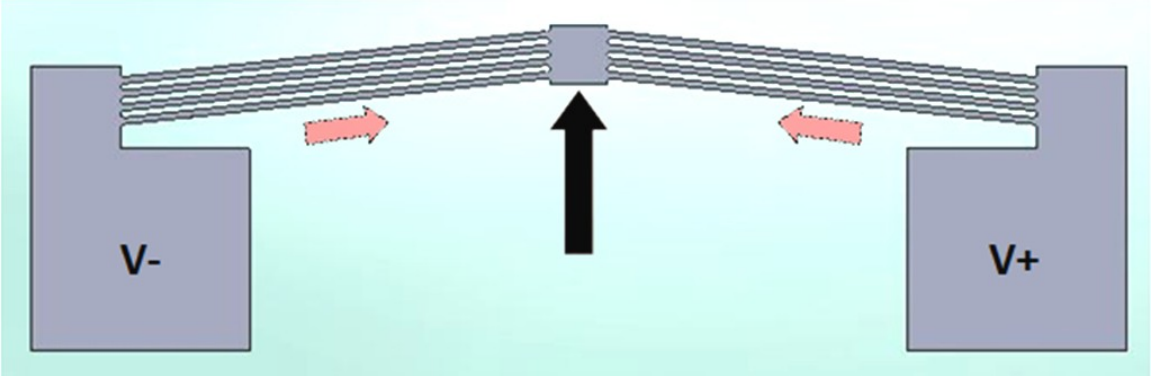

Figure 1.5.4 - Thermal Chevron Actuator (Size ~100 x 400 μm)

Polysilicon chevron TAs typically used in the Dalhousie MEMS Lab are typically in the range of 200-400 μm in length, and produce and approximately 100-200 μN of force. However, their displacement is relatively small, in the 2-6 μm range, and thus may require amplification if large displacements are required. An example of an amplified chevron can be found in Figure 1.5.5, with the photo on the left being in the unpowered state, and the photo on the right being in the powered state. Amplified chevrons typically used in the Dalhousie MEMS Lab can achieve forces in the range of 1-5 μN, and displacements in the range of 10-40 μm. Like the bimorph TA, the chevron TA can be adapted for out-of-plane motion if necessary; in a chevron-VTA, the chevron motion remains in plane and an out-of-plane VTA-like unpowered curling structure is affixed to the tip of the chevron.

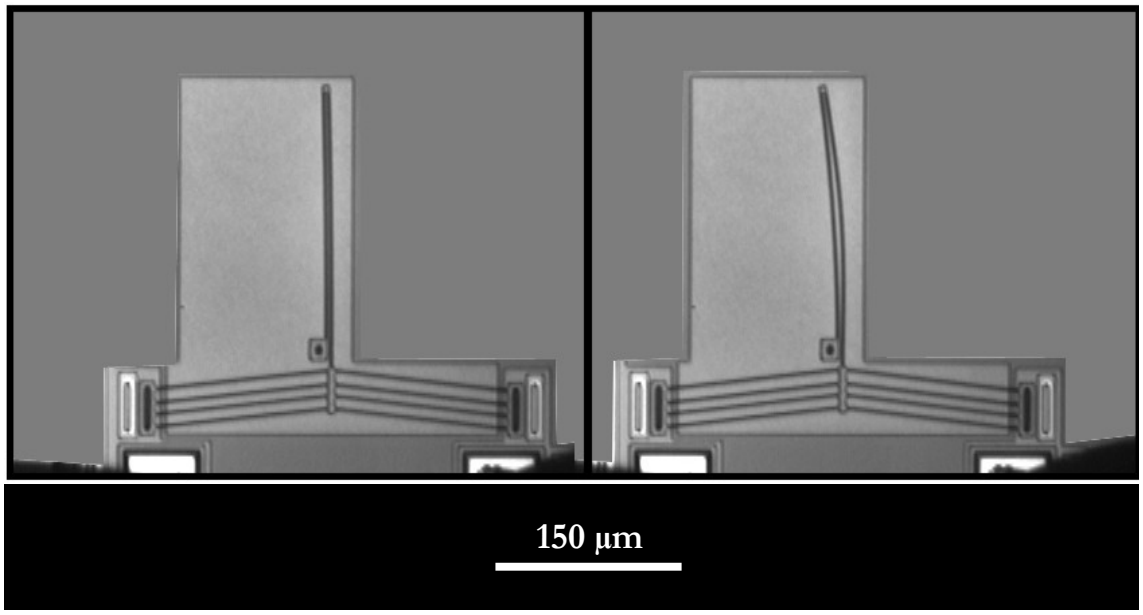

Figure 1.5.5 - Amplified Thermal Chevron

1.5.2.3 Thermal Actuator Calculations

As seen in Figure 1.5.6, there are three modes of heat transfer that must be considered with respect to the thermal operation of a TA: convection, conduction, and radiation.

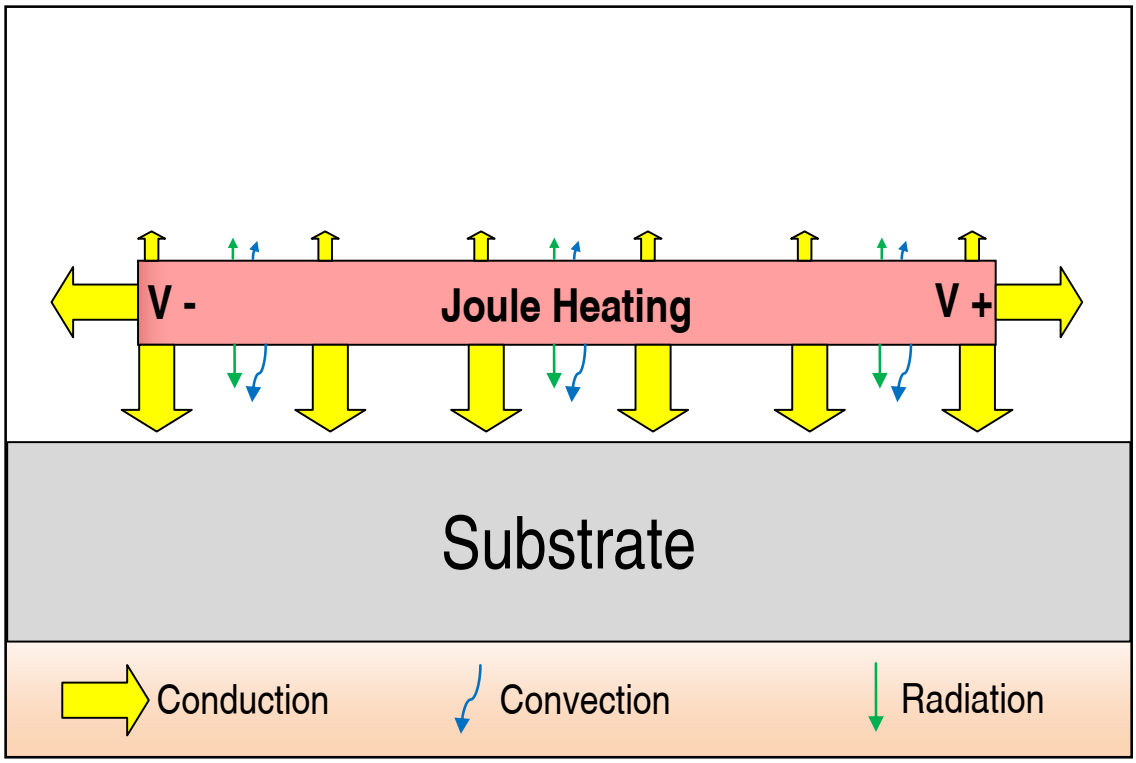

Figure 1.5.6 - Thermal Actuator Heat Transfer

Hickey [47] calculated the heat transfer analysis and thermal response for a TA, finding that heat loss due to radiation and convection is negligible when compared to conduction at the micro-scale; instead, most of the thermal actuator's heat is lost downward to the chip's substrate due to conduction. He found that if the thermal actuator arms are approximated by a first order system, the time constant and maximum temperatures respectively become [47]:

$$\tau_{approx_i} \cong \frac{C_{mat}\,\rho\,A_i\,\Delta z}{k_{air}\,\frac{P_i}{2}}$$

Equation 1.5.4

$$T_{max} = \left(\frac{V_i^2}{R_i}\right)\left(\frac{\Delta z}{k_{air}\,\frac{P_i}{2L_i}}\right)$$

Equation 1.5.5

Where: C_{mat} is the specific heat of the actuator material (Polysilicon = 860 $\frac{J}{Kg\ K}$), ρ is the density of the actuator material (Polysilicon = 2300 $\frac{kg}{m^3}$), A_i is the area of the ith arm, Δz is the vertical spacing between the TA and the chip's substrate, k_{air} is the thermal conductivity of air (0.03 $\frac{W}{mk}$), P_i is the cross-sectional perimeter of the ith arm, V_i is the voltage across the actuator's ith arm, and R_i is the resistance of the actuator's ith arm.

The thermal time constant (~50-200 μs) is primarily affected by the actuator's cross-section and lead to thermal cut-off frequencies in the range of 2-3 kHz, while the actuator's mechanical response time is dependant mainly on its length. Common micro-thermal actuators have resonance frequencies in the 50-200 kHz range [47].

At lower frequencies, the actuator's motion is dominated by the first order thermal response, at higher frequencies, the second order mechanical response also has an effect. It should be noted that the actuators used for the micro-scale earthworm crawler were operated well below their resonant frequencies (<10 kHz), and are therefore dominated by the thermal response.

Lai [48] calculated the maximum theoretical force and work of an expanding rod (a single, straight arm) as:

$$Force = A\sigma = AE\varepsilon = AE\alpha T_{avg} L$$

Equation 1.5.6

$$Work = \frac{F\Delta L}{2} = \frac{AE\alpha}{2} L^2 \left(T_{avg}\right)^2 = \frac{1}{2} AE\alpha^2 \left(\int_{x=0}^{x=L} T(x)\, dx \right)^2$$

Equation 1.5.7

Where: A is the arm's cross-sectional area (m^2), σ is the arm's axial stress (Pa), E is the Young's modulus of the arm (Pa), ε is the arm's strain $[\varepsilon(x) = \alpha T(x)]$, α is the arm's coefficient of thermal expansion (1/°C), T is the arm's temperature (°C), and L is the arm's length (m). It should be noted that common chevron-type actuators are capable of outputting work in the range of ~10-50 pW.

1.6 MEMS Processes

While other specialty processes have been developed for the production of some actuators, like those described in Section 1.5, there are three Multi-User MEMS Processes (MUMPs) that are commonly used. MUMPs, a service offered by MEMSCAP Inc, allows people to purchase a small number of MEMS die locations on a wafer, as opposed to an

entire run. This allows scientists and researchers to test their designs on a small-scale without having to invest in fabrication equipment, or pay for an entire batch of thousands of chips. In Canada, the MUMPs processes, as well as the tools and software to design and test MEMS devices, are subsidized by the Canadian Microelectronics Corporation (CMC Microsystems). Since MUMPs processes are standardized, they have set design guidelines and are well understood; this means that researchers will have a greater chance of success with their designs. There are three main MUMPs processes that are offered: PolyMUMPs, SOIMUMPs, and MetalMUMPs. Each process is intended for the widest range of possible uses, but is still better for some devices than for others due to the materials used, and the process's feature sizes and spacings. MEMSCAP offers guides [49; 50; 51] for each process, including design rules specific to that process; these rules are built from years of experience with the processes themselves, and are put in place to allow designers the greatest chance of device success. Before submitting a chip for fabrication, the design must first pass CMC's Design Rule Check (DRC) to verify that all rules were abided by; any rule violations that were found by the DRC must be sufficiently explained by the designer before the chip design will be accepted.

Of the three, PolyMUMPs is the most commonly used and the best understood; it provides multiple layers of polysilicon and oxides in combination with conductive metal; this process, while thin, has a small minimum feature size (2 μm) and allows a large range of designs to be made using the same process. The PolyMUMPs process will be discussed further in Section 1.6.1.

Silicon on Insulator MUMPs (SOIMUMPs) was introduced in 2003, and was developed from the MEMSCAP Variable Optical Attenuator project [49]. It covers two separate run

thicknesses, with both types using the same process flow; a diagram of the layers found in SOIMUMPs can be seen in Figure 1.6.1. Designers using SOIMUMPS have a choice of two silicon thickness layers (10 and 25 μm), with the substrate thickness being 400 μm in both cases.

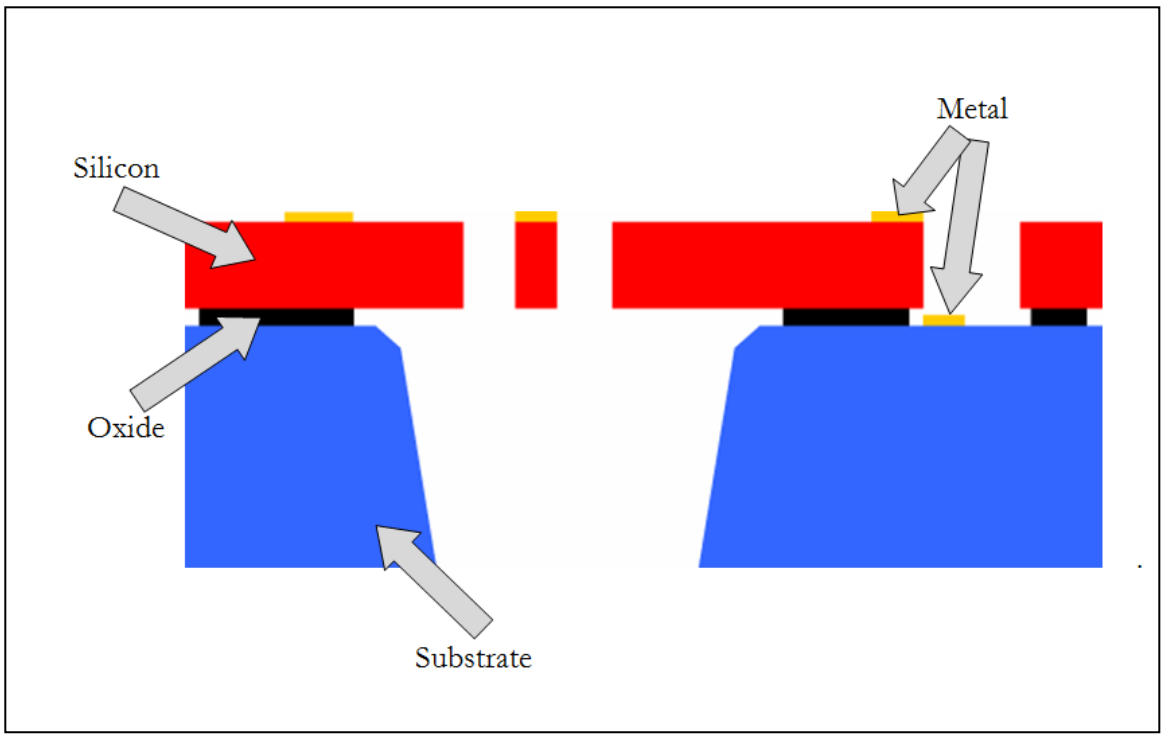

Figure 1.6.1 - SOIMUMPS Layers [49] (Not to Scale)

The SOIMUMPs process offers the benefits of large vertical heights, in addition to two separate metal layers for bonding pads and reflective surfaces. As well, through the use of an additional bottom-side etching step (TRENCH), through-hole structures are possible. These features make SOIMUMPs a good choice for optical switching, or devices that require larger vertical surfaces or stiffer mechanical structures. Unfortunately, as seen in Table 1.6.1,

designers are severely restricted as to how much space on the chip they can have without silicon (33%) or with metal (20%). As well, some of the process layers have very large minimum feature sizes and spacings (TRENCH=200 μm, BLANKETMETAL=100 μm) or have poor alignment tolerancing (METAL to SOI=±40 μm , TRENCH to SOI=±50 μm). These restrictions mean that the SOIMUMPs process is frequently unsuitable for use when designing frictional crawlers. For reference, the general rules for this process are included in Table 1.6.1 and Table 1.6.2.

Layer	Minimum Feature size	Minimum Spacing	Maximum Feature Length	Maximum Etched Area
PADMETAL	3 μm	3 μm	5000 μm	20% of chip area
SOI	2 μm	2 μm	Unlimited if width > 6 μm	33% of chip area
SOIHOLE	3 μm	3 μm	not applicable	not applicable
TRENCH	200 μm	200 μm	5000 μm	20% of chip area
BLANKETMETAL	100 μm	100 μm	5000 μm	20% of chip area

Table 1.6.1 - SOIMUMPs Process Rules [49]

Layer Combination	Center to Center Overlay Tolerance	Edge to Edge Bias
PADMETAL to SOI	±3 μm	±3 μm
TRENCH TO SOI	±5 μm	<50 μm
METAL TO SOI	±35 μm	±40 μm

Table 1.6.2 - SOIMUMPs Layer Combination Rules [49]

MetalMUMPs was introduced in 2003, and was derived from work on micro-relays using thermal actuators in the 1990's [50]. The MetalMUMPs process, a diagram of which can be seen in Figure 1.6.2, allows designers the ability to create highly conductive mechanical structures made from a single 20.5 μm thick electroplated nickel layer; it also

offers a doped 0.7 μm thick polysilicon layer for use as resistors, heaters, or electrical cross-overs.

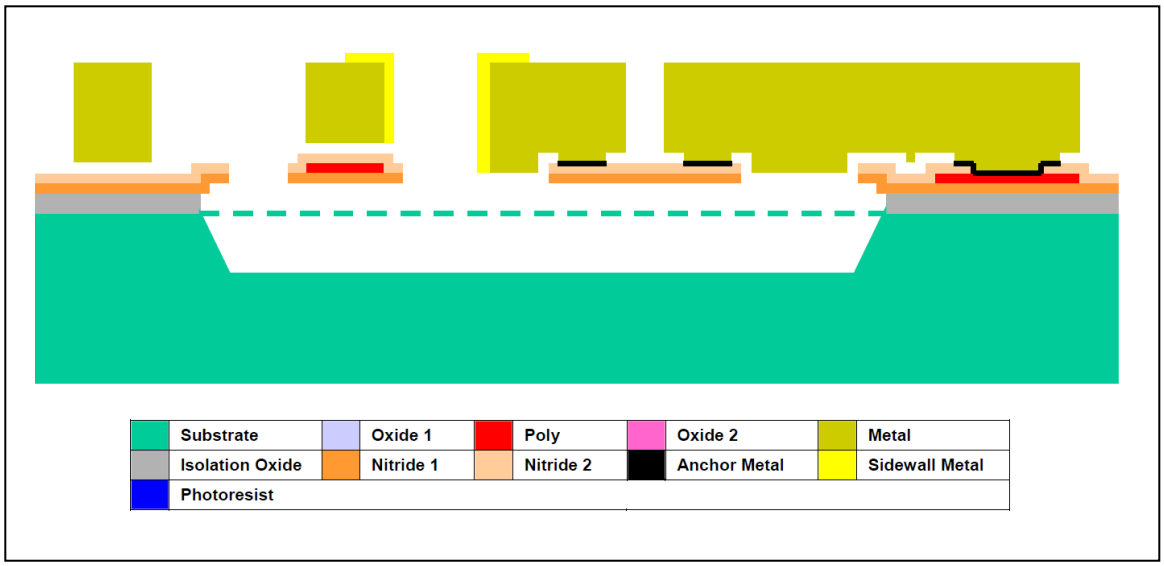

Figure 1.6.2 - MetalMUMPs Layers [50] (Not to Scale)

Its ability to coat the side-walls of structures with a layer of highly conductive gold, and to create trenches in the silicon substrate for fluid flow or further electrical/thermal isolation makes MetalMUMPs a good fit for use for electrical switching, RF devices, and microfluidics. However, this process is not without its drawbacks; the lack of multiple layers offered in MetalMUMPs limits the amount of devices that can successfully be constructed in this technology, and its large feature sizes (METAL=8 μm, OXIDE1=20 μm, METANCH=50 μm, GOLDOVP= 50 μm) and spacings (METAL=8 μm, OXIDE1=20 μm, GOLDOVP= 50 μm) can force designers to create larger-than-necessary devices. For

reference, the layer thicknesses and general rules for this process are included in Table 1.6.3 and Table 1.6.4.

Material Layer	Material Thickness	Comments
Isolation Oxide	2.0 μm	2.0 μm thermal oxide
Oxide 1	0.5 μm	0.5 μm PSG
Nitride 1	0.35 μm	0.35 μm low-stress silicon-nitride
Polysilicon	0.7 μm	0.7 μm doped polysilicon
Nitride 2	0.35 μm	0.35 μm low-stress silicon-nitride
Oxide 2	1.1 μm	1.1 μm PSG
Anchor Metal	0.035 μm	10 nm Cr + 25 nm Pt
Plating Base	0.55 μm	500 nm Cu + 50 nm Ti
Metal	20.5 μm	20.5 μm Ni + 05 μm Au
Sidewall Metal	1.0 - 3.0 μm	1-3 μm Au

Table 1.6.3 - MetalMUMPs Layer Thicknesses [50]

Layer	Minimum Feature Size	Minimum Spacing
OXIDE1	20 μm	20 μm
POLY	5 μm	5 μm
NITRHOLE	5 μm	5 μm
METANCH	50 μm	10 μm
METAL	8 μm	8 μm
GOLDOVP	50 μm	50 μm
HOLEP	5 μm	5 μm
HOLEM	8 μm	8 μm

Table 1.6.4 - MetalMUMPs Process Rules [50]

1.6.1 PolyMUMPs

PolyMUMPs is a three-layer surface micromachining process that has been developed from work originating at the University of California's Berkley Sensors and Actuators Center (BSAC) in the 1980's and 1990's [51]. PolyMUMPs provides three polysilicon structural layers (0.5, 2.0, and 1.5 μm thick respectively), as well as two sacrificial oxide (PSG) layers (2.0, 0.75 μm thick), an insulating silicon nitride layer (0.6 μm thick), and a conductive metal layer (0.5 μm thick). Sheet resistance of the polysilicon layers are 45, 20, and 30 Ω/sq respectively. The absolute minimum feature size of polysilicon elements in designs using the PolyMUMPs process is 2 μm. Figure 1.6.3 shows a diagram of the PolyMUMPS layers and their respective heights. Through the use of these layers, it is possible to build structures which act as bearings, hasps, hinges, and other various actuators that create motion both in, and out of plane; however, these devices must still comply with the standardized PolyMUMPs design rules, as summarized in Table 1.6.5 and Table 1.6.6. A summary of the PolyMUMPS process steps as well as graphical representations of the process flow are shown in Appendix A.

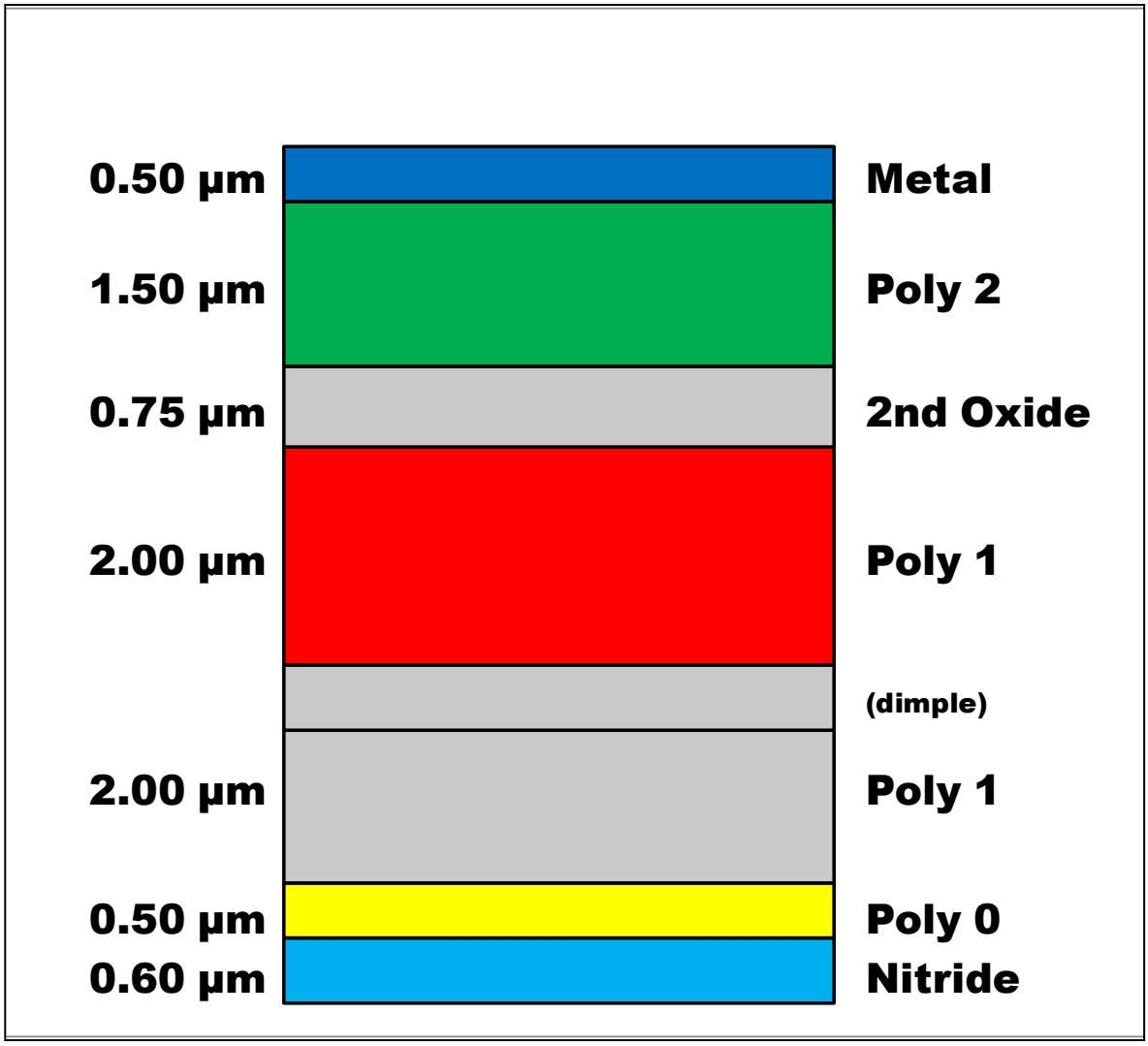

Figure 1.6.3 – PolyMUMPS Layers

Level 1	Level 2	Enclose By	Spacing Between
Poly 0	Anchor 1	4.0 μm	4.0 μm
	Poly 1	4.0 μm	
	Anchor 2	5.0 μm	5.0 μm
	Poly 2	5.0 μm	
Poly 1	Poly 0		
	Anchor 1	4.0 μm	
	Anchor 2		3.0 μm
	Poly 2	4.0 μm	
	Dimple	4.0 μm	
	Poly 1 - Poly 2 VIA	4.0 μm	
Poly 2	Poly 0		
	Poly 1		3.0 μm
	Poly 1 - Poly 2 VIA	4.0 μm	
	Anchor 2	5.0 μm	
	Metal	3.0 μm	
Hole M	Hole 2	2.0 μm	
Hole 2	Hole 1	2.0 μm	

Table 1.6.5 - PolyMUMPs Layer Rules [51]

Layer	Minimum Feature Size	Minimum Spacing
Poly 0	2.0 μm	2.0 μm
Dimple	2.0 μm for Spaces 3.0 μm for Holes	3.0 μm
Anchor 1	3.0 μm	2.0 μm
Poly 1	2.0 μm	2.0 μm
Poly 1 – Poly 2 VIA	2.0 μm for Spaces 3.0 μm for Holes	2.0 μm
Anchor 2	3.0 μm	2.0 μm
Poly 2	2.0 μm	2.0 μm
Metal	3.0 μm	3.0 μm
Hole 0	2.0 μm	2.0 μm
Hole 1	3.0 μm	3.0 μm
Hole 2	3.0 μm	3.0 μm
Hole M	4.0 μm	4.0 μm

Table 1.6.6 - PolyMUMPS Feature Sizes and Spacings [51]

Chapter 2: The Earthworm Crawler

This chapter covers the theory behind the earthworm crawler's design. It will illustrate why the earthworm crawler is able to move in the way it does, and explain how it is different from the current inchworm-type motion.

2.1 Earthworm Crawler Design Background

The earthworm uses of multiple segments of its body for moving; but, in its simplest form, only two segments are required to produce peristaltic motion. In the earthworm crawler, rather than the worm squeezing against a fixed burrow or tunnel in soil, the tunnel squeezes against the worm, which in this case is represented by a flexible shuttle. Figure 2.1.1 shows a simple model of a micro-scale crawler with each segment of the shuttle modeled by flexible diamond-shaped structures that are connected via a rigid bar, and a pair of actuators that engages each diamond. To reduce rotation and allow the actuators to maintain contact with the shuttle over a longer range of motion, the diamond-shaped segments have stiff flat bars attached on the top and bottom. The first step of the operation is to activate all actuators to ensure that the gap between the actuators and the worm is even on both diamonds, and the actuators are just touching the shuttle.

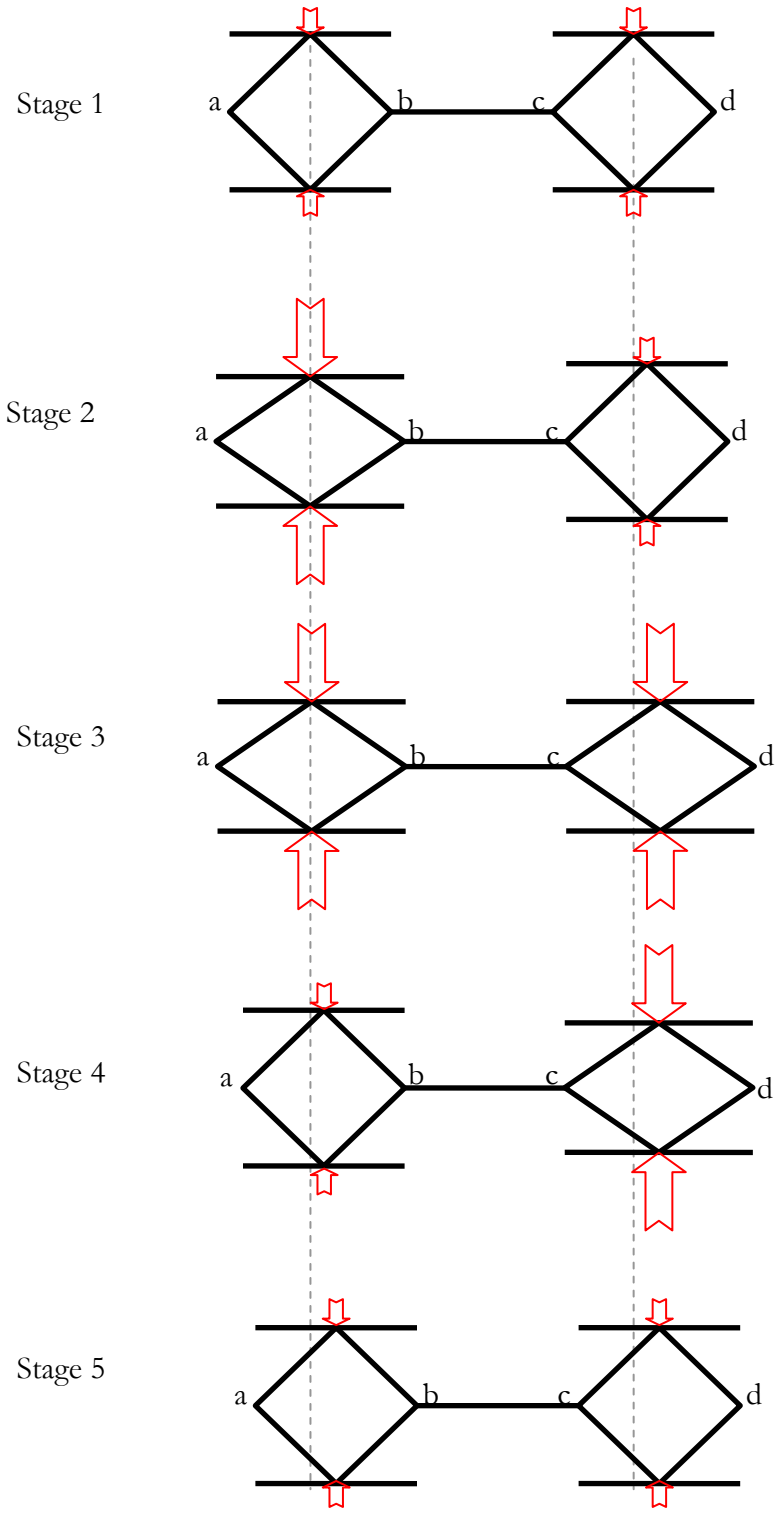

Figure 2.1.1 - Schematic of Peristaltic Motion of a 2 Segment Earthworm Model.

There are 4 different stages to complete one full step of the crawler's motion, starting with Stage 1: the pre-loading of the shuttle in Figure 2.1.1; the amount of pre-load controlling the sustained force capacity of the shuttle, with more pre-load allowing larger forces at the expense of lowered motion.

In Stage 2, to move to the shuttle to the right the left diamond (between points *ab)* is squeezed by powering the left actuators (as shown by large red arrows). This simultaneously performs a clamping and thrusting operation. Because the clamping force on the right diamond is smaller than on the left diamond, its lateral frictional force is also smaller; this allows the right diamond to slip while the left diamond does not; let the stroke length produced by the actuator be *l*. The left diamond symmetrically compresses, pushing point *a* to the left (backward) a distance *l* and point *b* to the right (forward) a distance *l* (Note: *l* size is exaggerated in the figure). The motion of point *b* causes the right diamond (points *c* and *d)* to also slip forward a distance *l*.

In Stage 3, the right diamond is gradually squeezed; because the clamping force on the right diamond is smaller than on the left, the right diamond deforms and slips again while the left diamond does not. The slipping stops when the clamping forces on both diamonds reach the same level. The clamped left diamond prevents the right diamond from expanding backward, therefore points *b* and *c* remain advanced forward a distance *l* and point *d* moves forward an additional distance 2*l*.

In Stage 4, the left diamond is relaxed to the pre-load level; thus, point *a* of the relaxing and slipping left diamond now moves forward while the right diamond along with point *b* do not move, allowing point *a* to move forward a distance 2*l*. At this stage, the

points of the shuttle have made the following moves; point *a: –l+2l=+l,* point *b: +l,* point *c: +l,* point *d: +l+2l=+3l.*

Finally, in Stage 5, the right diamond is gradually relaxed to the pre-load level. Because the clamping force on the left is smaller than on the right, the left diamond slips while the right diamond relaxes without slipping: point *d* moves backward a distance *l*, point *c* and the entire left diamond move forward by an additional distance *l*. Thus the theoretical total distance moved per complete motor step is ideally twice the single actuator stroke length 2*l*.

Motion to the left is accomplished by simply reversing the order of steps, and step size can be controlled by squeezing each diamond further in each step. Other modes of locomotion are possible, such as holding one diamond slightly clamped while pulsing the other; but the above described mode is the simplest, and therefore is the one upon which this work was focused.

2.2 Earthworm vs. Inchworm Motors

Unlike the inchworm motors discussed in section 1.3, which rely on separate actuators for clamping and motion, the earthworm crawler uses the same actuator to allow both clamping and motion. The earthworm crawler uses three pairs of actuators to provide two-directions of motion (forwards and backwards), while the inchworm actuators require a minimum of three pairs to achieve the same results. This distinction is important, as generally the fewer the number of actuators required to produce motion, the smaller the device's footprint can be made.

The downfall of using the same actuators for both clamping and motion is that you are limited as to the amount of clamping force you can place on the shuttle and still allow motion. This is not to say that the earthworm can't still output a large force; only that that without a separate dedicated clamping actuator, the earthworm shuttle will be limited to a slightly lower force than its equivalent inchworm counterpart.

Chapter 3: Scale Model Testing

A common step in the design of MEMS devices in the Dalhousie MEMS Lab is the construction and testing of models at the macroscopic scale. Often, designers use these models to test and finalize new, unproven, designs before transferring the concepts to the microscopic scale. Typically, this is done due to the long turn-around time that is involved with the MUMPs processes discussed in Section 1.6 (~4-5 months), as well as the costs involved with chip fabrication. If any form of control (either open, or closed loop) is to be applied, the program can be first constructed and tested with the operation of the macro-model, and then modified to suit the needs of micro-scale operation. Preliminary testing can be performed at the macro-scale to enable the designer the ability to focus on those variations that will offer the best chance of device success.

In the case of the Earthworm Crawler, preliminary macro-scale testing was performed for four main reasons:

The first reason for macro-scale testing was for confirmation of the earthworm crawler's theory of motion, as explained in Chapter 2. The macro crawler was capable of moving slowly, and the individual steps could be observed first hand. It was very important to be sure that the crawler could actually move before work progressed to the micro-scale.

Secondly, it was important to finalize the design of a Labview program that is capable of outputting two signals out of phase to propel the crawler; the program had control for changing the crawler's direction of motion, frequency, and actuator displacement. This program was designed to be easily adaptable for use with the micro-scale earthworm crawler.

The third reason for macro testing was to complete preliminary frequency testing to ensure that the crawler was capable of running at a variety of frequencies.

Finally, it was not known if the Earthworm Crawler would require a flexible spring between its two diamonds to achieve reliable motion. Two different shuttle designs were tested (one with a spring, and one without) to determine if the micro-model would require the added complexity of a spring for its operation. As will be discussed later, the macro-scale model clearly indicated that this spring was not required for motion of the earthworm crawler.

3.1 Scale Model Design

A macro-model of the earthworm was designed using Siemens PLM's Solid Edge and manufactured in Dalhousie University's Faculty of Engineering machine shop. The model, measuring approximately 14" X 10" X 2.5", was fabricated of Ultra-High Molecular Weight Polyethylene (UHMW PE), aluminum, and stainless steel; it employed shuttles fabricated from steel strapping, and used servos for its motion. A photograph of the macro-earthworm can be seen in Figure 3.1.1. For exact model dimensions, the fabrication drawings for the macro-scale crawler can be found in Appendix B.

The model can be broken-down into a few key features:

1. The baseplate material was chosen due to its machinability, as well as the relatively low friction that UHMW PE offers. It was machined out of one solid piece (2" thick) to increase the device rigidity, as well as to ensure the crawler's guides were

parallel. There were eight guide blocks (four on each side) of the design, with each block containing a reamed hole for the pusher's two guide rods.

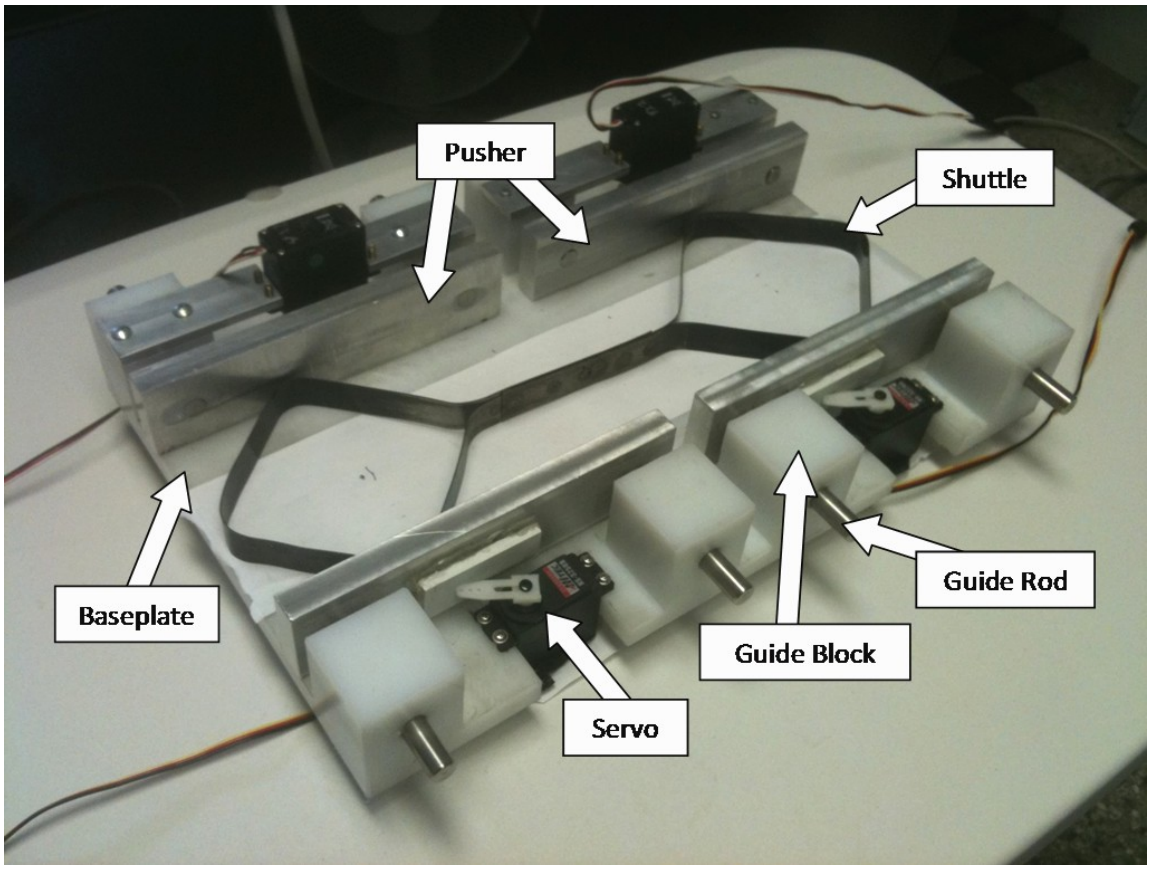

Figure 3.1.1 - Macro Earthworm Model (Model Size = 14" x 10")

2. The guide rods were fashioned from 3/8" stainless steel to allow smooth operation, and were of sufficient length (3") to allow a full range of motion. Each rod was threaded on one end to allow attachment to the pusher's aluminum face, with two rods per face to prevent twisting.

3. The pusher faces were fabricated of 6.5" long pieces of 1.5" X 0.5" Aluminum. The material was chosen due to the material's ease of machining, weight, and low cost. The material's thickness was chosen to prevent flexing during operation.
4. Servos were used to provide the necessary forces to drive the crawler due to their ease of use. Servos on one side of the model (the 'top' side) were flipped upside-down, so that when their wires were paired with the servo opposite (on the 'bottom' side) they would produce a symmetric 'squeezing' motion. This was required since, if un-flipped, the top/bottom servos would have to rotate in opposite direction to squeeze. By flipping half the servos, all top/bottom paired servos now rotate in like directions; the method of the servo's operation will be discussed later in this section. Attached to each servo was a 1" long nylon cam, which sat against the back of the plastic block that was affixed to the aluminum pusher. To allow a maximized range of the servos, small 3/16" thick plastic spacers were adhered to the back of the pushers with hot-melt adhesive. This took up the initial gap between the servo arms and the pushers.
5. The shuttles were made from steel packaging straps (those used to bind lifts of plywood) which were bent to the correct shape, and then spot-welded together. The material that the Department of Mechanical Engineering's rapid prototyper uses, which often cracks when exposed to high-deflection cyclic loading. For this reason, shuttles made from steel strapping were chosen due to the material's fatigue resistance, availability, and the ease of fabrication that it offered. Two shuttles were fabricated, as seen in Figure 3.1.2, with one having a S-shaped spring between the two diamonds and one without a spring. For ease of fabrication, the bars that would

be located at the tops and bottoms of the shuttle's diamonds to extend its range were omitted.

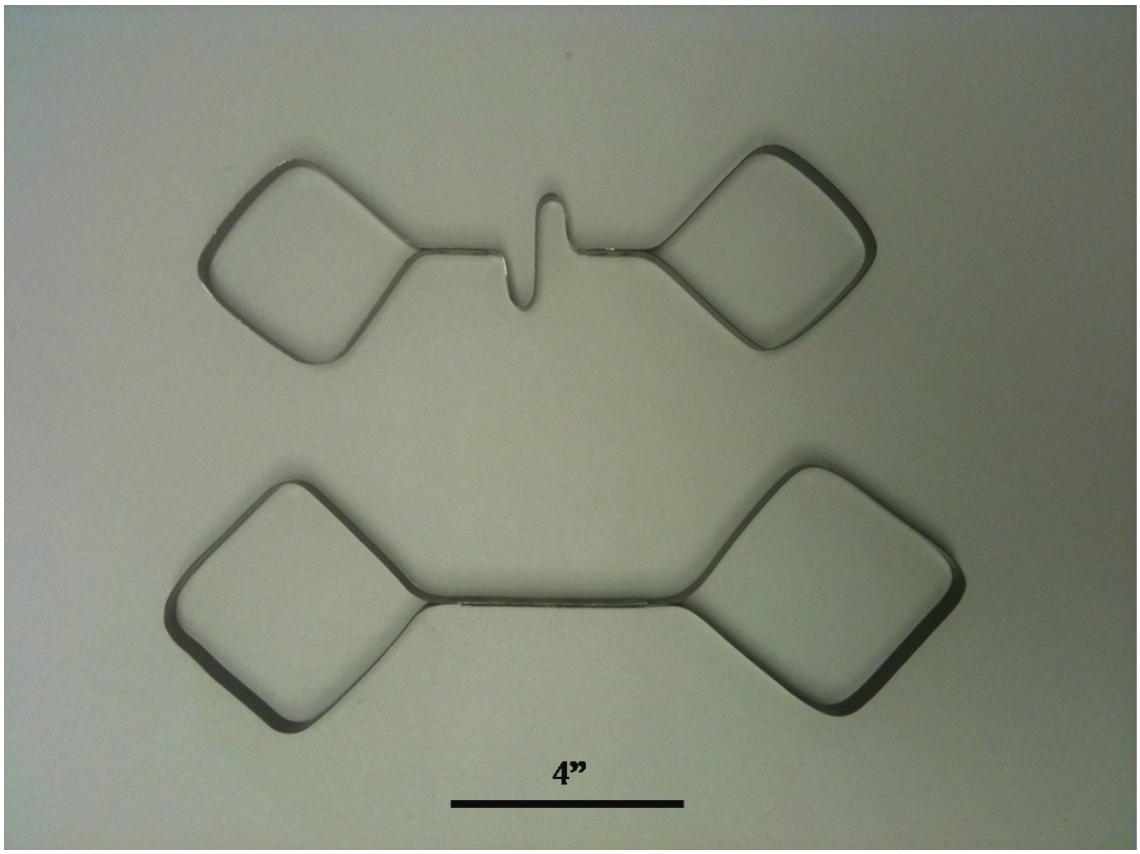

Figure 3.1.2 - Macro-Scale Shuttles

The servos used in the design of the macro-scale earthworm shuttle were HiTec heavy-duty analog servos (model HS-322HD); these servos are commonly used in remote controlled aircraft and other remotely controlled vehicles. The specifications of these servos can be found in Table 3.1.1.

Motor Type	3-Pole
Bearing Material	Nylon
Speed at 4.8V	0.19 sec @ 60deg
Speed at 6.0V	0.15 sec @60deg
Torque at 4.8V	42 oz/in (3.0 kg/cm)
Torque at 6.0V	51 oz/in (3.7 kg/cm)
Size	1.57 in X 0.78 in X 1.43 in (39.88 mm X 19.81 mm X 36.32 mm)
Weight	1.51 oz (42.81 g)

Table 3.1.1 - Servo Specifications [52]

Servos are controlled using positional data in the form of a pulse width train (PWT), which has a refresh rate of 50 Hz and a neutral pulse width centered at ~1500 μs; the operational voltage of these servos are in the range of ~5 V. For the servos used in the macro-crawler, the 0° and 90° signals used 690 μs and 1590 μs pulses respectively [53].

3.2 Experimental Set-up

A flowchart of the experimental set-up can be found in Figure 3.2.1. The experimental hardware, software, and procedures will be discussed in more detail in the following sections of this chapter.

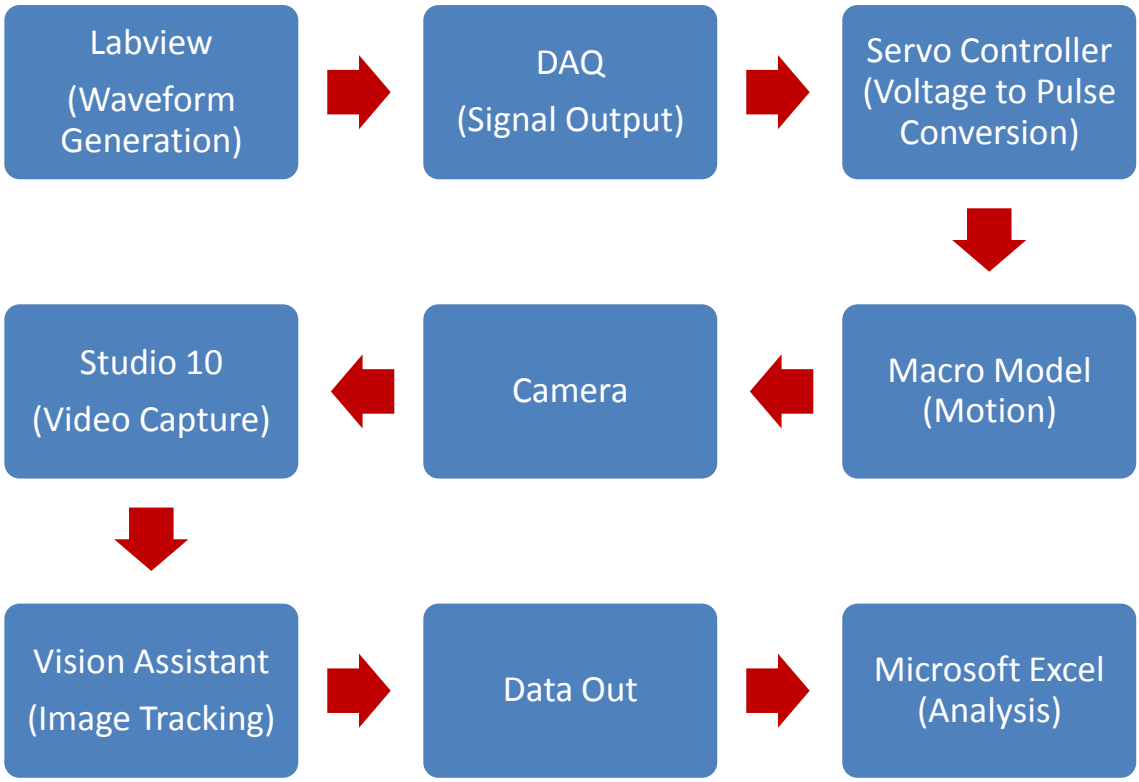

Figure 3.2.1 - Macro Testing Experimental Set-up Flowchart

3.2.1 Hardware

The software used to operate the macro-scale earthworm crawler, which will be discussed in Section 3.2.2, outputted a voltage signal through a National Instruments PCI-MIO-16E Data Acquisition Card (DAQ). Due to the requirements of a PWT for servo operation, a circuit was developed by Landry [54] to convert the DAQ's voltage output to a PWT. A photograph of circuit used can be seen in Figure 3.2.2. A diagram of the circuitry used to convert from Voltage to PWT can be found in Figure 3.2.3. A voltage of ~3 V produces a pulse width of ~1590 μs (90°), and a voltage of ~1.9 V produces a pulse width of ~590 μs (0°). Although there were four of the circuits shown in Figure 3.2.3 on the board in

Figure 3.2.2, meaning the board was capable of outputting a signal to four servos at once, the earthworm crawler was only connected to two of these outputs, since opposing pairs of servos on the crawler were connected together.

Figure 3.2.2 - Voltage to PWT Circuit (4" x 6")

A video camera (Sony Handycam Digital 8) was mounted directly over the macro-scale earthworm crawler using aluminum rods, as seen in Figure 3.2.4. The camera was then connected to the computer via a Pinnacle™ 640x480 pixel video capture card. To aide in optical tracking of the shuttle's position two additional steps were taken; as seen in Figure 3.2.5, these steps were:

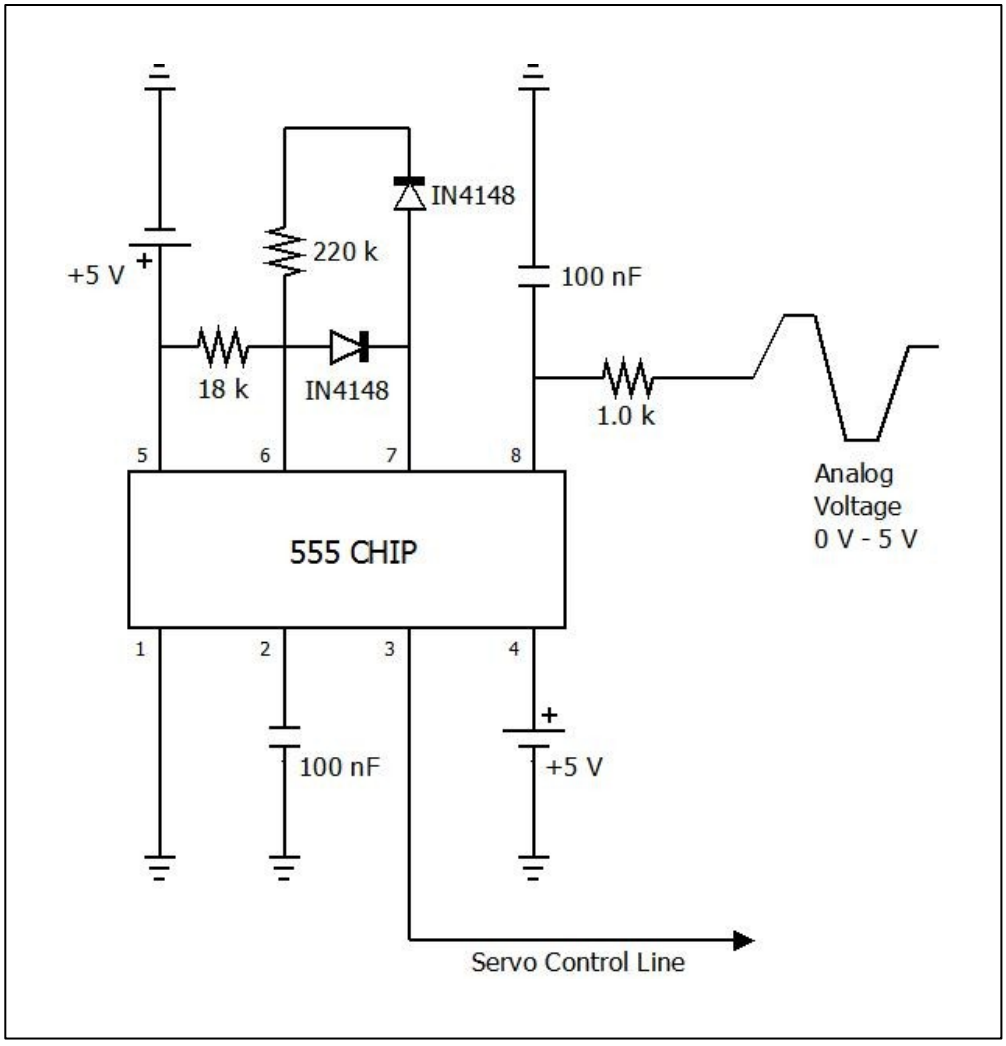

Figure 3.2.3 - Voltage to PWT Circuit Diagram [54]

- To increase the contrast of the image, a piece of plain white paper was affixed to the baseplate using double-sided adhesive tape.
- Small wooden blocks with black lines on them were attached to the ends of the shuttle in order to allow distinct shaped for the image-tracking software to follow. These shapes were different on each end to distinguish forward and backward motion.

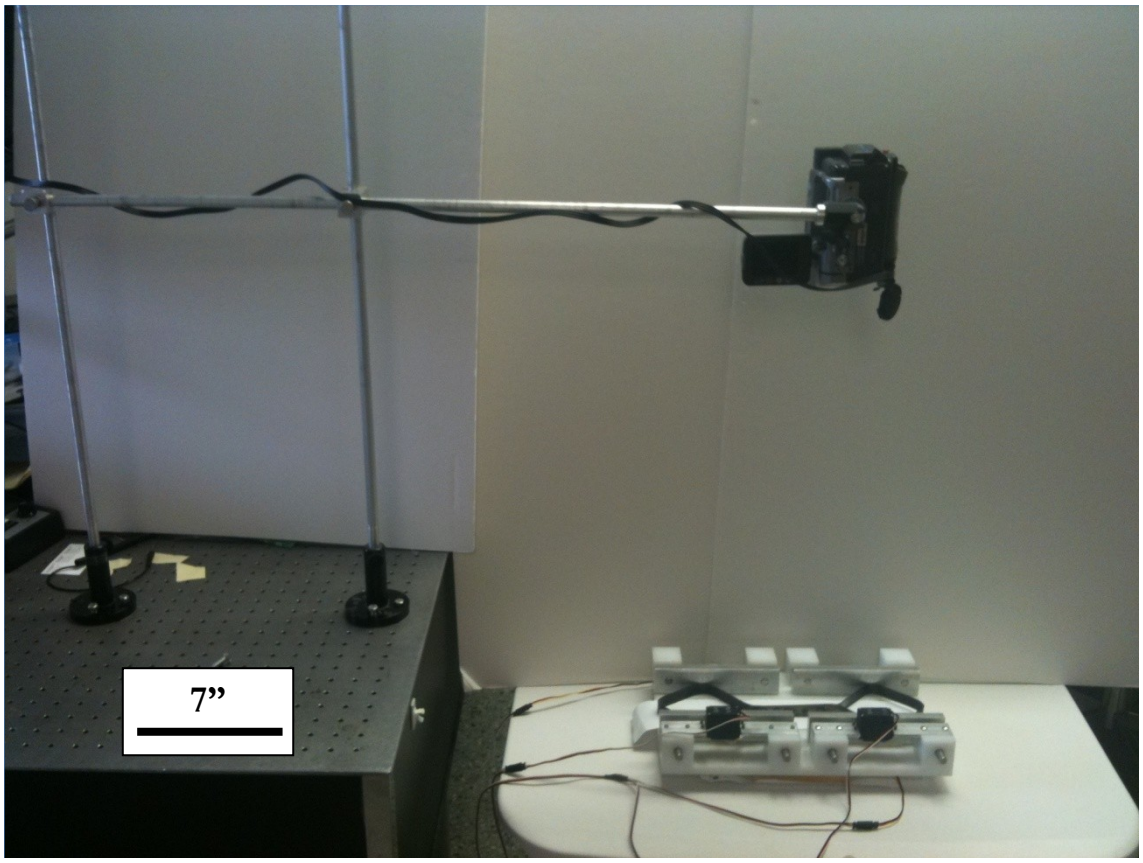

Figure 3.2.4 - Macro-Model Testing

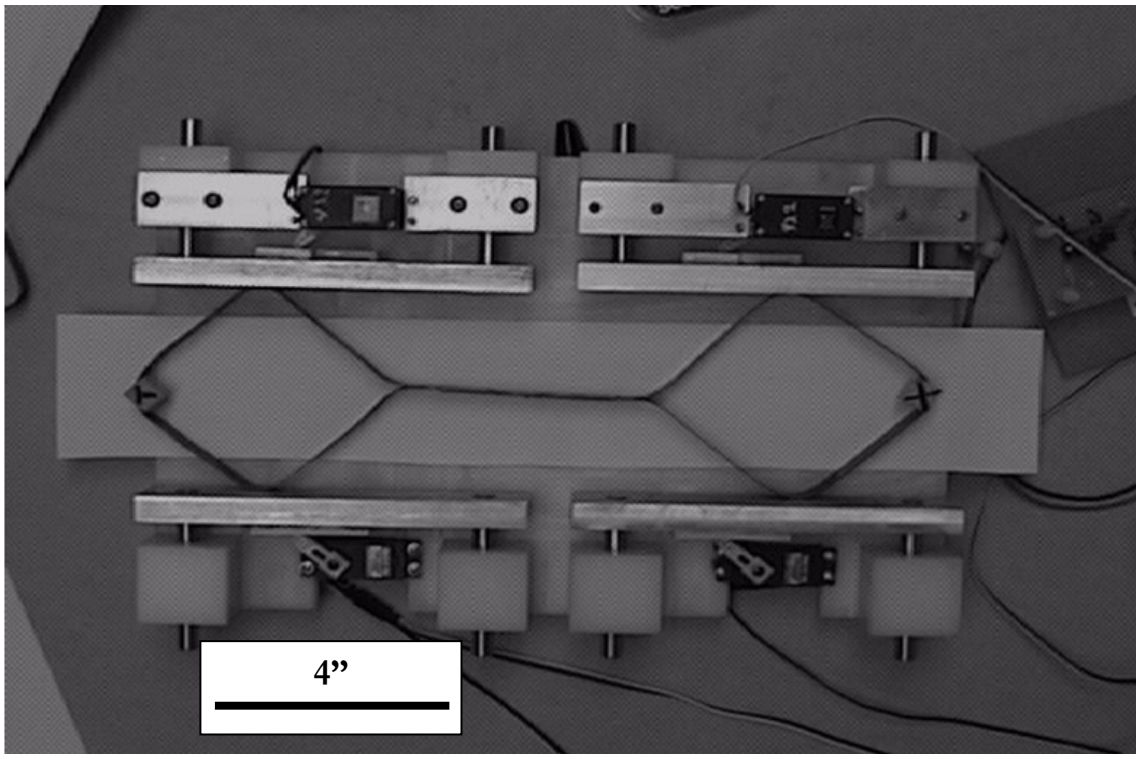

Figure 3.2.5 - Camera View of Macro-Scale Earthworm Crawler With Tracking Blocks

3.2.2 Software

Control of the macro-scale earthworm crawler was achieved via a customized National Instruments™ Labview Virtual Instrument (VI), a screenshot of which can be seen in Figure 3.2.6. This VI allowed variable frequency, as well as independently variable phase and range of motion for each of the servo pairs. Signal output was in the form of a square voltage wave, but with the rise and drop having a slight ramp. These ramps took ~8% of the total cycle to rise and ~8% to fall, and were intended to both avoid abrupt transitions and to account for the amount of time it took the servos to move. Direction change was achieved manually via a ‘direction switch’ on the Labview VI, which would change the signal phase differences from +90° to -90°, and was initiated once the crawler neared the end of its range.

The video taken during the experiments was recorded using Pinnacle Studio 10 with an .avi file extension. This file was then imported into National Instruments™ Vision Assistant, where the video's frames were separated into individual images. An image tracking script was then run on each image (frame) of the video. This script first converted the images to 8-bit greyscale; it then tracked a specified region of interest (ROI) in each frame and calculated x and y pixel displacements of the i^{th} frame ROI relative to the first frame's ROI. The pixel distances were converted to μm using a scale factor, and this data was outputted in the form of a text file. The output file from Vision Assistant was then opened using Microsoft Excel, where the data was analyzed.

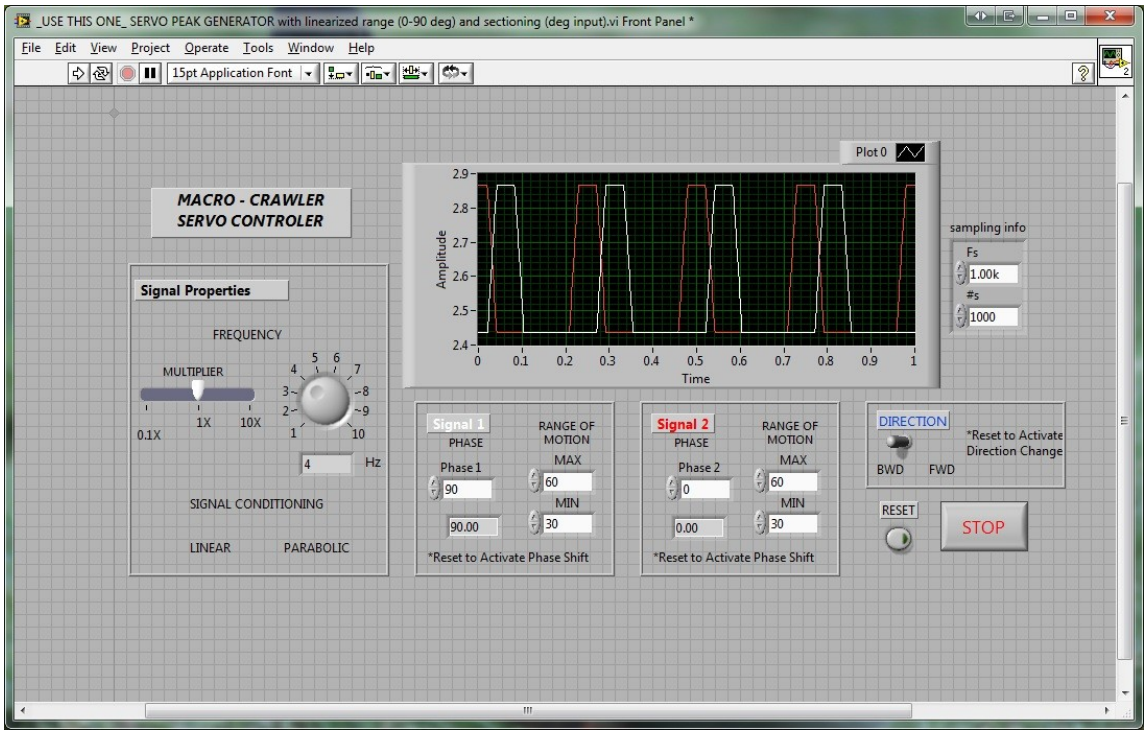

Figure 3.2.6 - Macro Testing Labview VI

3.2.3 Procedure

Following is the procedure that was used for all macro-scale earthworm crawler testing. The same procedure was used for tests run on both the shuttle with a spring, and without a spring.

First, the macro-model was placed in a sturdy surface and roughly levelled using blocks of wood. All electrical connections were made, then the video camera was set-up and connected to the computer; the camera was turned on, and manually focused so that the focus would not change during the experiment. The shuttle being used in the experiment was placed between the aluminum pusher bars; if there was an initial gap between the pusher and shuttle, the pushers were closed until they were just touching the shuttle by changing the servo start position using the Labview VI. Once all Labview inputs for the test being run were correctly set, the video capture was started, and the Labview VI was set to 'run'. Upon completion of the experiment, the Labview VI was set to 'stop', and video capture was ended; the video file was then saved with a name that was descriptive of the test's settings. Once all videos were recorded and saved, each file was imported into Vision Assistant, where the image tracking script was set to track one of the two blocks located on the shuttle and run. Once image tracking of all video files for an experiment were completed, they were individually opened using Excel where they were analyzed.

3.3 Scale Model Results

Testing was initially conducted to determine if there was a requirement for a shuttle with, or without a spring. While the graph showing the comparison of the two shuttles will

appear later in this chapter, it should be noted that little difference was seen between the two shuttles, which is why only the data for the shuttle without a spring is being shown.

The operational frequency of the crawler was set to 2 Hz, and the phase difference between the signals was varied from 75-110 Hz; the results of this can be seen in Figure 3.3.1. While a slight decreasing trend was observed, it was decided that for the purposes of simplicity, all further experiments would occur with the two signals 90° out of phase.

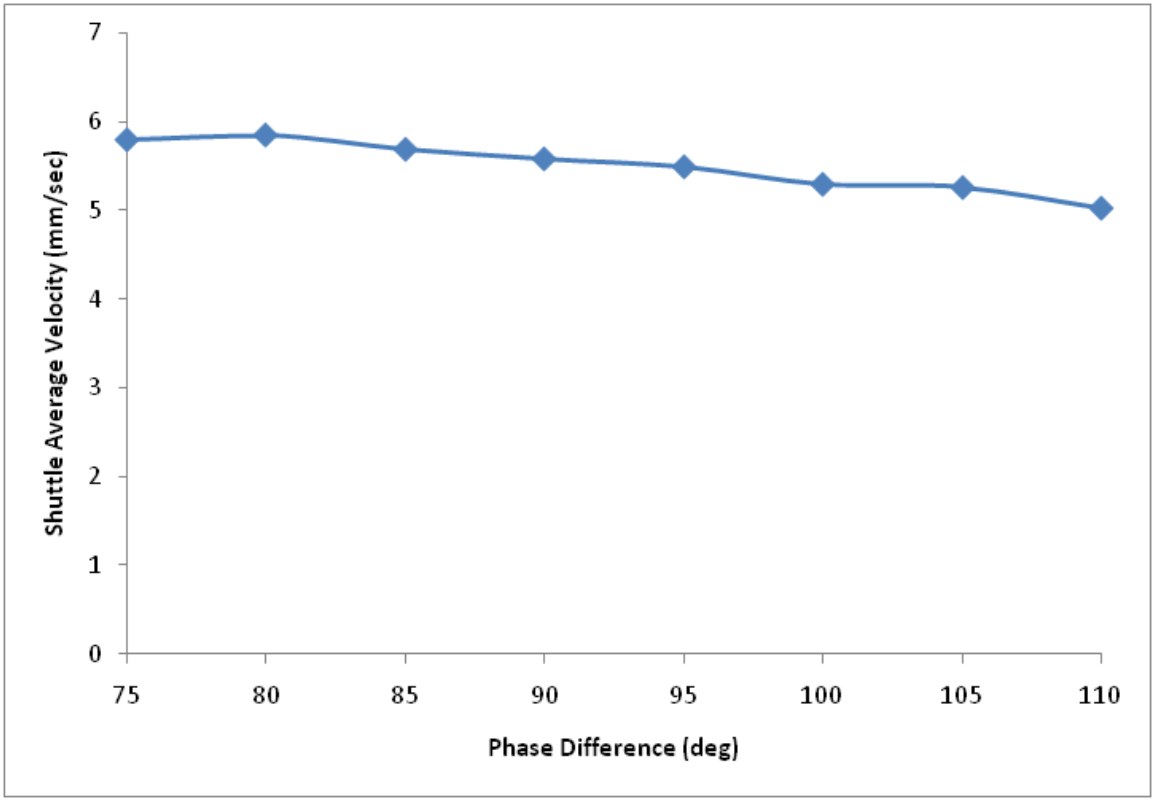

Figure 3.3.1 - Macro Crawler Velocity vs. Phase

Figure 3.3.2 shows the recorded shuttle motion in 3 steps at a 1Hz input frequency. The numbers 1, 2, 3, 4, 5 refer to the stages in Figure 2.1.1. The 5 stages in Figure 2.1.1 are identified in Figure 3.3.2, and are found in reverse order since the shuttle is moving to the left. This proof of concept plot shows that using peristaltic motion derived from the movement of earthworms, it is possible to move a shuttle with two diamonds at the macro-scale; in the case of this experiment, with a step distance of approximately 3 mm. When these steps are combined, long range motion is possible. Figure 3.3.3 shows ~17 steps backwards and ~17 steps forwards, again with an input frequency of 1Hz.

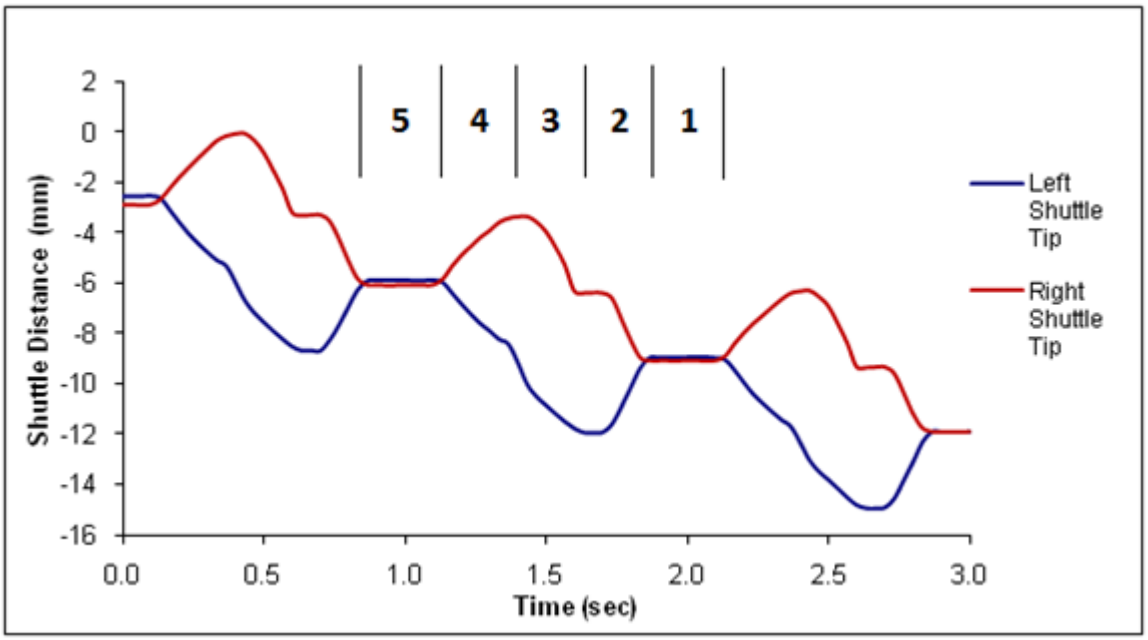

Figure 3.3.2 - Macro Crawler Step Plot

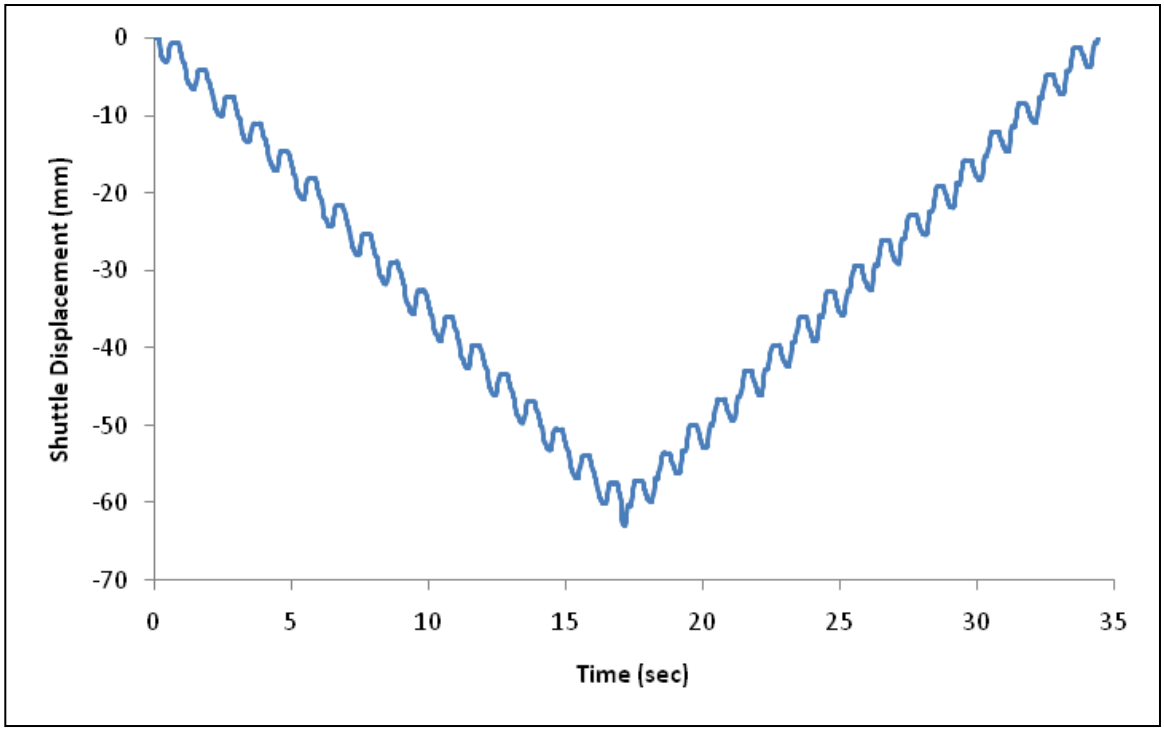

Figure 3.3.3 - Macro Crawler Backward and Forward Motion

The Shuttle's input frequency was varied, and the shuttle's velocity in both the forward (to the right) and backward (to the left) direction were measured, with the results shown in Figure 3.3.4. The differences in velocities in each direction (~15% at higher frequencies) can be the result of many things:

- While the base plate and pushers are accurately made and mounted, the diamond springs were hand assembled and may have had significant variations in the shuttle geometries or mechanical properties (one diamond larger or softer than the other).
- Slight variations in the servo outputs.

- Slight differences in the electrical signals from the DAQ card, or the Voltage to PWT circuit.

In both the forward and backward cases, the shuttle velocity varied linearly with the input frequency at low frequencies; however, the velocity increase began to slow at higher frequencies, and began to decrease past a frequency of ~5 Hz due to the servo's limited speed capacity.

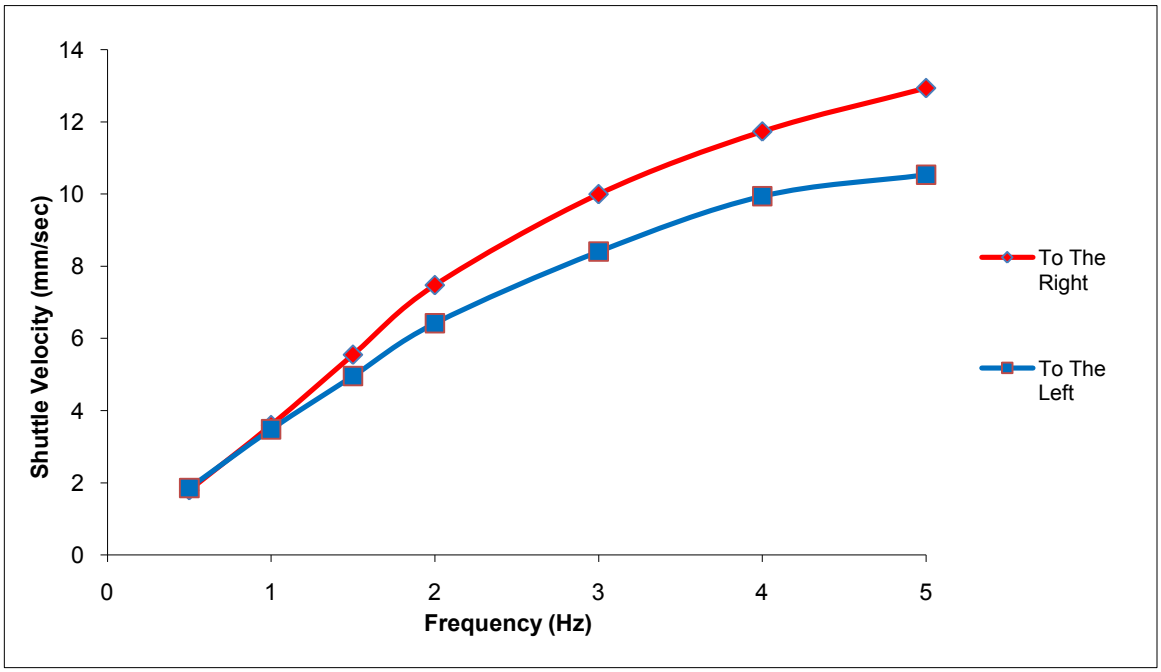

Figure 3.3.4 - Macro Velocity vs. Frequency (Forwards and Backwards)

The forward and backward velocities were averaged and plotted for both the shuttle with a spring and the shuttle without a spring; the results of this can be seen in Figure 3.3.5. It can be seen that there is little difference between the velocity profiles of either shuttle.

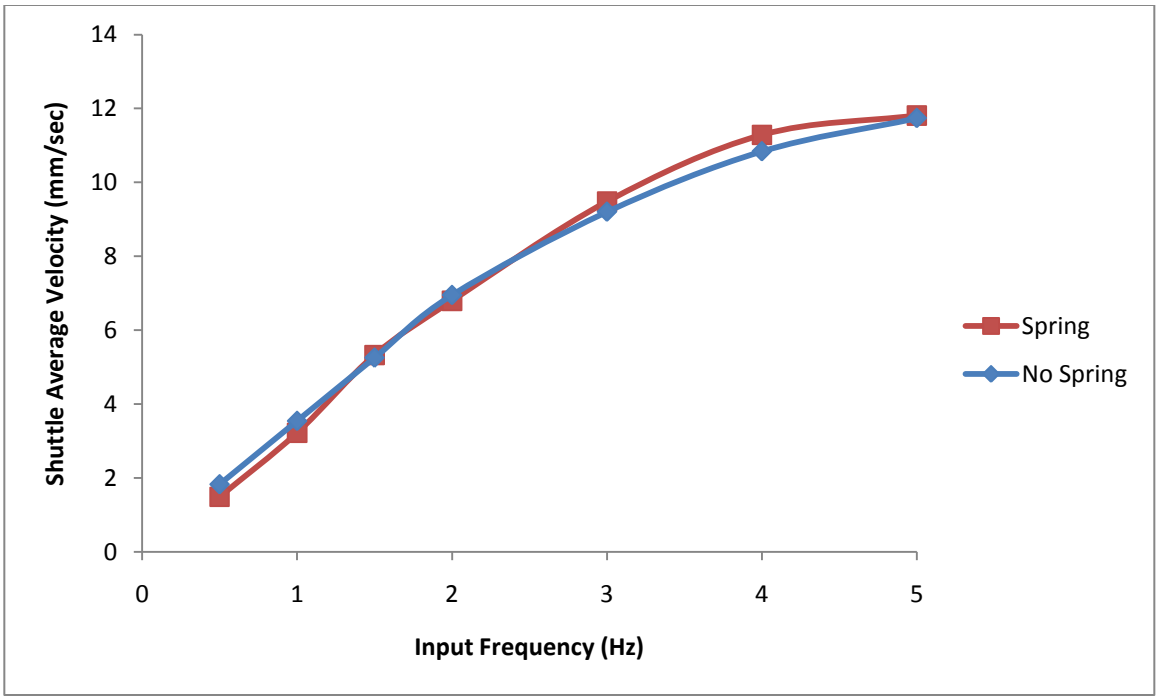

Figure 3.3.5 – Macro Velocity vs. Frequency (Spring and No Spring)

3.4 Scale Model Conclusions

The macro-scale testing confirmed that the theory behind the earthworm crawler's motion is sound, and that the individual steps can be summed to produce long-range motion. A slight difference in velocity was found between motion in the forwards and backwards directions, which can be explained by variations in the experimental hardware. The crawler's peak operating frequency was ~5 Hz, due to the speed of the servos used. It was shown that there was no requirement for a spring between the shuttle's two diamonds for crawler operation, which will help to reduce the micro-scale crawler's complexity.

Chapter 4: MEMS Earthworm

This chapter covers the selection of a MEMS process for the fabrication of the micro-scale earthworm crawler, as well as the selection of an actuator for its motion. It will also describe the additional steps taken in the crawler's design to ensure the greatest chance of device success.

4.1 MEMS Earthworm Process and Basic Actuator Selection

While some preliminary testing for the MEMS earthworm crawler was completed using the SOIMUMPs process, due to complications with debris on the chips and as additional process restrictions, such as only being able to etch a maximum of the 33% of the chip area, this process was abandoned. More information on the SOIMUMPs earthworm crawler can be found in Appendix C. Since the Dalhousie University MEMS Lab is restricted to the services offered by CMC, the two remaining options for fabrication were MetalMUMPs and PolyMUMPs. As described in Section 1.6, MetalMUMPs has an 8 μm minimum feature size, meaning that if the earthworm crawler were fabricated using this process, it would be quite large and stiff. PolyMUMPS, with it additional layers and 2 μm minimum feature size, allowed a versatile design that could fit into a small footprint. This, combined with the familiarity of the Dalhousie University MEMS Lab, led to the adoption of the PolyMUMPs process for the MEMS earthworm crawler.

Although, as described in Section 1.5.1, ECD actuators provide much larger displacements than Chevron-type thermal actuators (10-20 μm vs. 2-6 μm) they have much lower forces (~5 μN vs. 100-200 μN) and take up a larger footprint. Electrostatic actuators also require large supply voltages that require power supplies that the Dalhousie MEMS Lab

does not easily have access to. Chevron-type thermal actuators were chosen to power the MEMS earthworm crawler due to their small size, relatively large force, linear operational path, and reliable operation. These actuators have been used many times in previous frictional crawler designs tested in the Dalhousie MEMS Lab, and are therefore well understood. The final crawler design is described in detail in Section 4.2.

4.2 MEMS Earthworm Design and Fabrication

The chevron actuators used to power the MEMS earthworm crawler uses four Poly 1 beams on each side that are 150 μm long, and 2 μm square in cross-section; these beams are bent at a 6° angle. This chevron geometry produces ~2 μm of motion with 7 V supplied. At the midpoint of each actuator is attached a horizontally elongated triangular lattice structure, which acts as pusher bar; this allows the actuators to squeeze the shuttle over a wide range of lateral positions. Figure 4.2.1 shows an image of the chevron and lattice structure as laid out in the program used to design micro-scale devices in the Dalhousie MEMS Lab (L-Edit); it should be noted that the L-Edit images do not always show all details of the design, particularly when zoomed out. Figure 4.2.2 shows a Scanning Electron Microscope (SEM) image of the same area on the fabricated chip. As seen in Figure 4.2.2, two small dimples were added to the center portion of the chevron to prevent stiction to the chip's surface during operation; as well, a small strip of Poly 2 was added to the front of the lattice structure to increase its height. This double-height approach will be discussed later in this section.

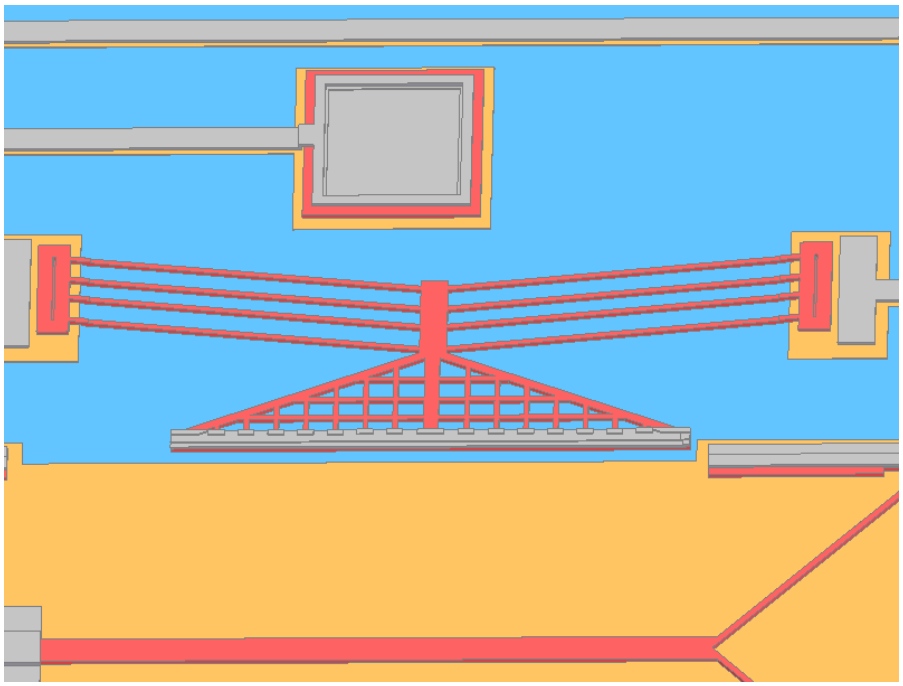

Figure 4.2.1 - 3D Diagram of Chevron TA and Lattice Extension

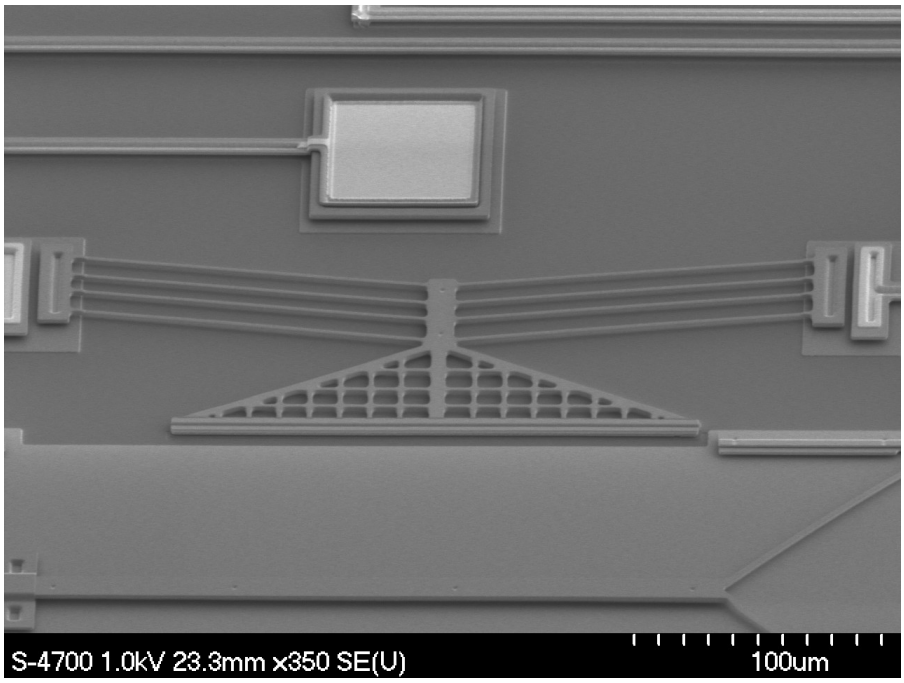

Figure 4.2.2 – Tilted SEM Photo of Chevron TA and Lattice Extension.

The shuttle consists of two 200 x 200 μm diamond shaped flexible structures connected by a 300 μm long stiff central bar, for a total shuttle length of 700 μm; the shuttle members are 2 x 2 μm in cross section, and are fabricated from Poly1. Figure 4.2.3 and Figure 4.2.4 show an overhead view of one of the shuttle's diamonds. The shuttle is designed with dimples that help to reduce the effects of stiction, as well as beneficially change the post-release device height; this post-release height will be discussed later in this section.

To constrain the shuttle's motion during testing, the shuttle was constructed with two 'hasp' structures covering the stiff bars affixed to one end of each diamond. These hasps, one of which can be seen to the right of the shuttle diamond in Figure 4.2.3 and Figure 4.2.4, is made from Poly2 and anchored to the substrate. They serve two main purposes: to guide the earthworm between the pushers during assembly, and to keep the earthworm on the chip in the event that it gets bumped by a probe needle during operation. A side-on view (at an angle 45° from the surface) of one hasp can be seen in Figure 4.2.5 and Figure 4.2.6; from these figures, it can clearly be seen how the hasp helps to keep the shuttle in place.

For the operation of the micro earthworm crawler, it is desirable to have large vertical contact heights. For this reason, the contacting edges of both the shuttle and pushers were made as double-height (both Poly1 and Poly2) structures. This is done by overlaying a patch of Poly2 on top of the contacting edge, and connecting it to the Poly1 layer using PolyMUMPs' Poly1-Poly2VIA feature. This change allows a design to have a double-height structure to have a thickness of 3.5 μm, as opposed to a single-height Poly1 thickness of 2.0 μm. A side-on view of these double-height contact patches can be seen in Figure 4.2.7 and Figure 4.2.8.

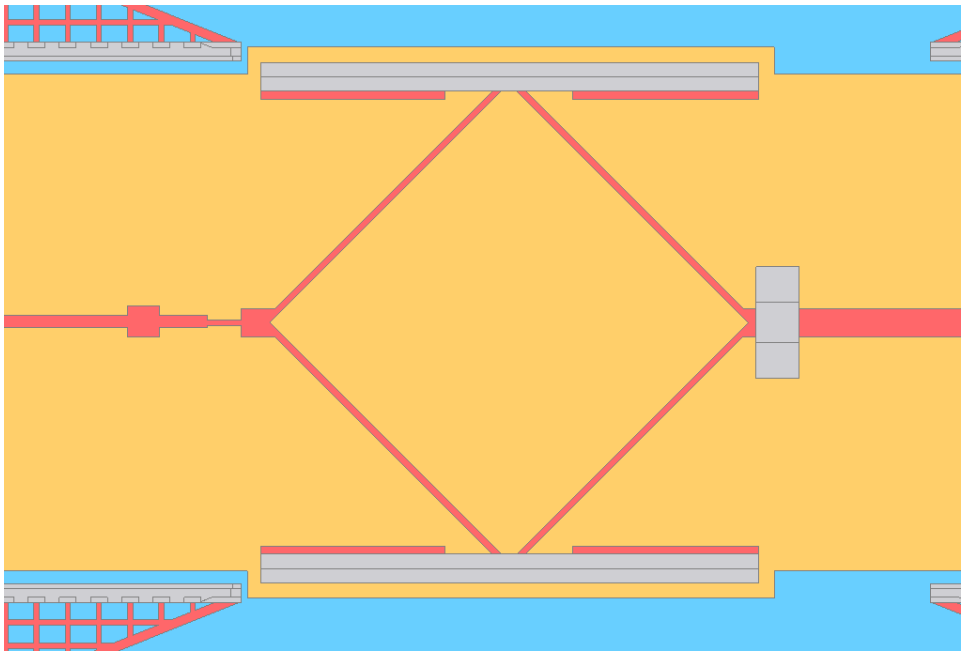

Figure 4.2.3 - Diagram of One Diamond of Earthworm Shuttle

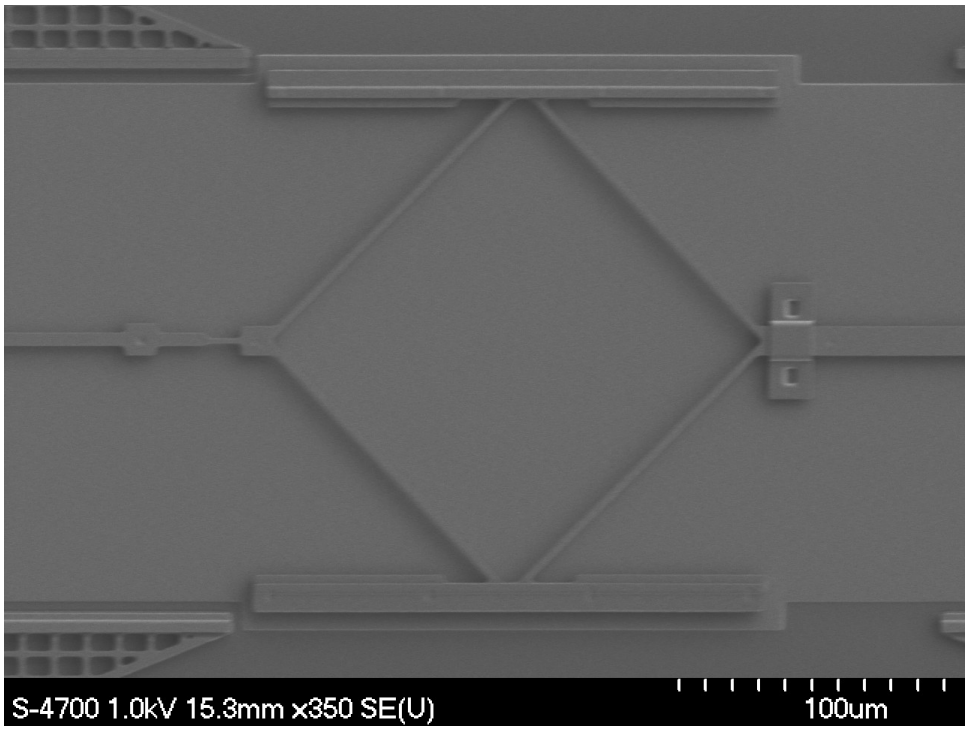

Figure 4.2.4 - SEM Photo of One Diamond of Earthworm Shuttle

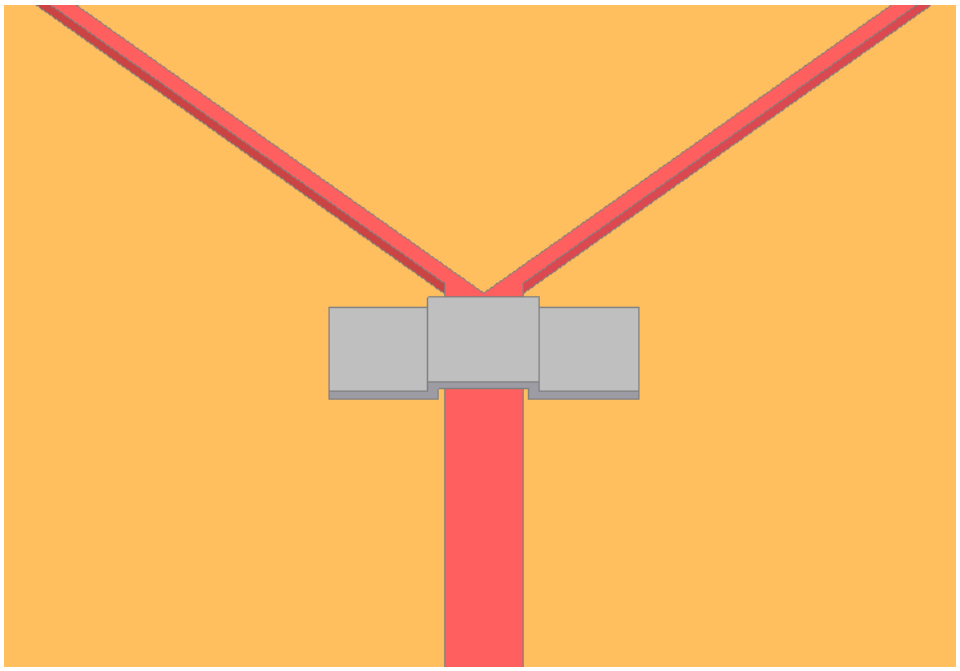

Figure 4.2.5 - Diagram of Hasp Used to Contain Shuttle

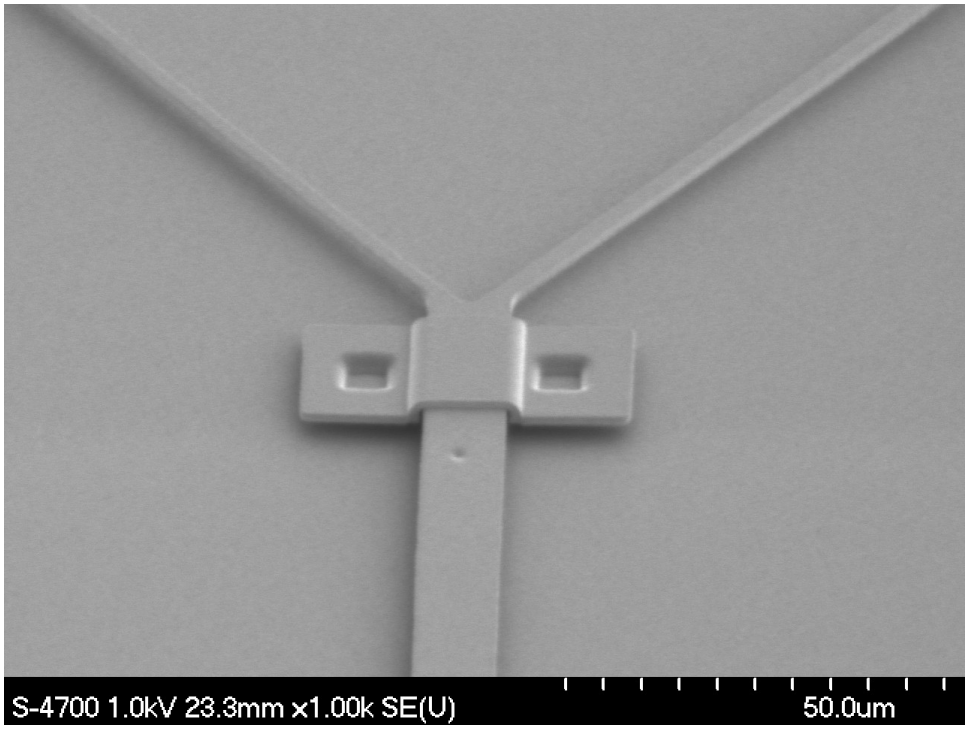

Figure 4.2.6 - SEM Photo of Hasp Used to Contain Shuttle

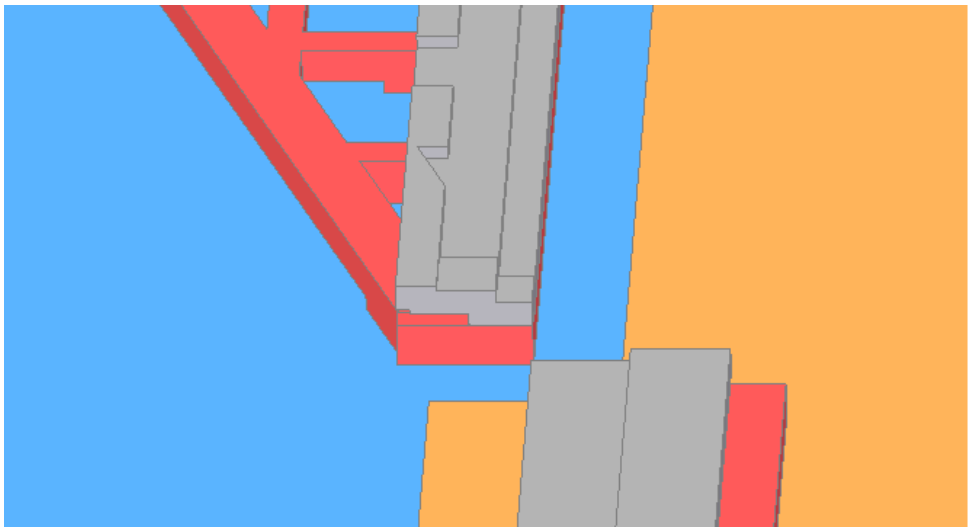

Figure 4.2.7 - Diagram of Double-Height Structure

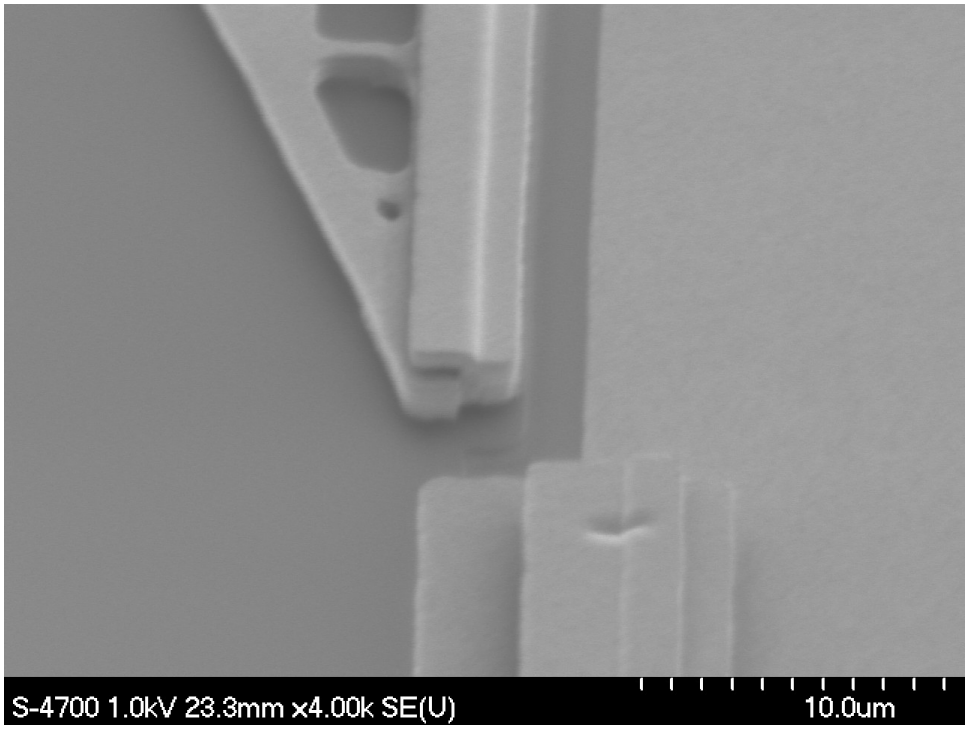

Figure 4.2.8 - SEM Photo of Double Height Structure

Because the pushers are cantilevered structures attached to the substrate, and the shuttle is a free structure, they will not necessarily be at the same height above the substrate; when the shuttle is released during fabrication, it will drop down and be vertically offset from the pushers. In the simplest design, these two structures would have a vertical mismatch of approximately 1.25 μm, or nearly 1/3 of their thickness. In order to have both the shuttle and the pusher's contact edges at the same height from the chip's substrate, a combination of layers were used. For the shuttle, the entirety of the shuttle was raised 0.5 μm using on a Poly0 pad, and small dimples were used to raise the height of the shuttle by a further 0.75 μm once the HF release was completed and the device was assembled. For the edges of the pushers, the entire contact edge was lowered by 0.75 μm through the use of a large rectangular shaped patch of the 'Dimple' layer; this layer was used exclusively for height reduction, and did not contribute to the reduction of device stiction. The combination of these geometries resulted in both the shuttle and pusher edges being aligned after they were released and ready for testing. Figure 4.2.9 shows the edge heights before the HF release and device assembly, and Figure 4.2.10 shows the aligned devices once the crawler is ready for testing; the double-height contact edges can also be seen in these images. The colors in these figures correspond to the PolyMUMPs layers shown in Figure 1.6.3.

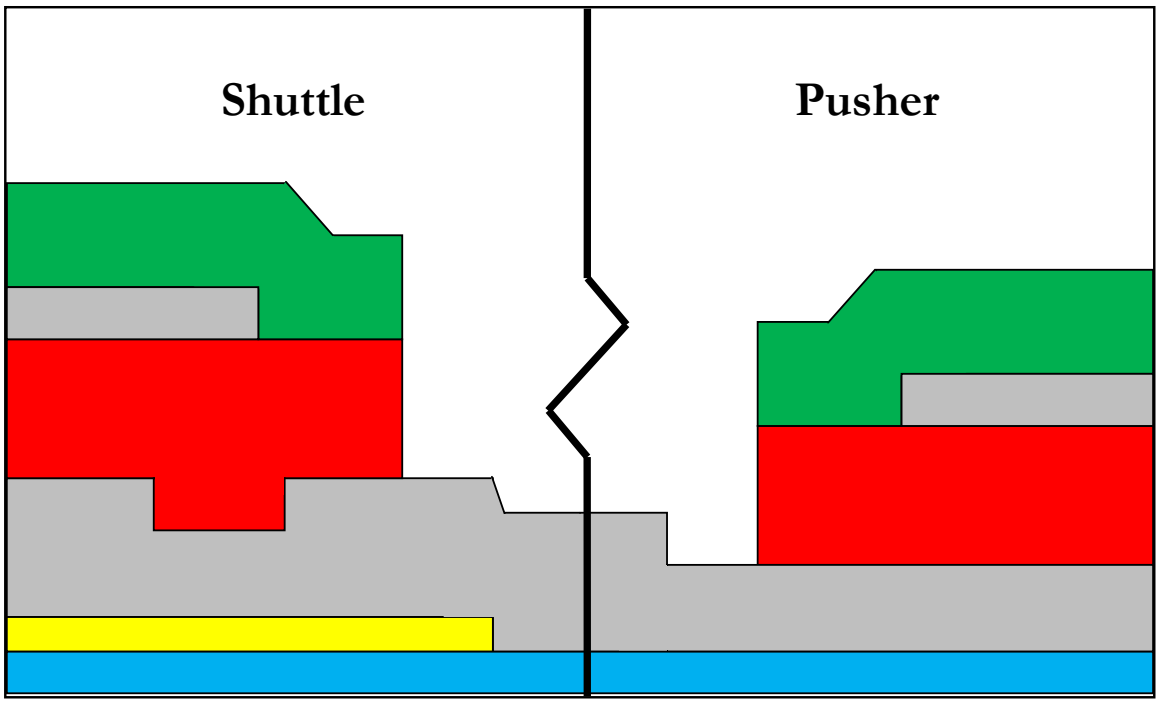

Figure 4.2.9 – Micro Crawler Layer Heights Pre-Release

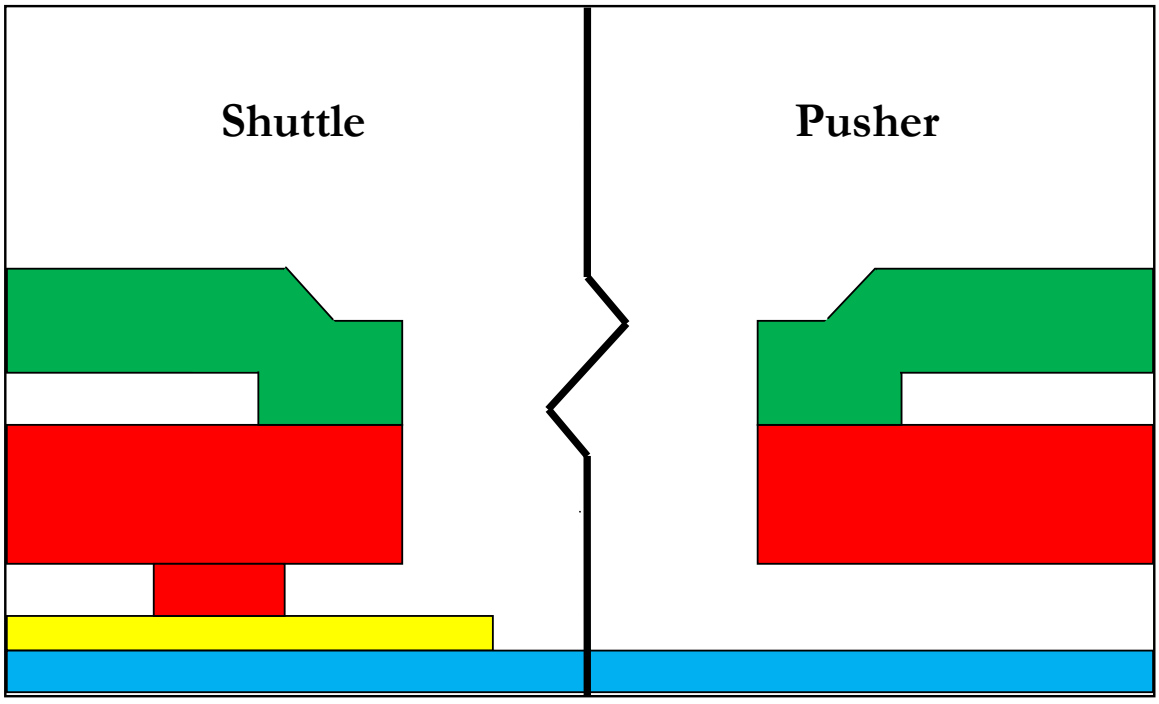

Figure 4.2.10 - Micro Crawler Layer Heights Post-Release

To prevent damage to the shuttle during shipping, it was affixed to the chip's substrate using breakable Poly1 tethers. These thin beams hold the shuttle in place beside the actuators until the crawler is ready to be tested, at which point they are manually snapped off using probe needles and the shuttle is pushed to its final position between the actuators. Figure 4.2.11 and Figure 4.2.12 show one of the tethers used to hold the shuttle in place; there are two small tethers used to hold the right hand side of the shuttle in the figures (one on each side of the stiff bar), and a long 'T-shaped' tether is used to hold the left hand side. On long tethers, dimples are used to ensure that the tether does not stick to the chip's substrate which would prevent their removal; these dimples can be seen in Figure 4.2.11 and Figure 4.2.12, appearing as five small squares on the tether.

The micro earthworm crawler is electrically powered with three connections: Signal 1, Signal 2, and a ground. The two left-most chevron connections in Figure 4.2.13 and Figure 4.2.14 are joined and wire-bonded to one of the chip's 68 Pin Grid Array (PGA) pins (Signal 1), the right-most two chevron connections are joined and wire-bonded to another of the chip's 68PGA pins (Signal 2). The two larger middle chevron connections are connected to large pads for contact with probe needles (one on the top of the crawler, and one on the bottom of the crawler) and are used as electrical grounds. The grounds were designed to be connected with probes as opposed to a PGA pin due to the added complexity of requiring jumpers when one wire runs under another.

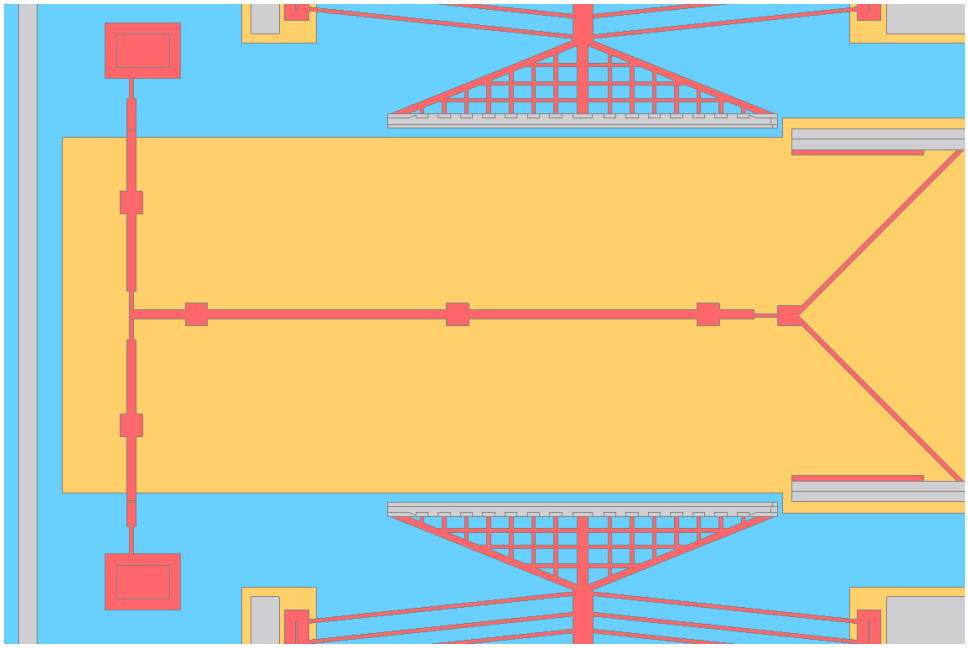

Figure 4.2.11 - Diagram of Break-away Tether

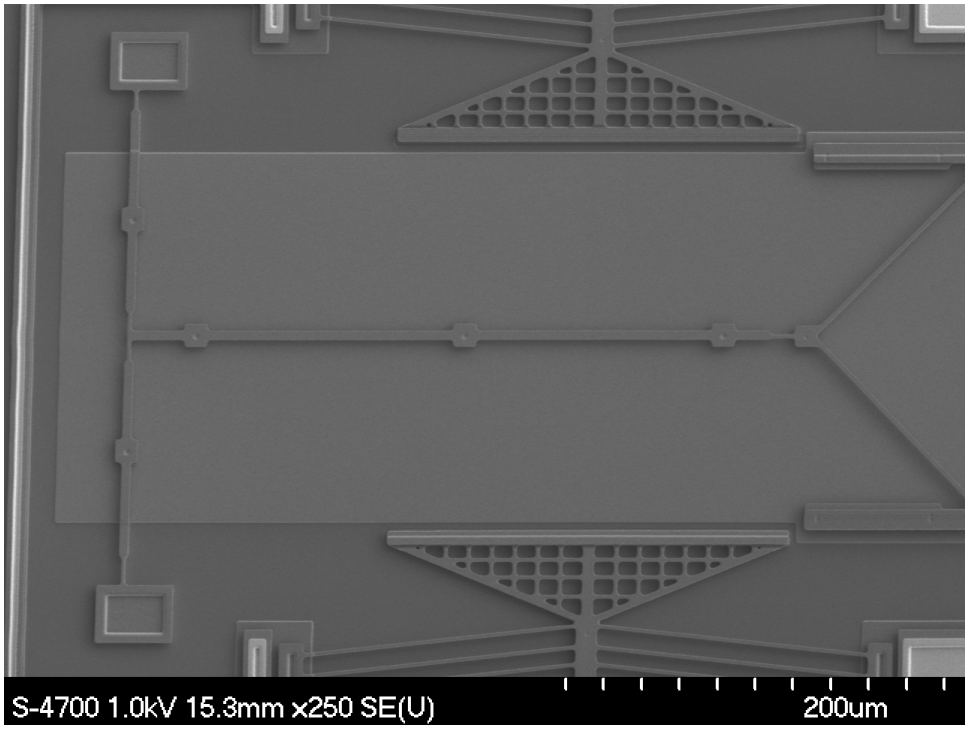

Figure 4.2.12 - SEM Photo of Break-away Tether

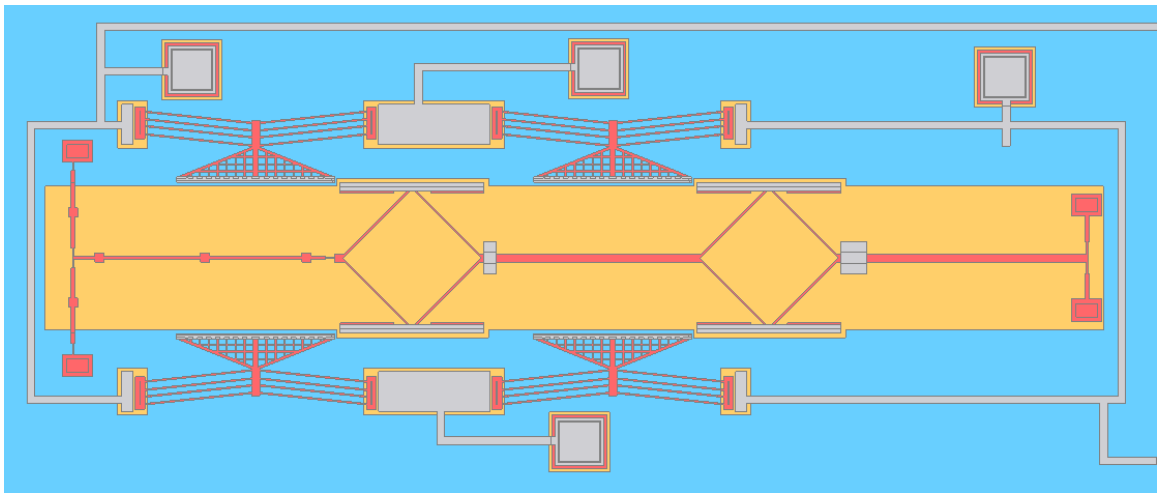

Figure 4.2.13 - Diagram of Complete Earthworm Micromotor (Before Assembly)

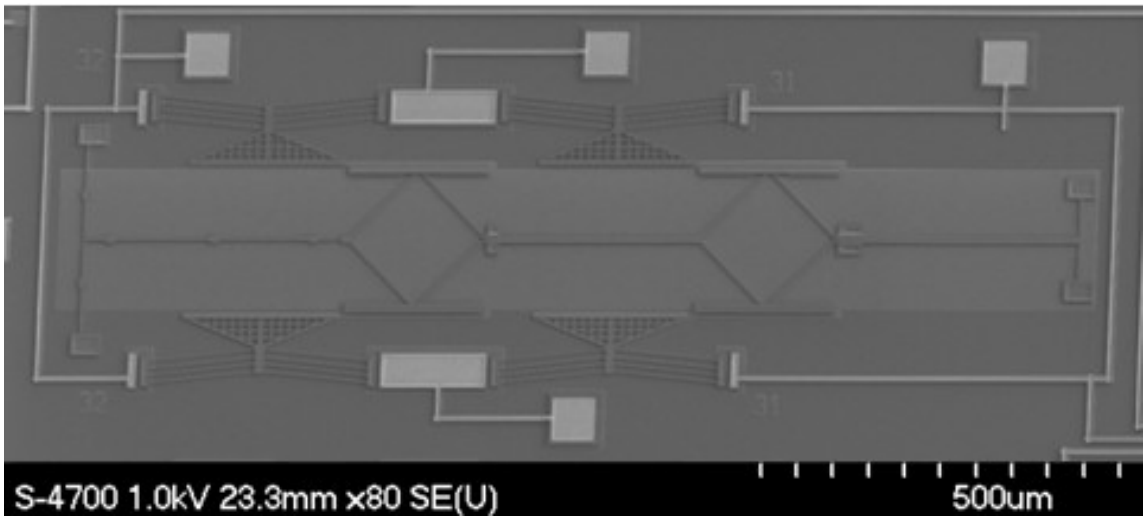

Figure 4.2.14 – SEM Photo of Complete Earthworm Micromotor (Before Assembly)

The crawler was designed such that, even when the shuttle was in place between the pushers, there would still be a small gap between the contact surfaces on the shuttle and the pushers (0.5 μm on each side of the shuttle). This gap is intended to ease in the assembly of the crawler for testing, and to help prevent stiction issues between the shuttle and pushers; however, since the chevrons have a finite range, this gap would lessen the total amount that the shuttle could be squeezed by the chevrons.

Chapter 5: Experimental Set-up

This chapter covers the experimental set-up used to test the micro-scale earthworm crawler. It includes the assembly of the crawler itself, as well as the process used for both velocity and force testing.

5.1 Device Assembly

Devices fabricated through CMC are made off-site, and then shipped to the Dalhousie MEMS Lab; for this reason, devices are frequently designed in an un-assembled state, with individual components tethered to the chip's surface so they do not become damaged during shipping. This means that before a micro-crawler could be tested, it first had to be assembled.

The 68PGA chip containing the MEMS Earthworm crawler was placed in a Zero Insertion Force (ZIF) socket located on a Wentworth™ Probestation Model 901 microscope owned by the Dalhousie MEMS Lab; the chip and ZIF socket can be seen in Figure 5.1.1. Once the chip was securely located on the probestation's cross-slide, three probes (Wentworth™ Model PRO195RH/PRO195LH) with 0.30 mm dia X 50 mm long stainless-steel J-type acupuncture needles were used to break the tethers and slide the shuttle to its final position. It was found that in all cases, in-plane (x-y) motion was much more effective at cleanly breaking the tethers than out-of-plane (z) motion. Frequently, the crushing motion of out-of-plane motion would damage the chip's surface, causing poor operation of the earthworm crawler. Figure 5.1.2 shows the probestation with the three probes used to assemble the crawler, while Figure 5.1.3 shows the probe needles positioned on the chip for device assembly.

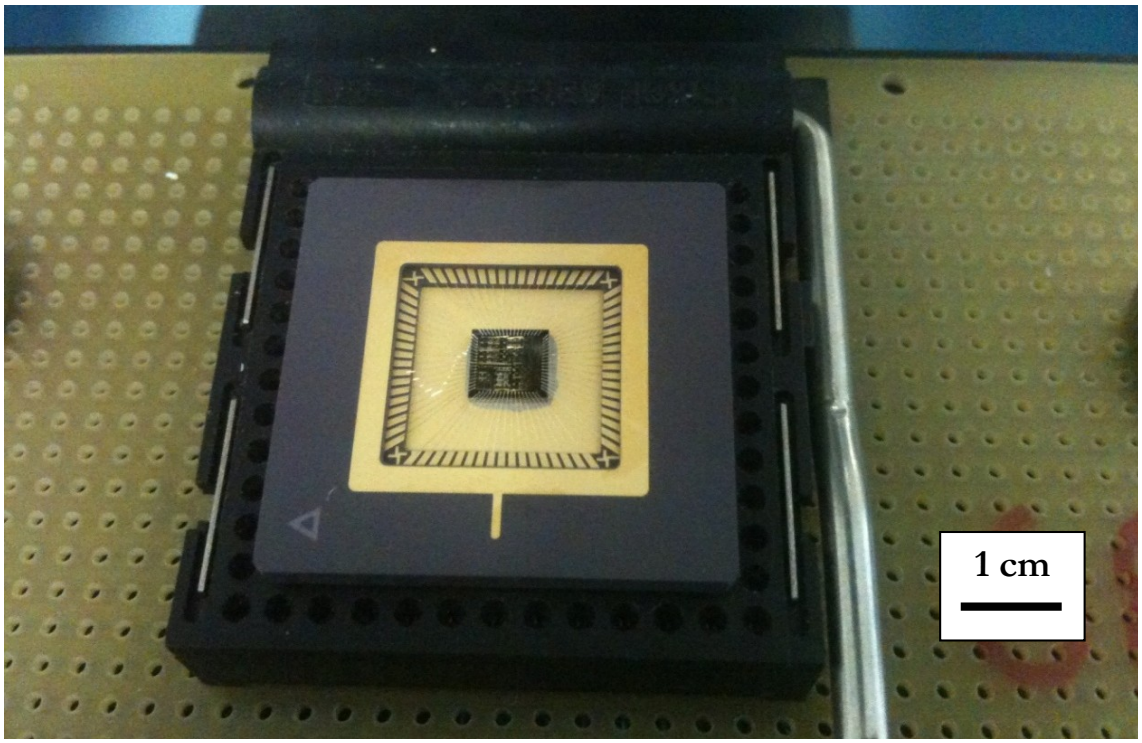

Figure 5.1.1 - MEMS Earthworm Chip and ZIF Socket

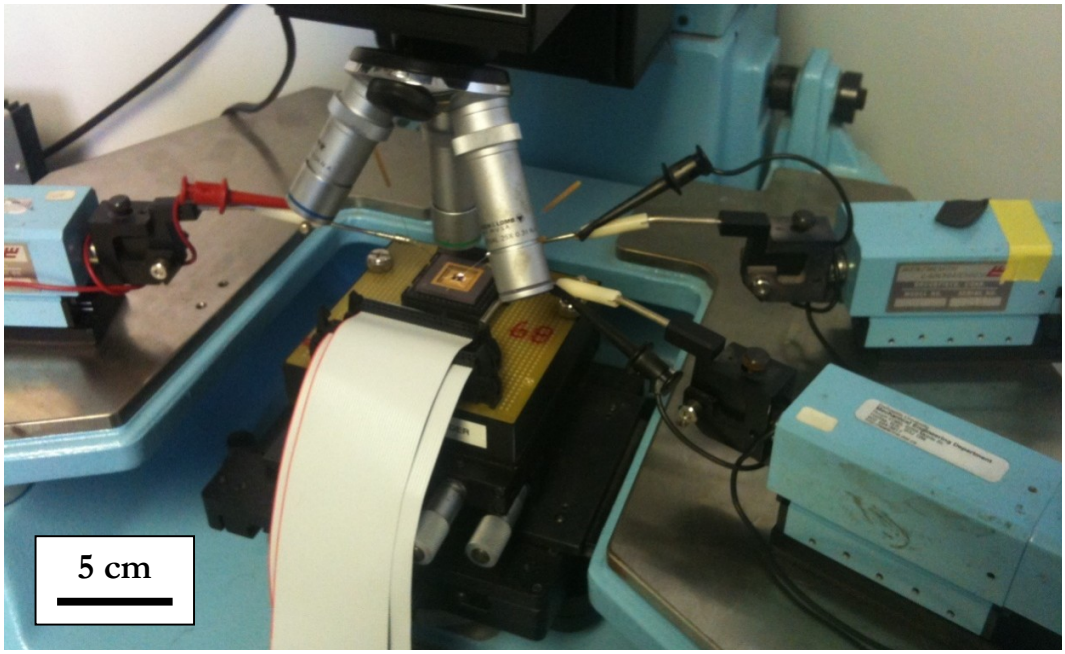

Figure 5.1.2 - Probes Used For Micro-Crawler Assembly

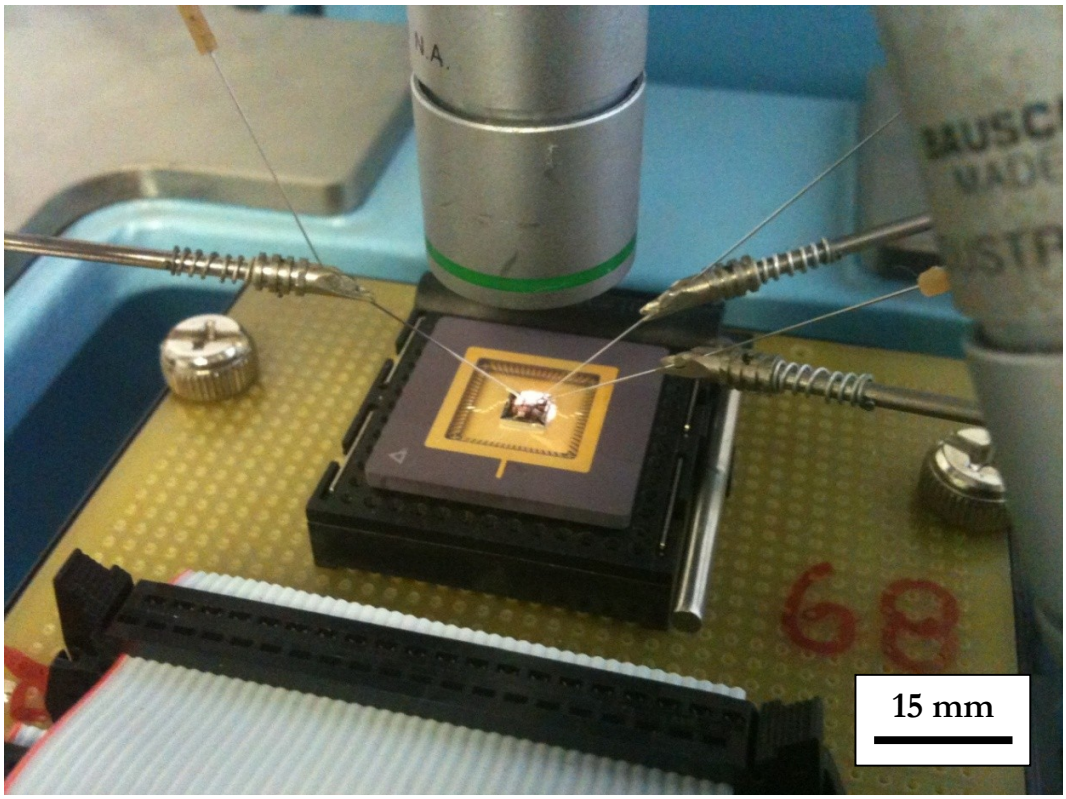

Figure 5.1.3 - Probe Needles Used for Micro-Crawler Assembly

First, the tethers located on the right-hand side of the earthworm shuttle were broken; an image of the tethers before they were removed can be found in Figure 5.1.4. To break these two small tethers, as seen in Figure 5.1.5, a probe was used to push the right-hand end of the shuttle to the left. If both tethers did not break-off completely, a second probe was used to break off the remaining piece of tether while the first probe remained to prevent the shuttle from sliding. This two-probe approach can be seen in Figure 5.1.6, where the needle on the right is being held stationary to prevent the shuttle from sliding, while the left hand needle moves to the right to break the remaining tether. Figure 5.1.7 shows an image of the shuttle once both tethers on its right hand end were removed.

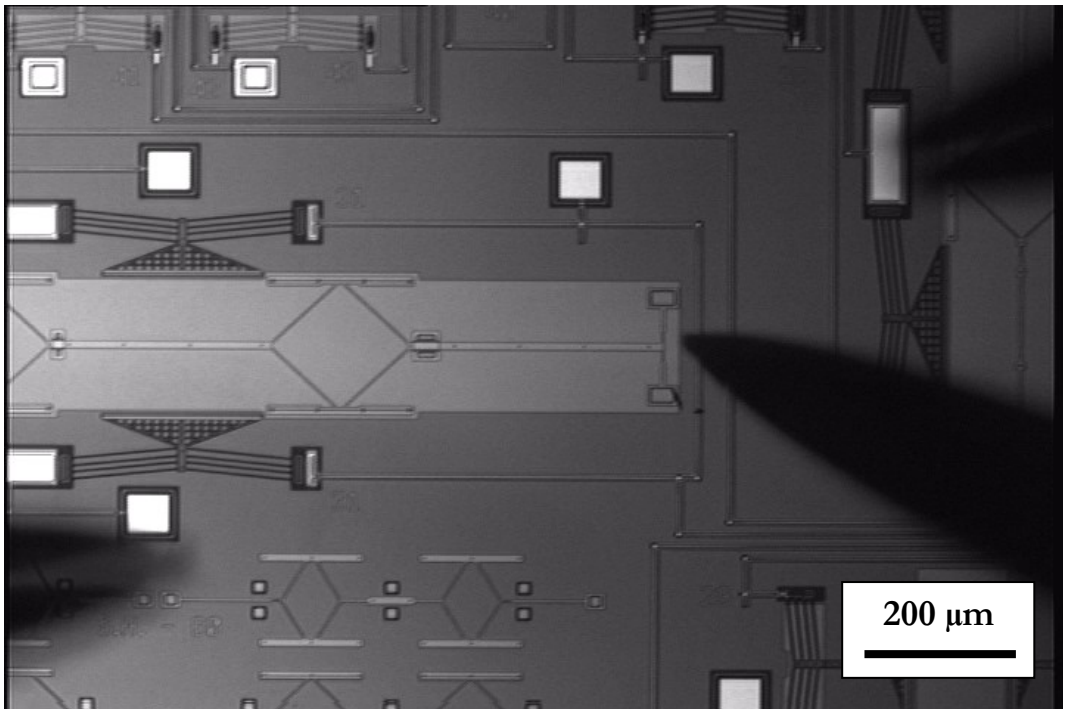

Figure 5.1.4 – Before Breaking Right Hand Tethers

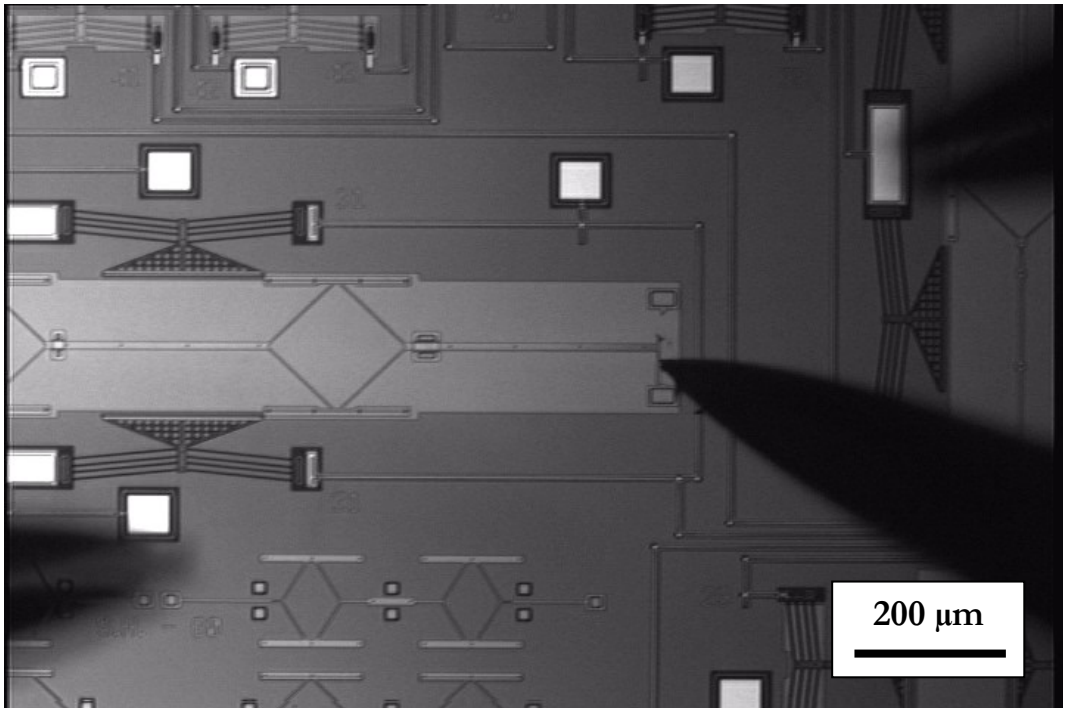

Figure 5.1.5 - Breaking First Right Hand Tether

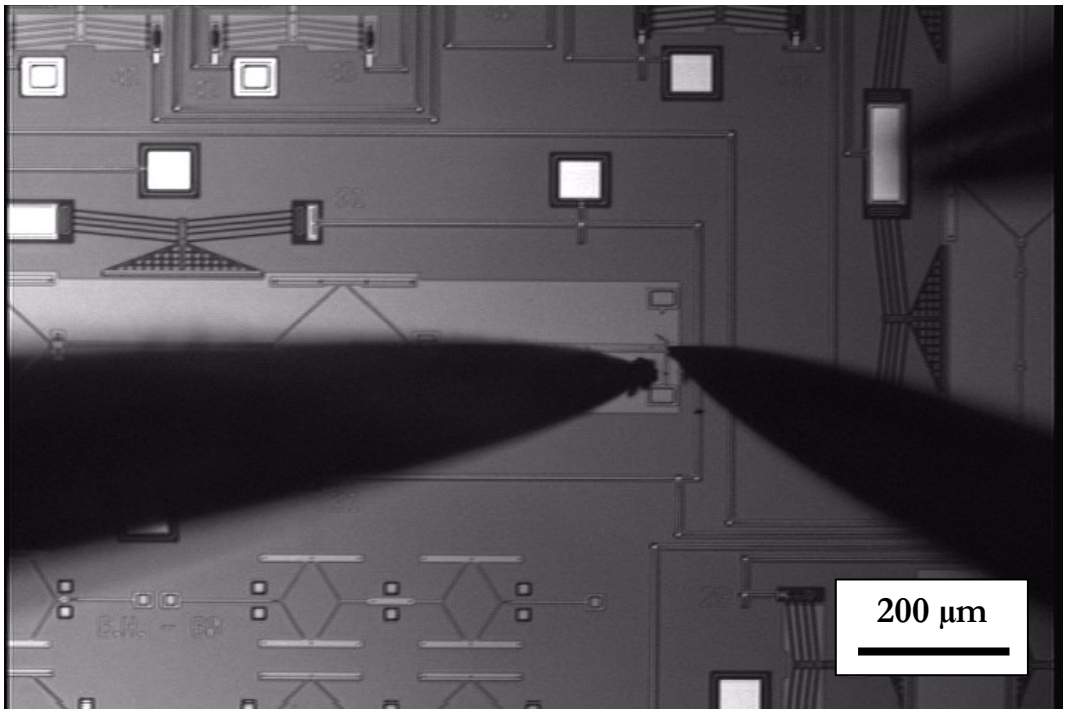

Figure 5.1.6 - Breaking Second Right Hand Tether

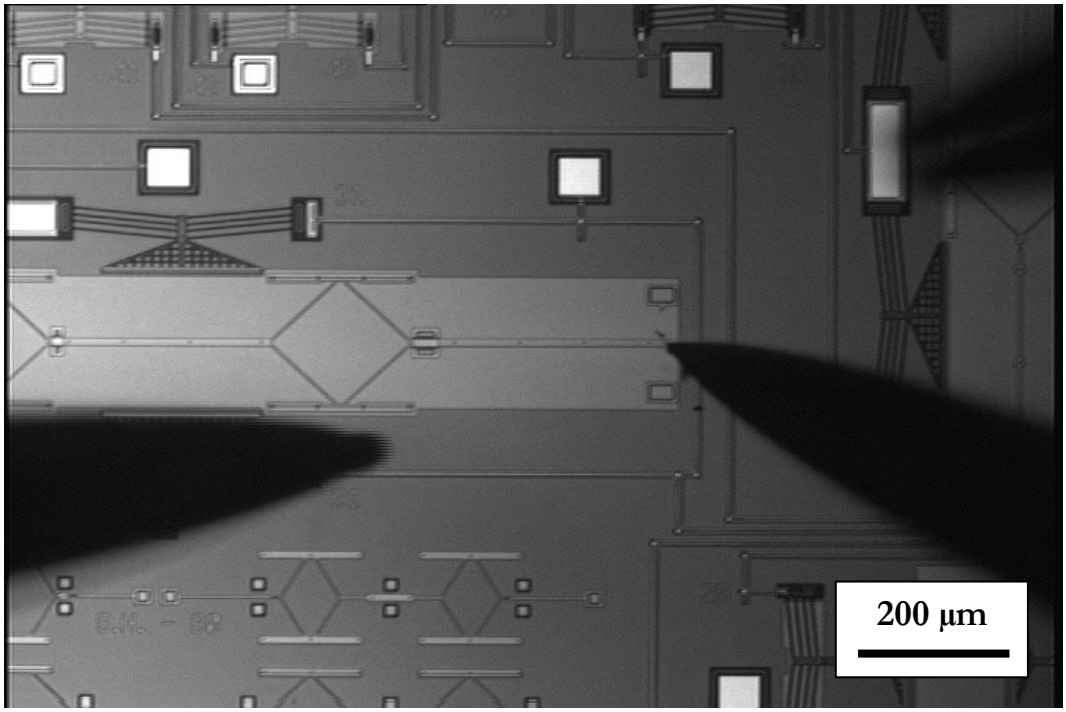

Figure 5.1.7 - Right Hand Tethers Fully Broken

Second, the larger 'T-shaped' tether located on the left land side of the earthworm shuttle was broken; an image of the tether before it was removed can be found in Figure 5.1.8. To prevent the shuttle from moving while the tether was broken, two probes were lowered beside the shuttle's diamond (one on each side). These two stabilizing probes can be seen in Figure 5.1.9, where they come from the right. Once the shuttle was held in place, a third probe, which entered from the left, was used to snap the tether off. This three-probe approach can be seen in Figure 5.1.10. Sometimes when this tether was broken, a small piece of it remained, as seen in Figure 5.1.11. In this case, one of the three probes was used to remove the remaining piece. Figure 5.1.12 shows an image of the shuttle once the tether on its left hand end was removed.

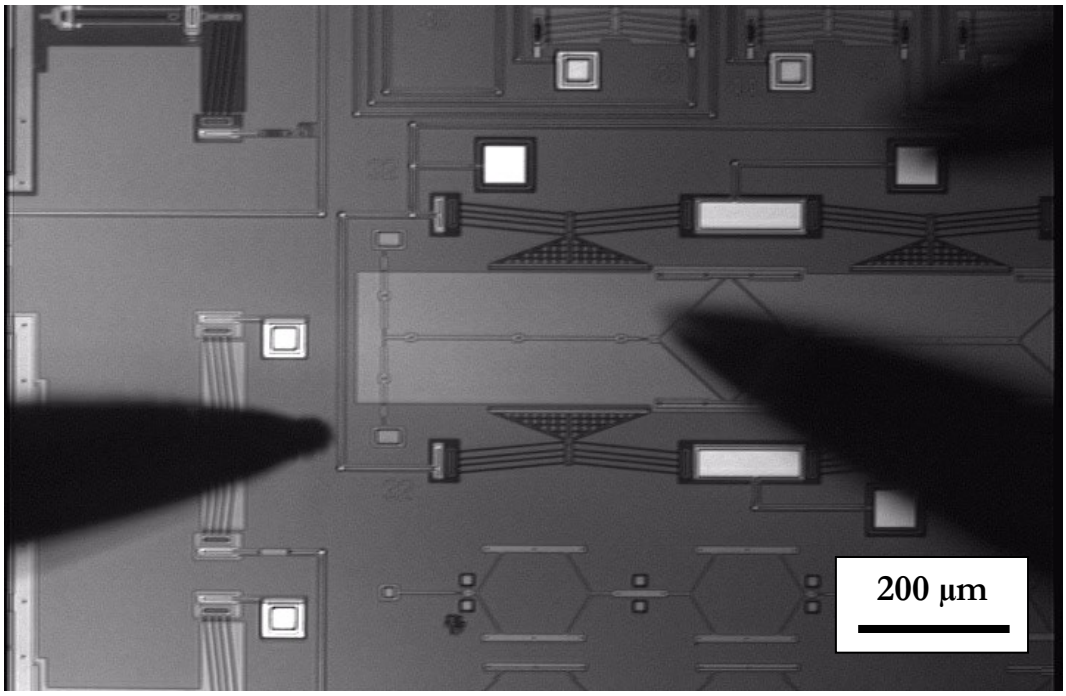

Figure 5.1.8 - Left Hand Tether Before Removal

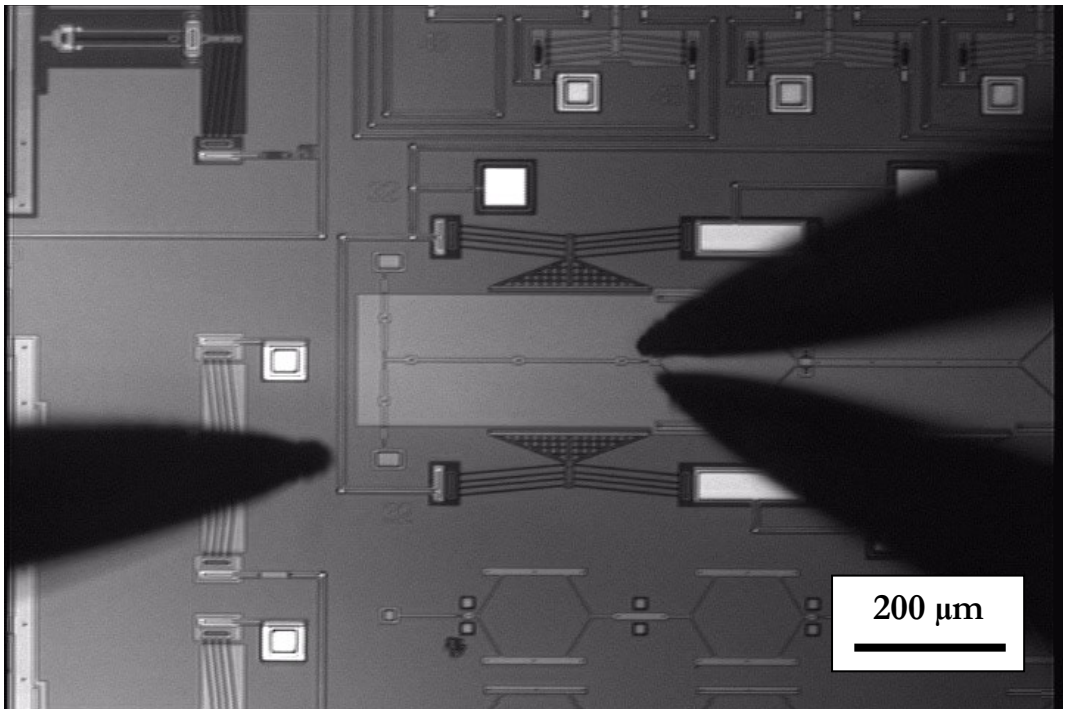

Figure 5.1.9 - Probes Used to Hold Shuttle in Place for Tether Breaking

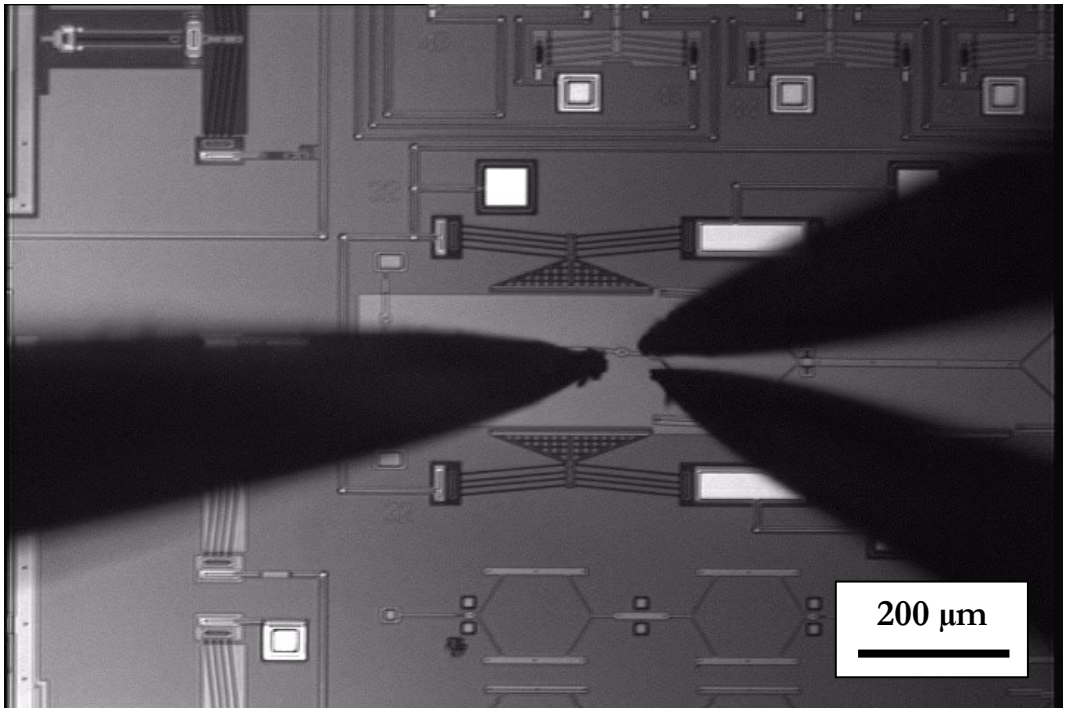

Figure 5.1.10 - Breaking Left Hand Tether

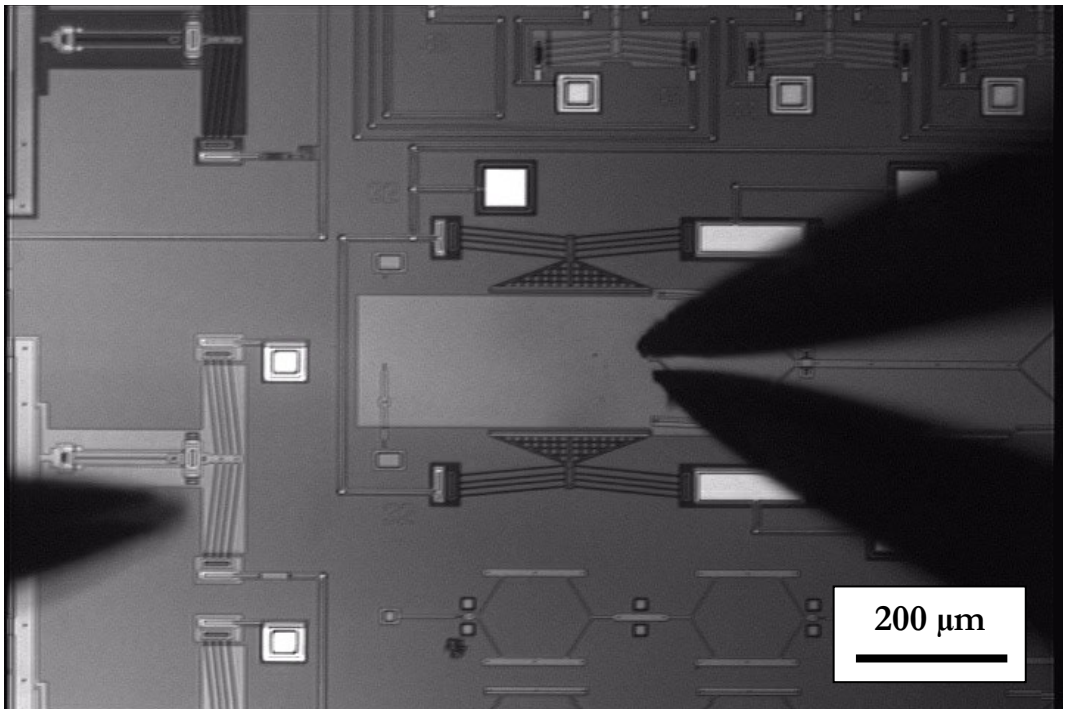

Figure 5.1.11 - Small Piece of Tether Remaining

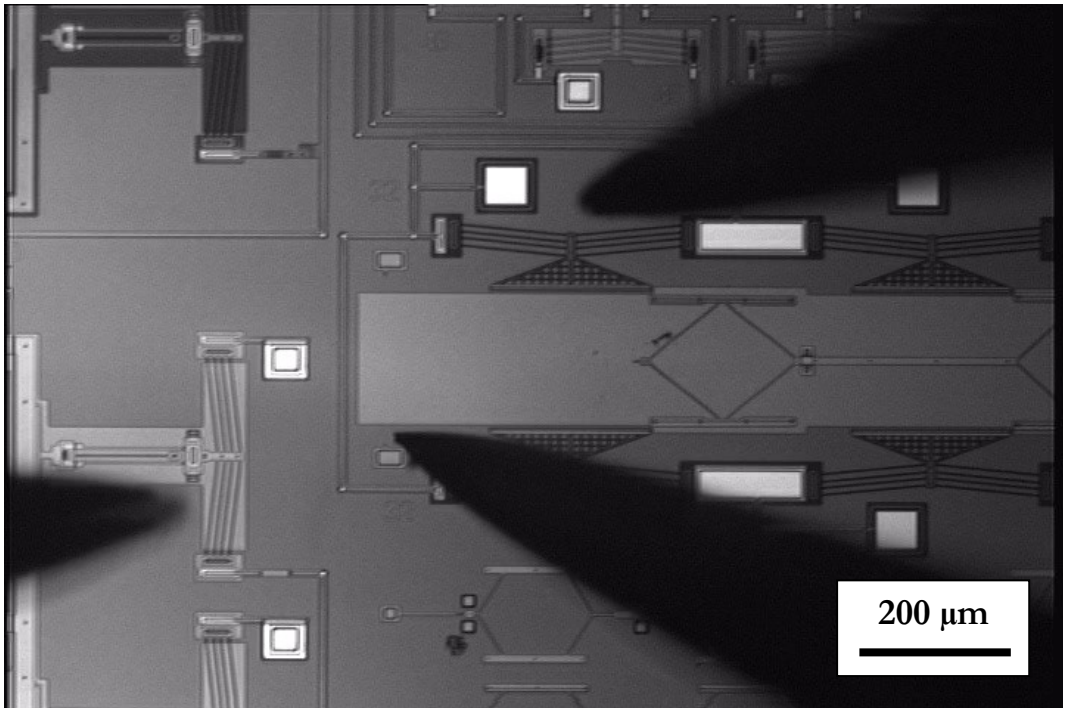

Figure 5.1.12 - Left Hand Tether Removed

Finally, the shuttle was moved laterally into its final testing position where it was centered between the pushers. This was achieved by using one probe to push the far right hand side of the shuttle towards the left. Figure 5.1.13 shows an image of the shuttle before it was moved, Figure 5.1.14 shows an image of the shuttle while it is being moved to its final position, and Figure 5.1.15 shows an image of the shuttle after it has been moved to its final position. Once the shuttle is centered between the pushers, the crawler is fully assembled and ready for testing.

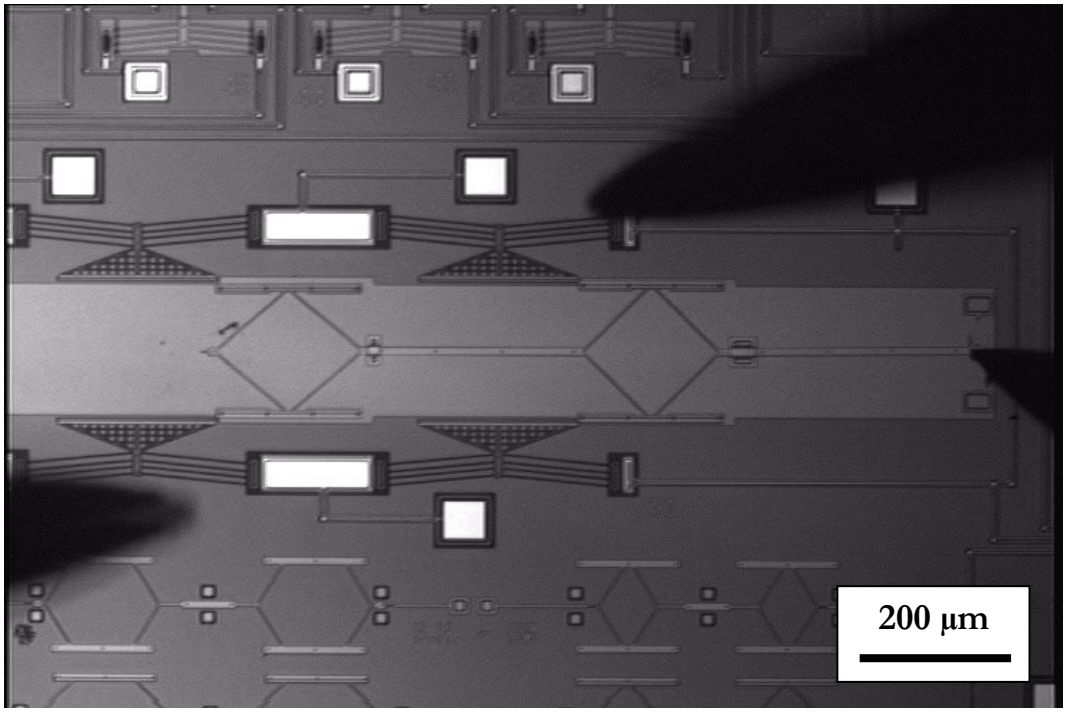

Figure 5.1.13 - Preparing to Slide the Shuttle to Its Final Testing Position

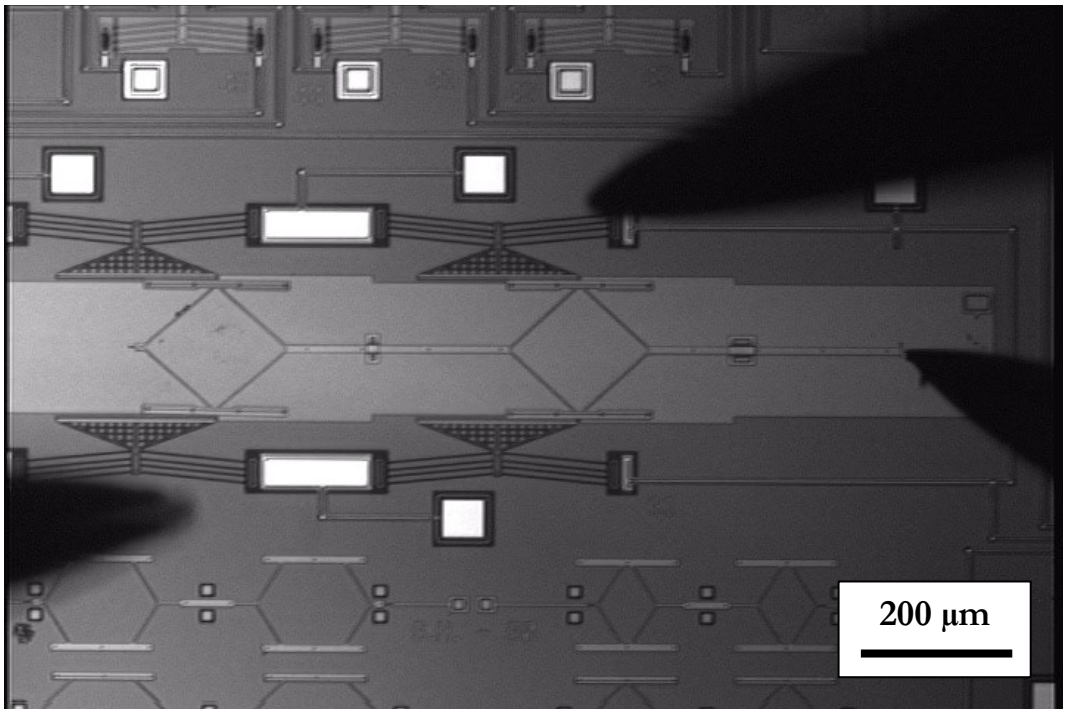

Figure 5.1.14 - Sliding the Shuttle to Its Final Testing Position

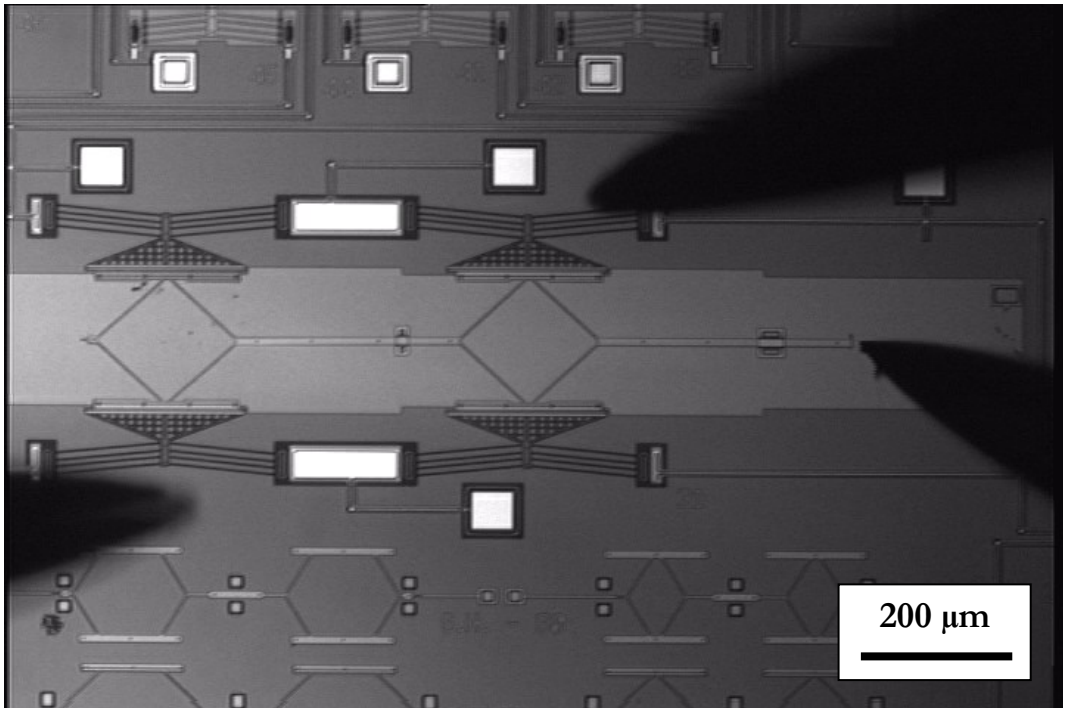

Figure 5.1.15 - The Shuttle in Its Final Testing Position

5.2 Motion Testing

A flowchart of the experimental motion testing set-up can be found in Figure 5.2.1. The experimental hardware, software, and procedures will be discussed in more detail in the following sections of this chapter.

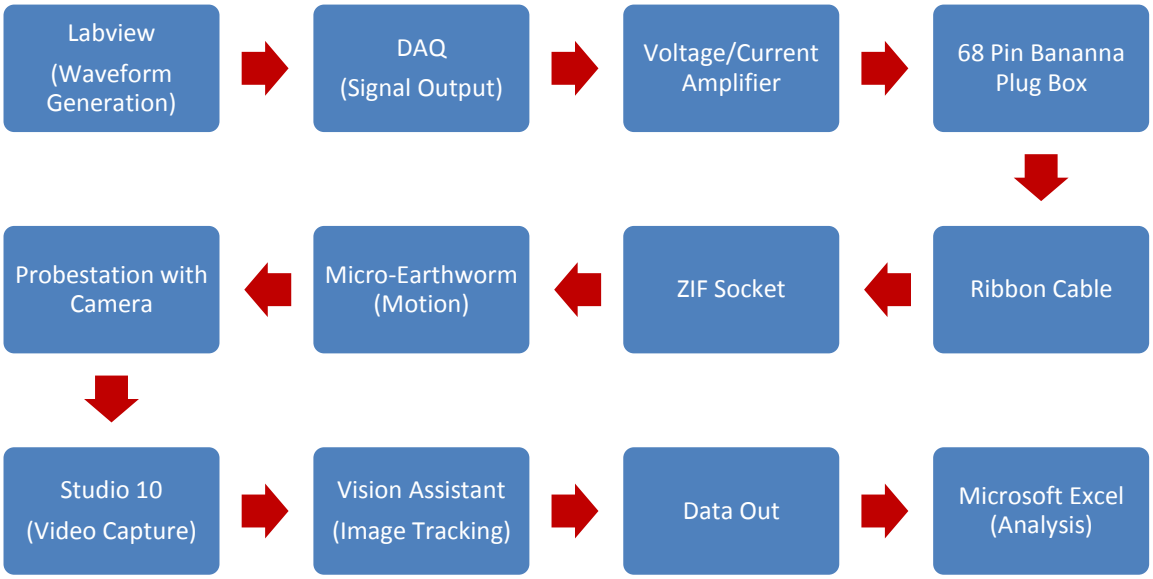

Figure 5.2.1 - Micro-Earthworm Motion Testing Flowchart

5.2.1 Hardware

The software used to operate the micro-scale earthworm crawler, which will be discussed in Section 5.2.2, outputted a low current (mA) signal through a National Instruments PCI-MIO-16E Data Acquisition Card (DAQ); this signal had a maximum voltage of 10 V. Due to the low power output of the DAQ, a current and voltage amplifier, with a voltage gain of 2x, was used to ensure that sufficient power (~50-100 mW) was

available for the operation of the micro-scale earthworm's chevron actuators. The MEMS earthworm crawler was held in a ZIF socket mounted on a Wentworth™ Probestation Model 901 microscope, which was wired to via a pair of ribbon cables to a 68PGA connection box. This box, as shown in Figure 5.2.2, had 68 numbered female banana plug connectors around its perimeter (one corresponding with each pin on the chip); it also contained a momentary switch and two polarity inverter switches in its center, which were not used for testing. The 68PGA connection box was used to connect both 'Signal 1', and 'Signal 2 (as described in Section 4.2) from the voltage/current amplifier, while the ground connections for the earthworm were made using two Wentworth™ probes (Model PRO195RH/PRO195LH), with 0.30 mm dia X 50 mm long stainless steel J-type acupuncture needles.

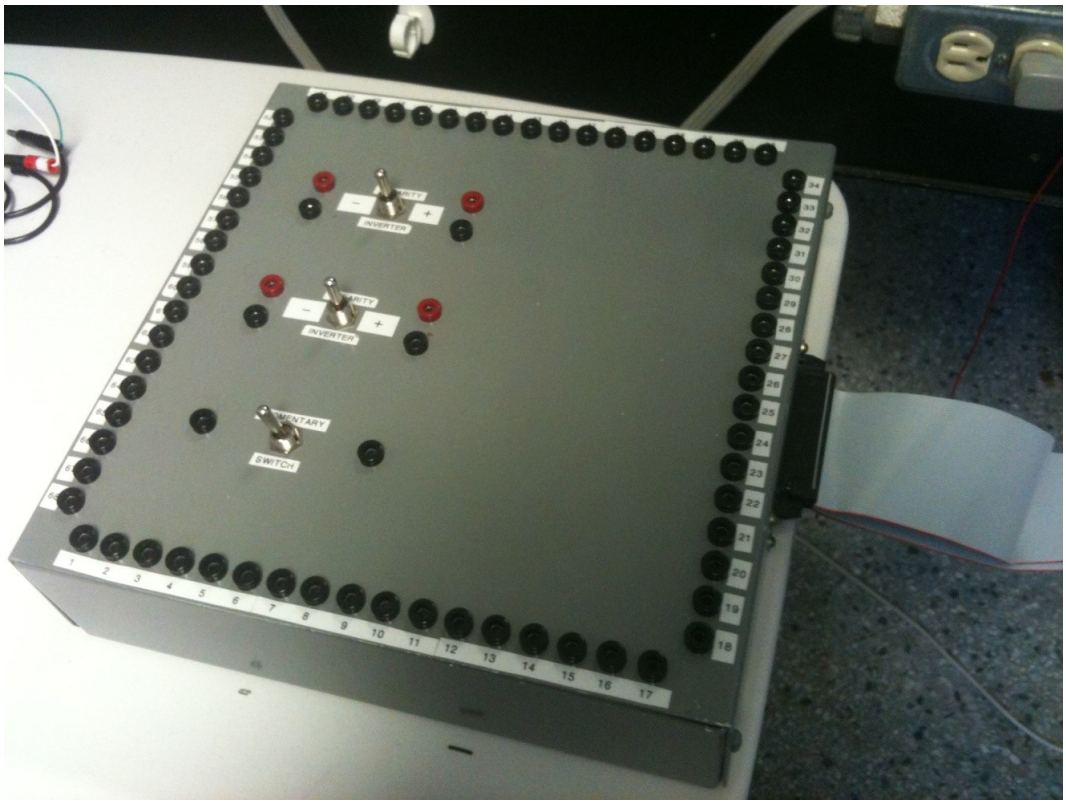

Figure 5.2.2 - 68PGA Electrical Connection Box (30 x 30 cm)

Video was taken using a Sony™ Model #XC-ST70 768x494 pixel, 30 fps, B&W CCD camera connected to the Wentworth™ Probestation microscope. This camera was connected to the computer via a Pinnacle™ 640x480 pixel video capture card.

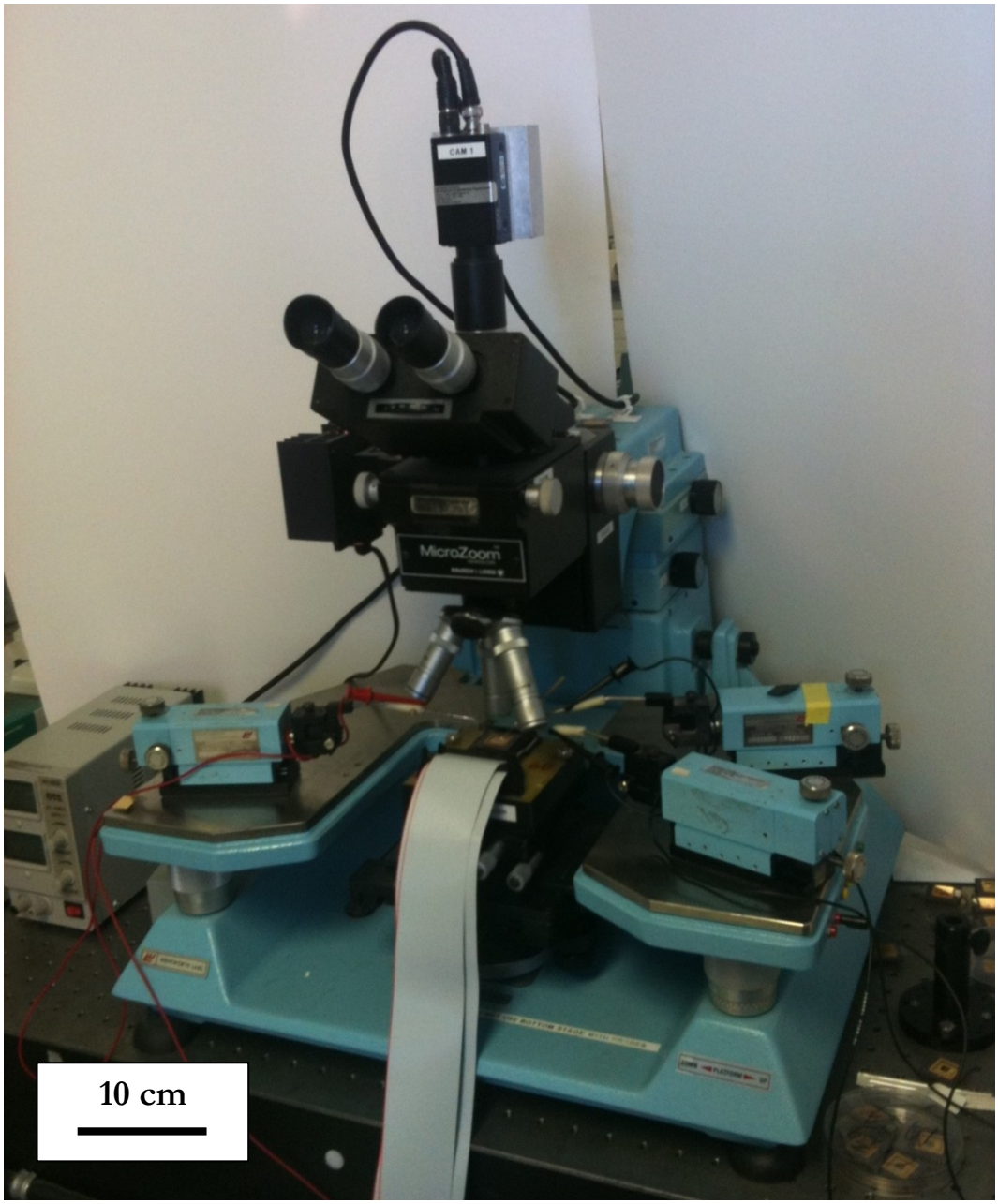

Figure 5.2.3 - MEMS Earthworm Motion Testing Experimental Set-Up

5.2.2 Software

Control of the micro-scale earthworm crawler was achieved via a customized National Instruments™ Labview Virtual Instrument (VI), a screenshot of which can be seen in Figure 5.2.4. The developed VI was created from a modified version of the software used to drive the macro-scale crawler, as discussed in Section 3.2.2; it allowed the user to specify the voltage and waveform provided to each actuator pair, as well as control the relative phase between the outputs. The waveforms consisted of ~square waves with a 50% duty cycle; these waveforms were not exact square waves, as the rise and drop had a slight ramp to them: taking 4% of the total cycle to rise and 4% to fall. This was done so that the changes in voltage were not too abrupt; while the earthworms could also be operated with pure square waves, the ramps improve repeatability.

It should be noted that the voltage settings in the Labview VI accounted for the voltage gain that resulted from the use of the voltage/current amplifier discussed in Section 5.2.1; this means that a Labview setting of 7 V would output 3.5 V from the DAQ, resulting in the desired 7 V after the voltage/current amplifier. For all tests, synchronized waveforms were sent to the right and left chevrons 90 degrees out of phase. The program allowed the user to specify the number of steps (bursts) that would be fed to the earthworm crawler, which allowed for greater control and accuracy of the experiment; the importance of these bursts will be discussed at a later time. Directional control of the crawler was accomplished by a 'direction switch' on the Labview VI, which would change the signal phase differences from +90° to -90°.

The video taken during the experiments was recorded using Pinnacle Studio 10 with an .avi file extension. This file was then imported into National Instruments™ Vision Assistant,

where the video's frames were separated into individual images. An image tracking script was then run on each image (frame) of the video. This script first converted the images to 8-bit greyscale; it then tracked a specified region of interest (ROI) in each frame and calculated x and y pixel displacements of the i^{th} frame ROI relative to the first frame's ROI. The pixel distances were converted to μm using a scale factor, and this data was outputted in the form of a text file. The output file from Vision Assistant was then opened using Microsoft Excel, where the data was analyzed. For displacement measurements, the above system measured position to sub-pixel accuracy and provided a measurement error of less than half a μm.

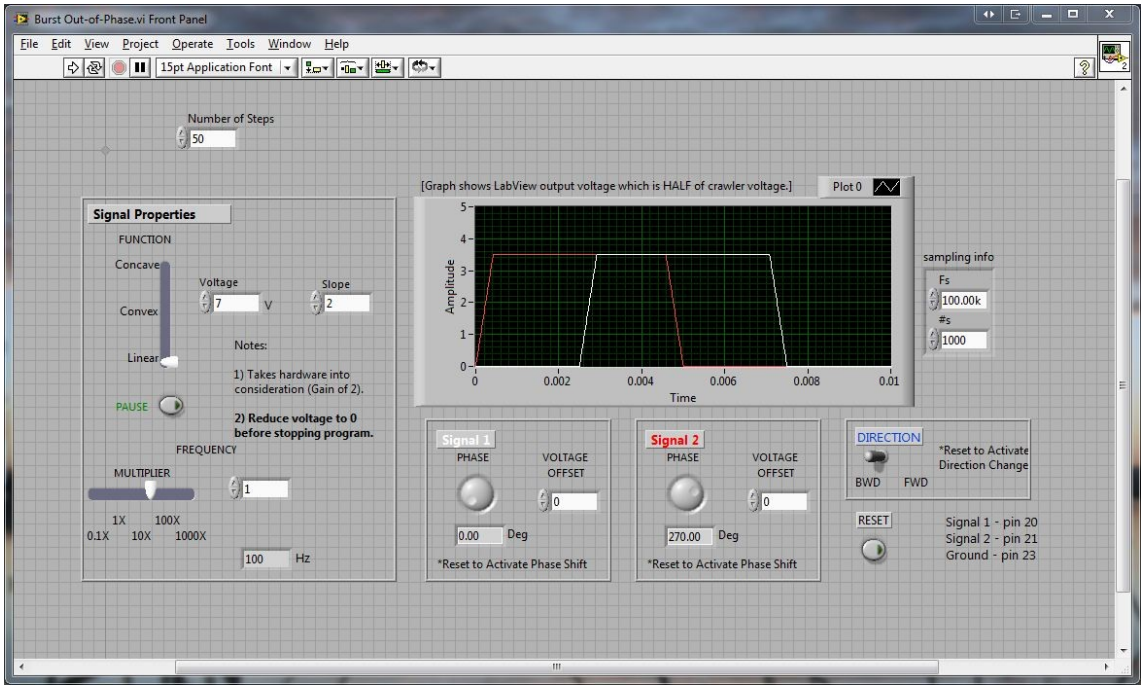

Figure 5.2.4 - Screenshot of Micro-Earthworm Motion Testing Labview VI

5.2.3 Procedure

Following is the procedure that was used for all micro-scale earthworm crawler motion testing (varying either voltage, or frequency).

First, the chip was assembled and electrically connected using the processes described in Section 5.1 and Section 5.2.1. Once the chip was in place and electrically connected, all Labview inputs for the test being run were correctly set. The video capture was then started, and the Labview VI was set to 'run'. After a set number of steps in one direction (generally 50) were completed, the direction was changed and the VI was run again. This direction change was repeated until ten or more runs in each direction were recorded. Upon completion of the experiment, video capture was ended; the video file was then saved with a name that was descriptive of the test's settings. Once all videos were recorded and saved, each file was imported into Vision Assistant, where the image tracking script was run on each frame of the video. Once image tracking of all video files for an experiment were completed, they were individually opened using Excel where they were analyzed.

While there were generally few difficulties with motion testing of the micro-scale earthworm crawler, it would occasionally become stuck. This stiction was more prevalent on days with high humidity; the stuck shuttle could generally be freed using a probe, and the test restarted.

5.3 Force Testing

A flowchart of the experimental set-up can be found in Figure 5.3.1. The experimental hardware, software, and procedures will be discussed in more detail in the following sections of this chapter.

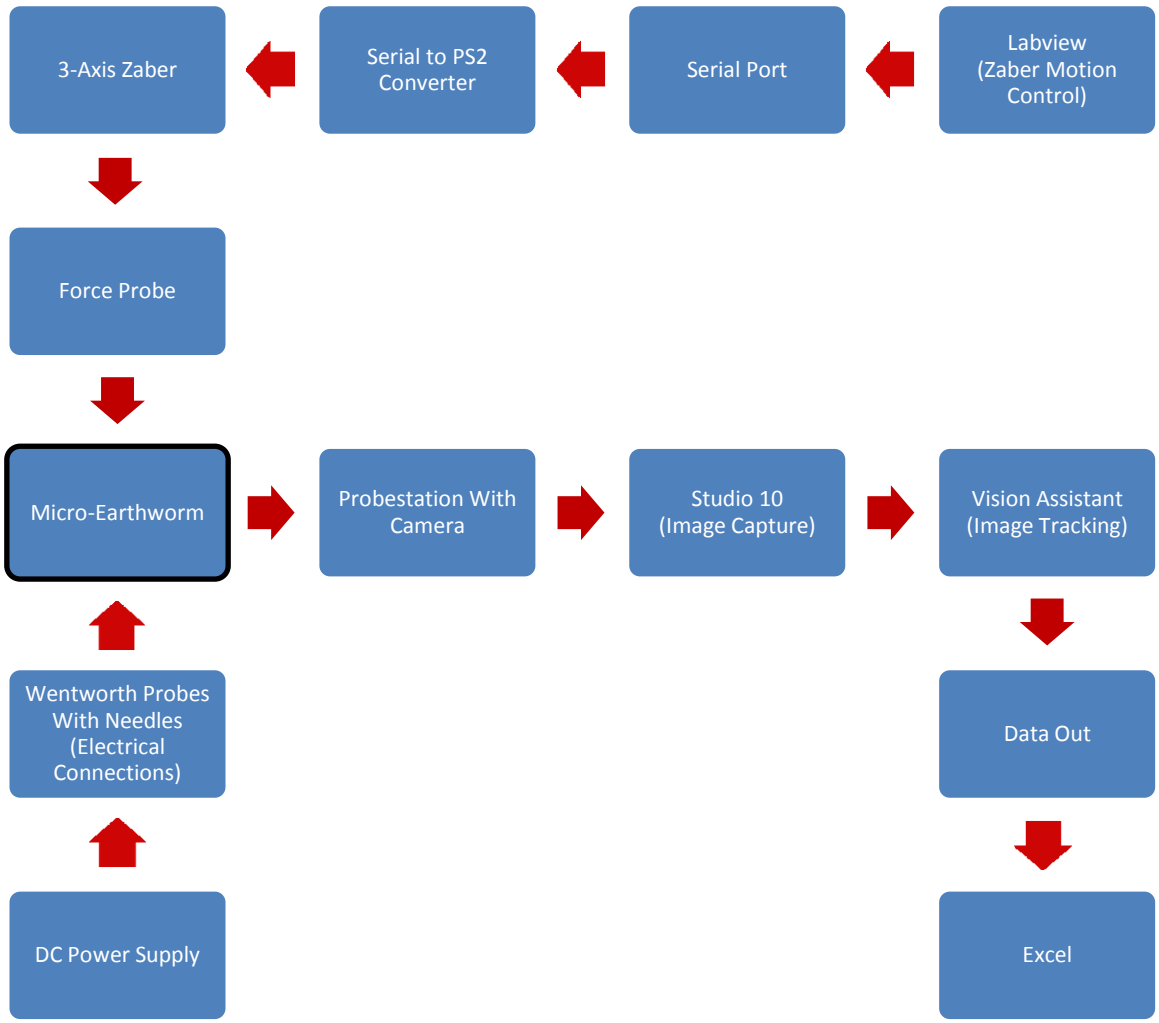

Figure 5.3.1 - Micro-Earthworm Force Testing Flowchart

5.3.1 Hardware

The MEMS earthworm crawler was held in a ZIF socket mounted on a Wentworth™ Probestation Model 901 microscope. The chip was held in the ZIF socket 90° counter-clockwise from its normal position, to allow ease of access for the force probe, which will be discussed in greater detail below. The rotation of the chip has no effect on the device's electrical connections, as the ZIF is used purely as a fixturing device during force testing.

Electrical connections for the earthworm crawler were made via three Wentworth™ probes (Model PRO195RH/PRO195LH), with 0.30 mm dia X 50 mm long stainless steel J-type acupuncture needles; with one probe for each ground (2 total), and one probe for a voltage supply for the pair of squeezing chevrons. For the purposes of force testing, only one opposed pair of chevrons were powered, since there are times during the earthworm's operation when there is only one set of pushers squeezing the shuttle.

The force probe, shown in Figure 5.3.2, consists of a rigid steel beam with a clamp on the end; held in this clamp is an acupuncture needle that is chosen to reasonably match the stiffness of the item being measured. For the purposes of the micro-earthworm force testing, a 0.25 mm dia X 50 mm long stainless steel J-type acupuncture needle was used, with 20.38 mm of the needle's length extending freely past the clamp. Since the needle's diameter, length, and material are known, its stiffness (k) can be calculated using the following equation:

$$k = \frac{3EI}{L^3}$$

Equation 5.3.1

Where: E is the modulus of elasticity (Surgical Stainless Steel = 190GPa), I is the needles moment of inertia in m^4 ($I = \frac{\pi D^4}{64}$, where D = needle diameter, in m), and L is the free length of the needle (in m). It should be noted that, although the needle's diameter was specified as 0.25 mm, its measured diameter was actually 0.240 mm. From this equation, given the needle's geometry, its stiffness was calculated to be 10.97 μN/μm.

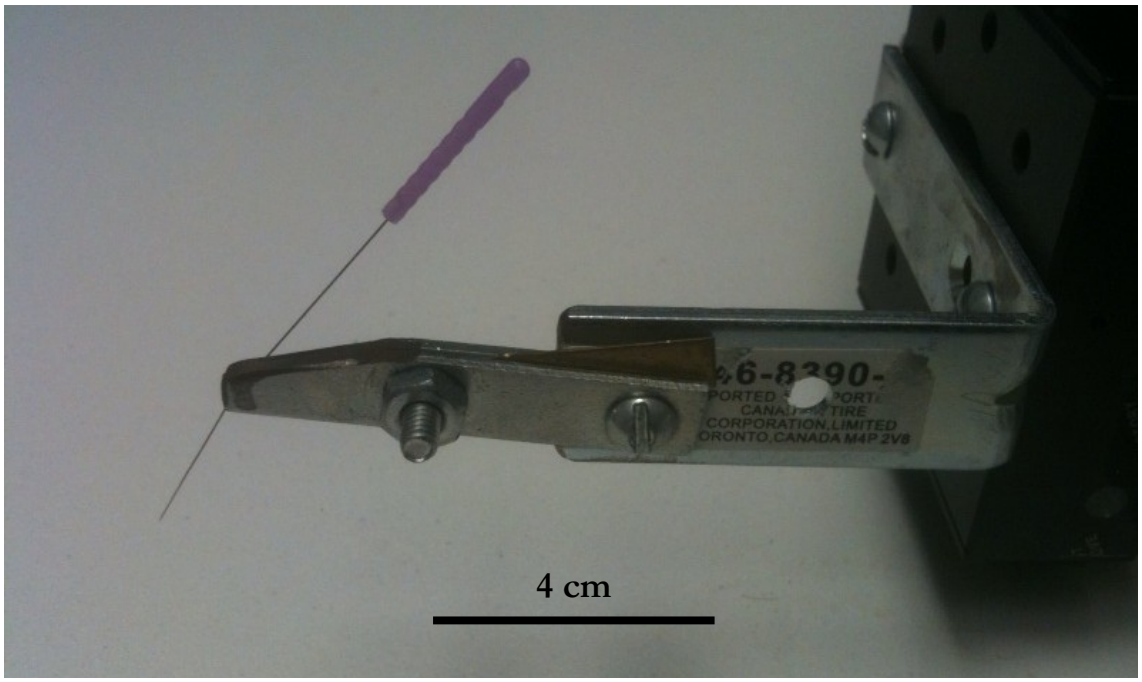

Figure 5.3.2 - Force Probe

The force probe was mounted to a 3-axis base, which could be positioned using computer-controlled Zabers (microstepping miniature linear actuators); this base can be seen in Figure 5.3.3, and allowed small, controllable, displacements of the force probe to be made. The three Zabers were connected in series to the computer's serial port via a serial-to-PS2 adapter, and a PS2 cable. The force probe allows measurements of device forces using the

needle's stiffness (k) and displacement (Δ) to calculate the force (F) through the following relationship:

$$F = k\Delta = k_{needle}(\Delta_{needle} - \Delta_{shuttle})$$

Equation 5.3.2

In the case of the micro-scale earthworm crawler, the maximum possible force that can be exerted is at the point of the shuttle slipping from between the clamped pushers (the device's stall force).

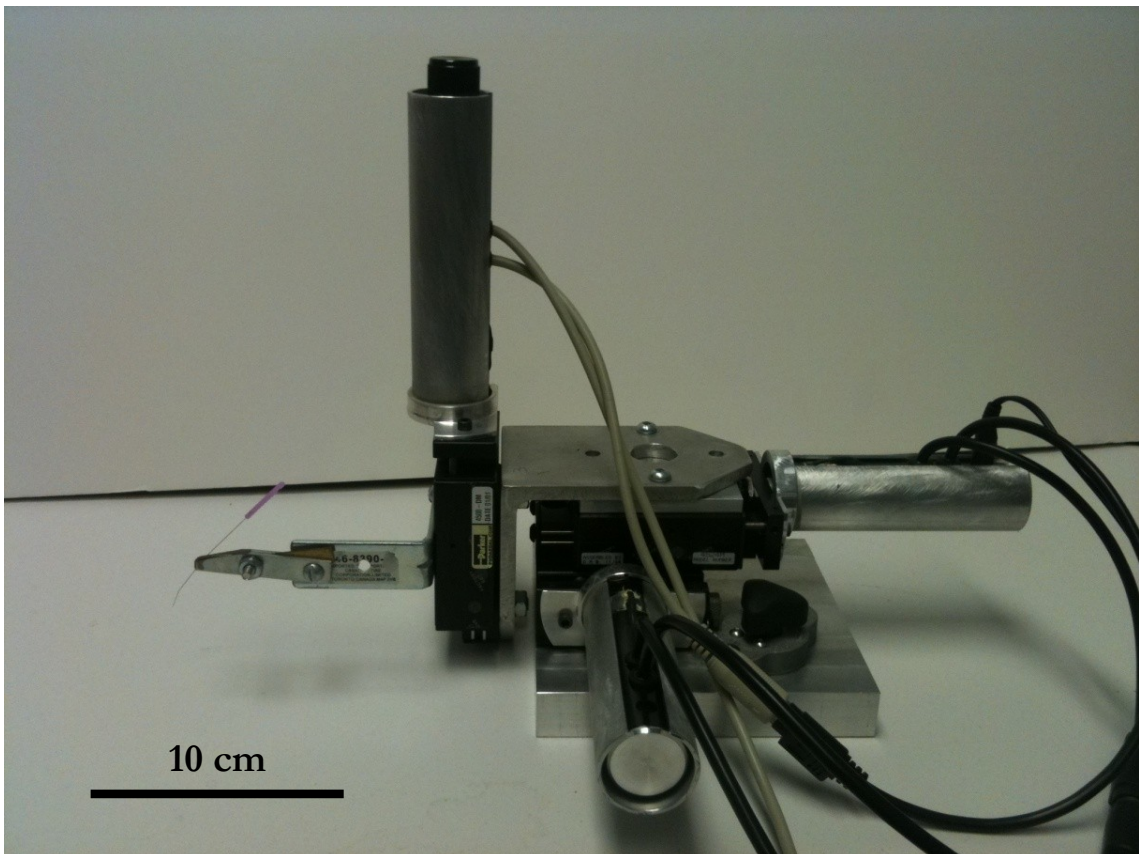

Figure 5.3.3 - 3-Axis Zaber With Force Probe

Video was taken using a Sony™ Model #XC-ST70 768x494 pixel, 30 fps, B&W CCD camera connected to the Wentworth™ Probestation microscope. This camera was connected to the computer via a Pinnacle™ 640x480 pixel video capture card. An image of the experimental set-up used for force testing, showing the three probes used for electrical connection as well as the force probe, can be seen in Figure 5.3.4.

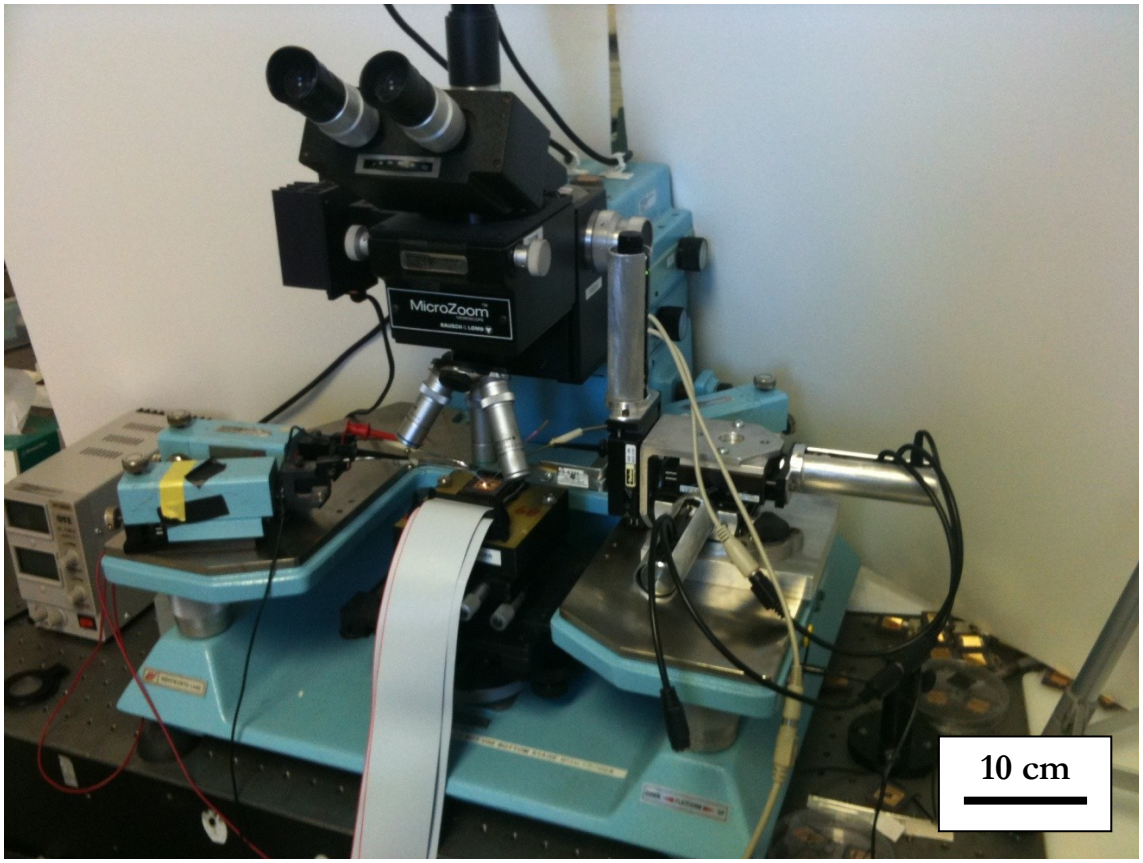

Figure 5.3.4 - MEMS Earthworm Force Testing Experimental Set-Up

5.3.2 Software

Control of the Zaber was achieved via a customized National Instruments™ Labview Virtual Instrument (VI), a screenshot of which can be seen in Figure 5.3.5. The developed VI allowed the user to send commands to each of the three Zabers used individually, or all at once. Its main purpose was to allow independent control over the displacement of each of each axis on the force probe's base.

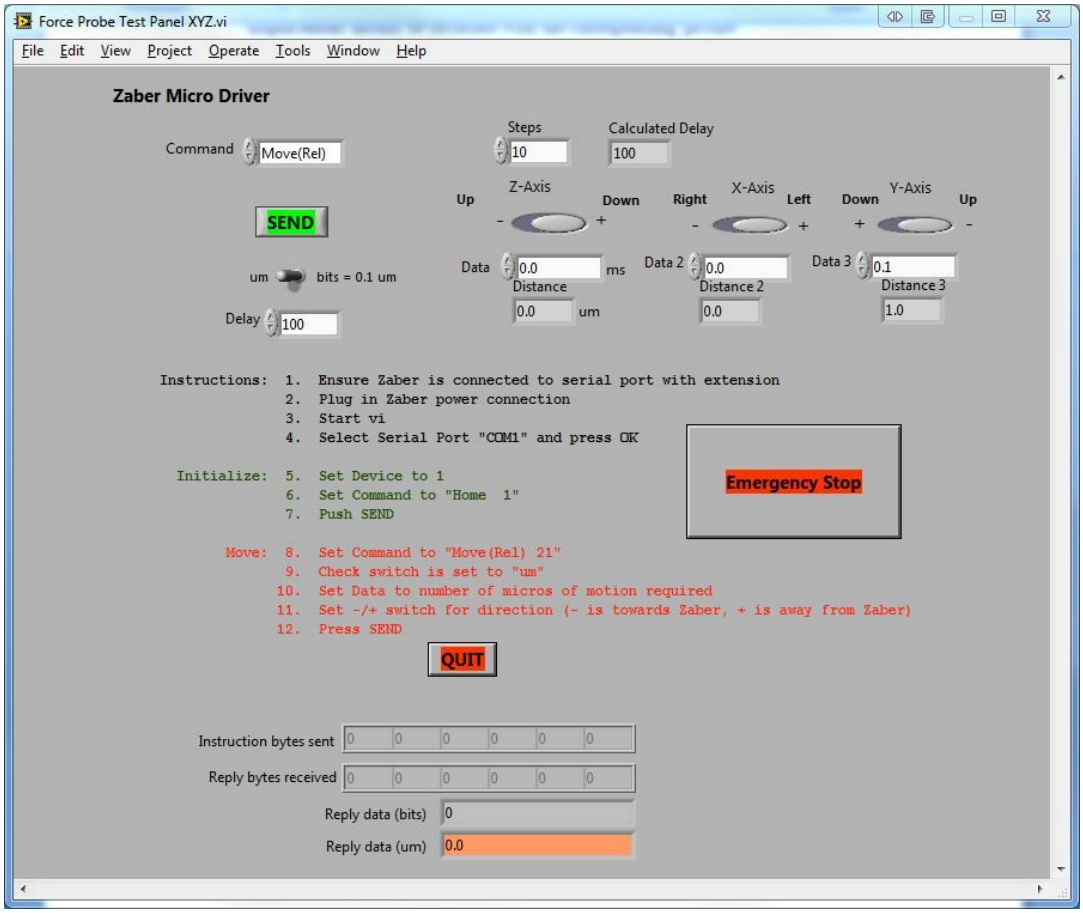

Figure 5.3.5 – Snapshot of Force Testing Labview VI

Images taken during the experiments were recorded using Pinnacle Studio 10 with an .jpeg file extension. These images were then imported into National Instruments™ Vision Assistant, where an image tracking script was run on each image. This script first converted the images to 8-bit greyscale; it then tracked a specified region of interest (ROI) in each image and calculated x and y pixel displacements of the i^{th} image ROI relative to the first image's ROI. The pixel distances were converted to μm using a scale factor, and this data was outputted in the form of a text file. The output file from Vision Assistant was then opened using Microsoft Excel, where the data was analyzed. For displacement measurements, the above system measured position to sub-pixel accuracy and provided a measurement error of less than half a μm.

5.3.3 Procedure

Following is the procedure that was used for all micro-scale earthworm crawler force testing. Before the force experiments began, the needle used on the force probe was measured using a micrometer and digital callipers (both diameter and length).

First, the chip was assembled using the processes described in Section 5.1. One opposing set of chevrons were electrically connected to a DC power supply via three probes, as described in Section 5.3.1. The Zabers were then connected to the computer, and powered via an AC adapter; once the Zabers were fully connected, the Labview VI was started and all Zabers were 'homed' to their fully-retracted state.

Second, the DC power supply that powered the chevrons was switched on, and the force probe was moved using the Labview VI to its correct position for force testing. The correct needle height, as shown in Figure 5.3.6, is just above the chip's surface; this allows the

greatest amount of contact between the needle and the device being tested without having the needle dragging across the chip. The correct needle location, as shown in Figure 5.3.7, is just touching the end of the shuttle when the chevrons are in their powered state, with the needle being oriented at a ~90° angle to the shuttle.

Third, the shuttle was tested; to do this, a photo was then taken using Studio 10 and the Zaber was moved slowly in the direction of the shuttle (vertically upwards in Figure 5.3.7) by a set distance (generally 10 steps at 0.1 μm per step, resulting in 1.0 μm per move). At this point, another photo was taken and the shuttle was moved again by the same distance. This move and photograph procedure was repeated until the shuttle visibly slipped from its original starting position between the clamped set of pushers, at which point a final photo was taken.

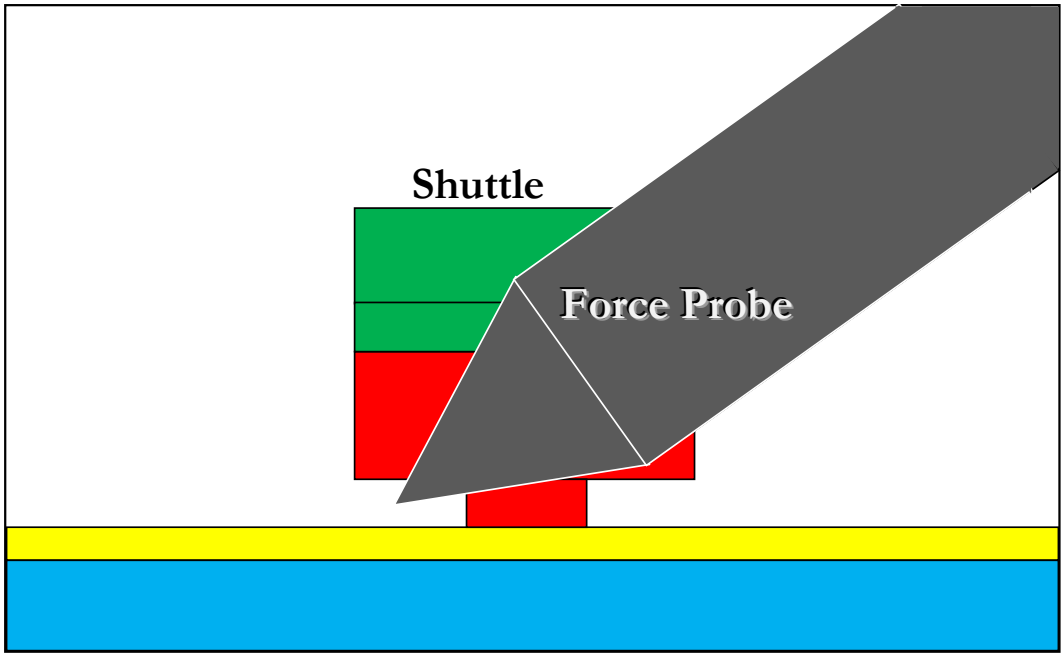

Figure 5.3.6 - Correct Force Probe Height (Not To Scale)

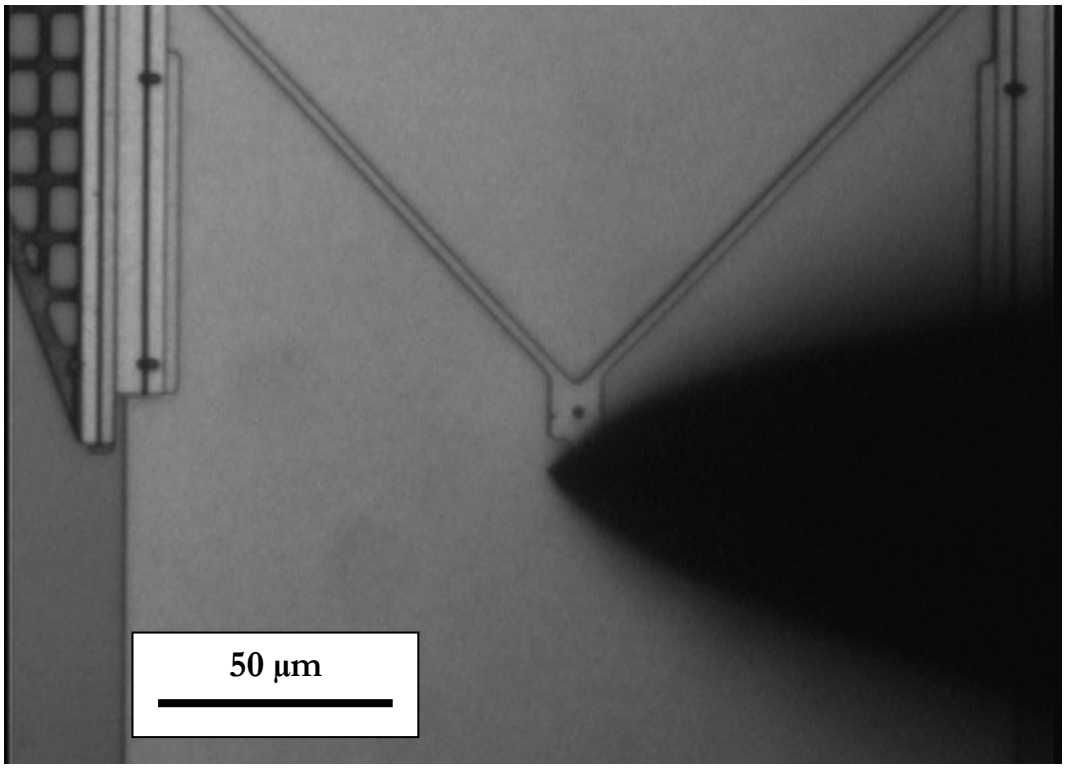

Figure 5.3.7 - Correct Force Probe Location for Shuttle Testing

All photographs for a set voltage and trial were opened in Vision Assistant, where the image tracking script was run on each captured image. The output file from Vision Assistant was then opened using Excel where it was analyzed.

Force testing proved to be much more difficult than motion testing due to the added complexity of the additional load applied by the force probe. Frequently, the shuttle would stick, resulting in an excessive force reading. This is likely caused due to dirt or debris on the chip, and high testing humidity. Another common problem, due to the overhead view of the camera, was damage to the chip's surface from lowering the force probe to its final testing position, or the needle slipping over the shuttle due to the needle being set to highly. Needle slippage laterally during force testing was found to be problematic due to the small contact

patch in the area of the tether connection on the end of the shuttle. Force testing on future devices may be simplified by the addition of a wider and taller structure on the end of the shuttle created using both Poly1 and Poly2, giving more of an area for the force probe to contact during testing. This change would allow a smaller chance for the force probe's needle to slip from the device in either the lateral or vertical direction.

Chapter 6: Results

The following chapter includes testing results for tracking individual segments of the micro-scale earthworm crawler, as well as proof of long-range back-and-forth motion. It covers the changes in shuttle velocity as a result of varying the shuttle's driving voltage and frequency, and also covers the testing of maximum shuttle output forces.

6.1 Earthworm Steps

For reference, Figure 6.1.1 shows a copy of the stages of micro-earthworm motion from Figure 2.1.1, which will be referred to throughout this section. Figure 6.1.2 shows the recorded shuttle motion in 3 steps using the experimental set-up and procedures from Section 5.2, with the crawler operating at a voltage of 9 V and a frequency of 0.1 Hz. The numbers 1-5 in the image refer to the stages of motion found in Figure 6.1.1; the points a,b,c,d referring to the shuttle locations in Figure 6.1.1. The displacement of the shuttle's front end is shown in green and corresponds to point *d* in Figure 6.1.1, while the displacement of the back end is shown in red and corresponds to point *a* in Figure 6.1.1. The motion of the stiff center section is shown in blue, and corresponds to segment *b -c* in Figure 6.1.1.

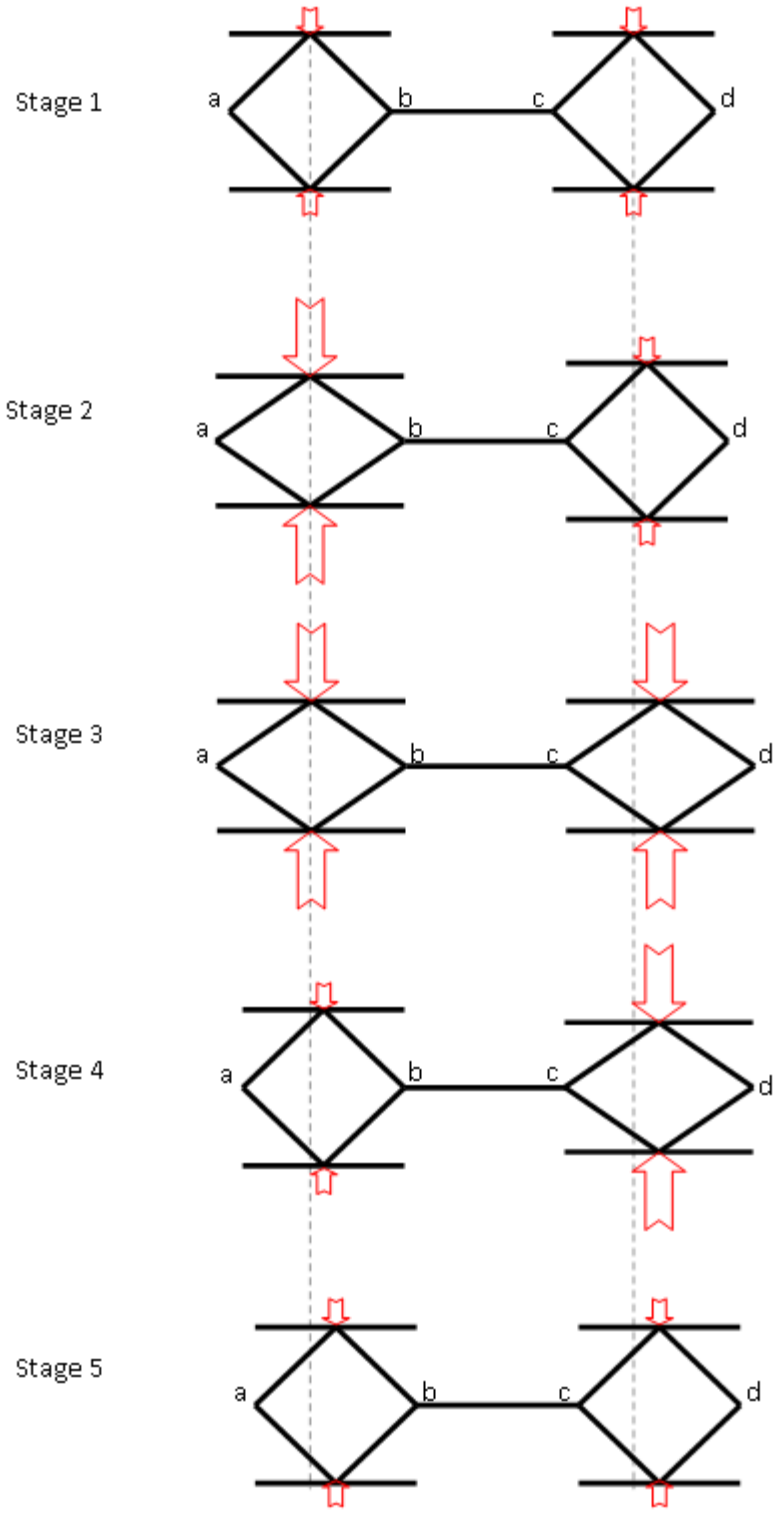

Figure 6.1.1 - Stages of Micro-Earthworm Motion

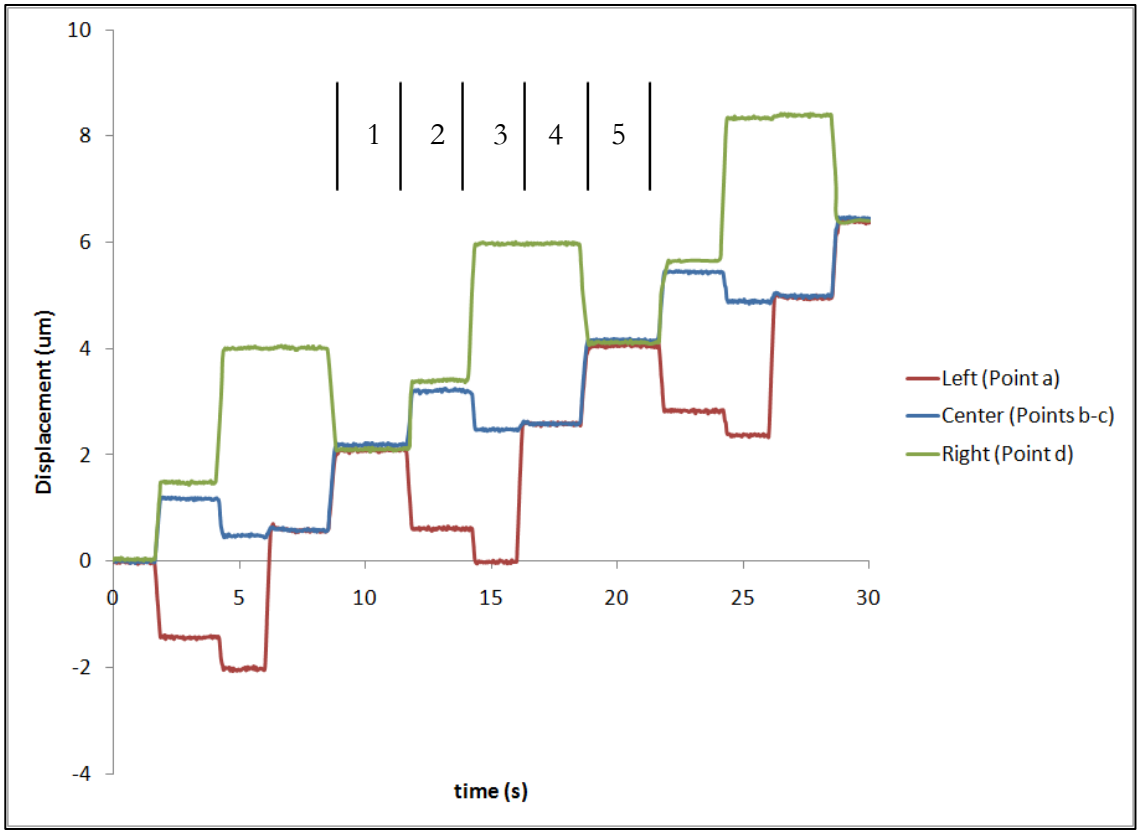

Figure 6.1.2 - Measured Step Displacements vs. Time

The 5 stages of shuttle motion, as shown in Figure 6.1.1, are identified by their numbers in Figure 6.1.2; the numbered stages begin at approximately 9 seconds and conclude at approximately 19 seconds. At ~12 seconds, Stage 2 begins as the left diamond is squeezed and both the center (blue = segment *b-c*) and right end (green = point *d*) are pushed forward while the left end (red = point *a*) is pushed back. At ~14 seconds, Stage 3 begins as the right diamond is also squeezed and the front end (green = point *d*) is pushed further forward while both the center (blue = segment *b-c*) and the far end (red = point *a*) slip slightly backwards. At ~16 seconds, Stage 4 begins as the left diamond is released and the far end (red = point *a*) is pulled forward. At ~18 seconds, Stage 5 begins as the right diamond is

released and the front end (green = point *d*) is pulled back while both the center (blue = segment *b-c*) and the far end (red = point *a*) are pulled forward. The locations of all points have now advanced the same amount, and this ends one complete step cycle. The average net step size for all three steps shown in the diagram is approximately 2 μm. When high-precision operation is desired, driving voltages can be lowered to yield very small steps; when the crawler was operated in the range of 4 V, a step size of ~0.3 μm was measured.

Figure 6.1.3 and Figure 6.1.4 show a much longer range of motion, with the shuttle switching direction every 50 cycles; for the test shown in these images, the crawler was operated using a voltage of 7 V and a frequency of 1.0 Hz. Figure 6.1.3 shows 50 steps forward (to the right) and 50 steps backward (to the left). The motion (measured over 100 steps) has a mean value of 1.91 μm per step, with a standard deviation of 0.23 μm/step. The motions in each direction are not exactly the same, with the right and left motions (each measured over 50 steps) having a mean value of -1.89 ± 0.20 and 1.94 ± 0.20 μm/step respectively. Possible causes of this ~3% difference in left/right velocities are slight differences in the actual fabricated left/right gaps between diamond and chevron pairs, or the left/right waveforms having slightly different voltages caused by different wiring resistance paths. Figure 6.1.4 shows 10 sets of back and forward motion, with the experiment totalling 1860 μm of distance traveled. The measured motion in this image shows some drift, with the shuttle ending at a position offset from its initial position by 22 μm after travelling a total of 1860 μm, or 1.2 % of the total distance travelled. This drift may, in fact, be caused by the above mentioned differences in left/right velocities.

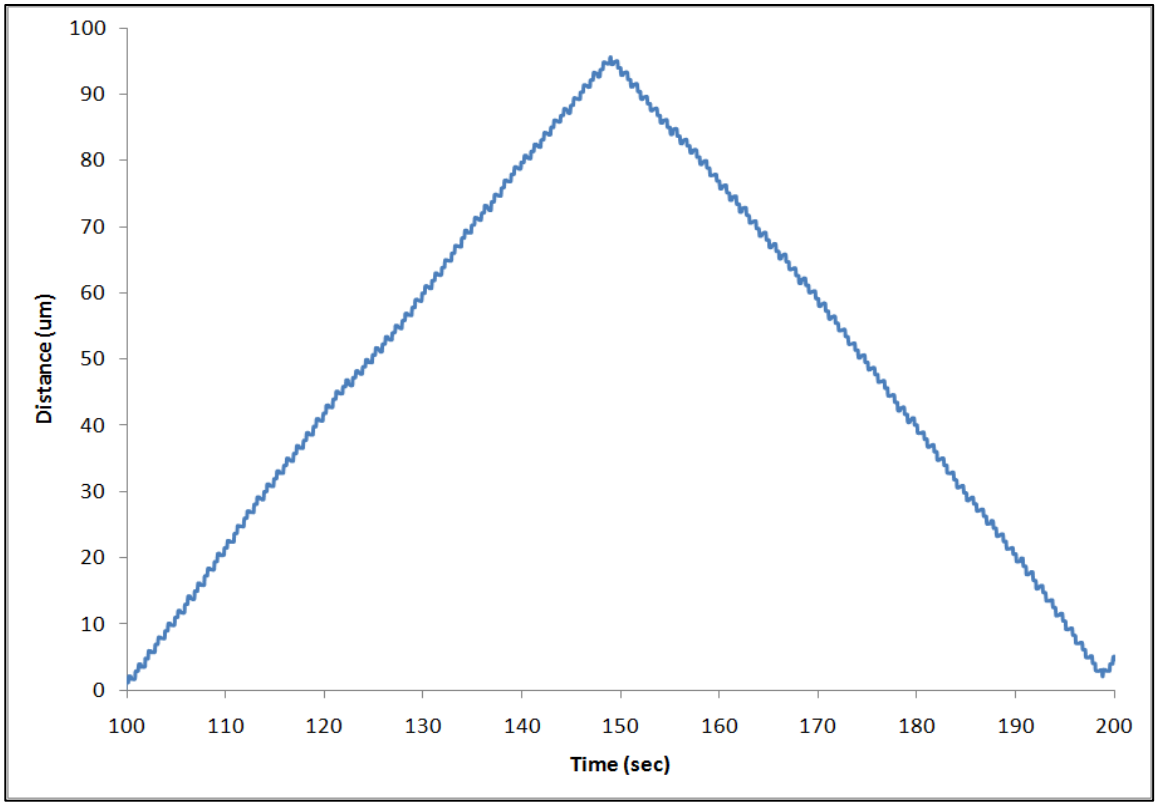

Figure 6.1.3 - Measured Motion of the Shuttle (50 Steps in Each Direction)

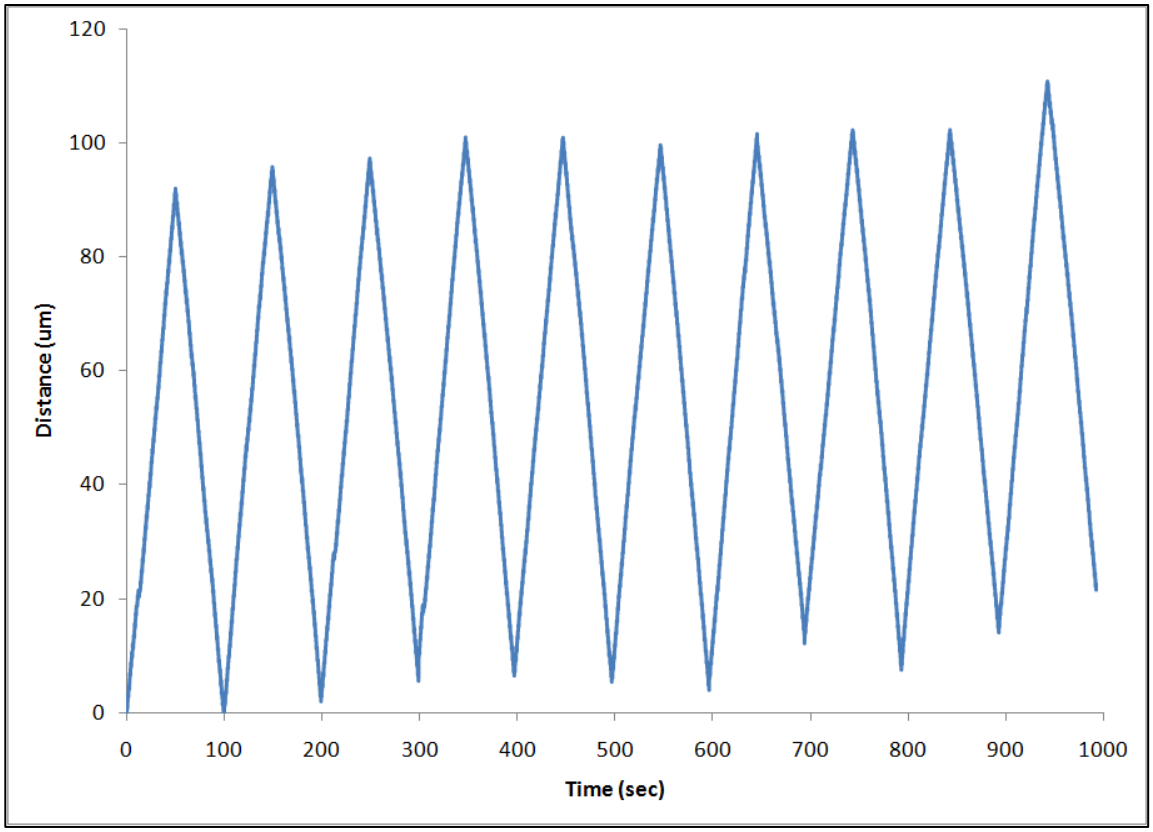

Figure 6.1.4 - Measured Long Range Motion of the Shuttle (With 1% Drift)

6.2 Shuttle Velocity vs. Driving Voltage

Before measuring how the velocity of the shuttle is affected by applied voltage, we will first examine the behaviour of the chevrons used with respect to applied voltage. Measurements of an unloaded chevron at 7 volts DC show that it produces 1.96 ± 0.16 μm of motion; a graph of unloaded chevron displacement vs. input voltage can be seen in Figure 6.2.1. In this figure, the chevron was loaded with 0 V (the chevron turned off), 4 V (the crawler's minimum operating voltage), 7 V (the crawler's standard operating voltage), and 9 V (the crawler's maximum operating voltage). At each voltage, five measurements were

taken; the figure shows the mean, as well as one standard deviation. As shown in the figure, the displacement of an unconstrained thermal actuator is proportional to the inputted electrical power or voltage squared. This relationship will be discussed further at a later point in this section.

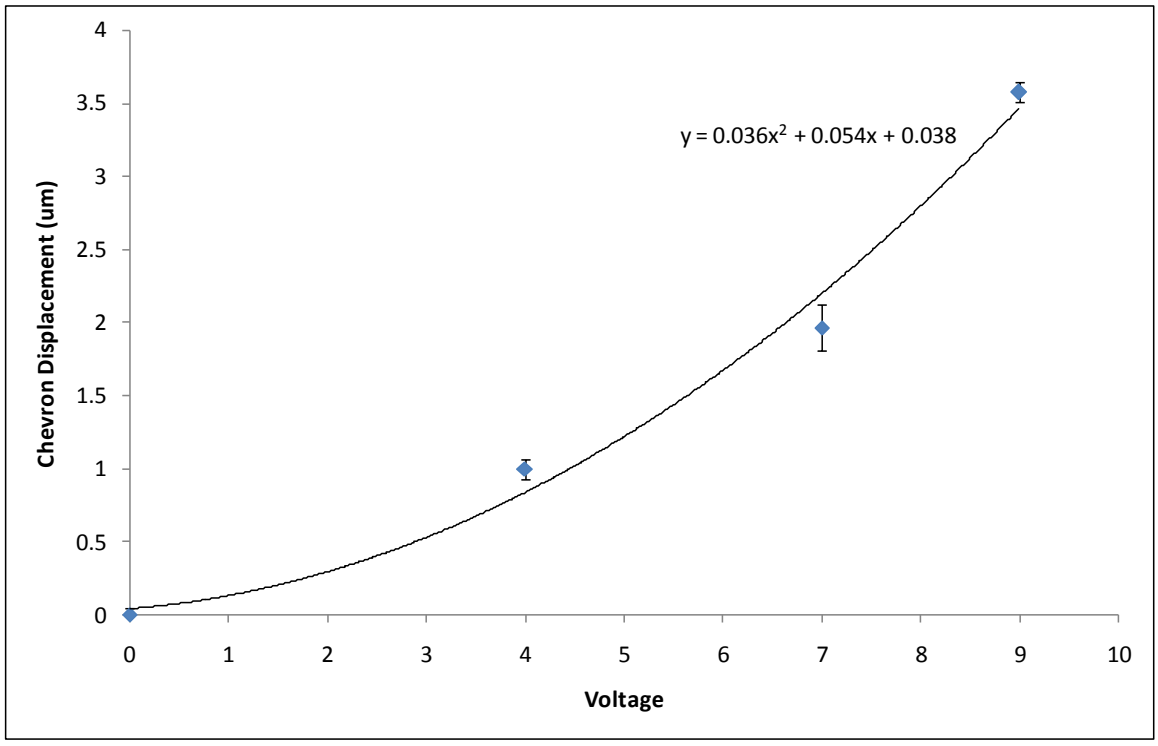

Figure 6.2.1 - Unloaded Chevron Displacement vs. Voltage ($R^2 = 0.99$)

For all shuttle velocity measurements, the shuttle was first assembled and aligned with the center of the chevrons (as described in Section 5.1). The device was then run forwards and backwards, 50 steps each way, a minimum of ten times (as described in Section 5.2.3).

Figure 6.2.2 shows the measured velocity as a function of input voltage at a fixed frequency (10 Hz). The average of left and right velocities is shown: a minimum of twelve separate measurements (minimum six in each direction) were made for each data point: the plots show the mean, as well as one standard deviation. A little over 3 volts are required to close the initial gap between the actuators and the shuttle and approximately 4 volts are required to overcome the initial friction and move the shuttle. The gap between the lattice pushers and the shuttle is 0.5 μm per side; this means that a pair of squeezing chevrons would ideally produce a transverse shuttle motion of l = (1.96 - 0.5) = 1.46 μm, resulting in a net step motion of 2*l = 2.92 μm. When tested at 7V and 10 Hz, the shuttle had a velocity of 19.1 μm/s; this resulted in a net step size of $\frac{19.1\ \mu m/s}{10\ Hz}$ = 1.91 ± 0.23 μm, which is approximately 66% of the ideal unloaded case. The reduction in motion is caused by the loading from shuttle: in operation the chevrons are loaded by contact forces produced by the elastically deforming diamond segments and by friction forces resisting sliding of the shuttle, with the friction forces being proportional to the deforming forces. As shown in Figure 6.2.1, the displacement of an unconstrained thermal actuator is proportional to input electrical power or voltage square. In the tested earthworm motors, the balance of the actuator forces, as well as the resisting deformation and friction forces, produces strokes that are proportional to the voltage not voltage squared; this results in the nearly linear trend shown in Figure 6.2.2.

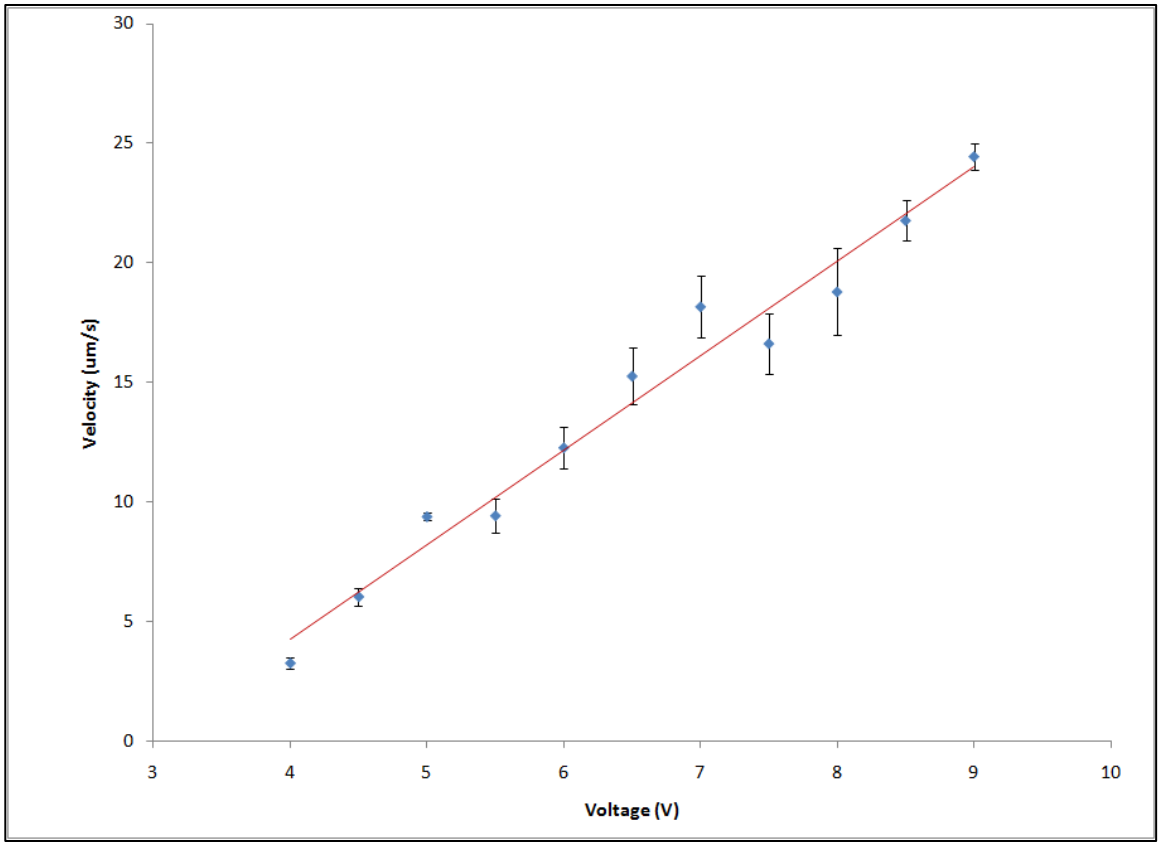

Figure 6.2.2 - Measured Shuttle Velocity vs. Voltage ($R^2 = 0.97$)

6.3 Shuttle Velocity vs. Driving Frequency

At a camera frame rate of 30 fps, the minimum experimental time resolution is 33 ms. At relatively low frequencies (10 Hz and below), the velocity can be calculated by simply measuring the shuttle displacement over a number of camera frames and dividing by the time elapsed (33 ms/frame). At higher frequencies, the motion of the shuttle can be very fast (1000's of μm/s) and the shuttle can move out of the camera field of view very rapidly (<10 ms). To improve the accuracy of all measurements, the velocity was measured using a

'burst' Labview VI that output a fixed number of steps (generally N = 50) at a fixed frequency. Thus, the time elapsed was known precisely: time = 1/frequency * N; the velocity was then calculated from the total measured shuttle displacement over the burst (generally 50 steps) divided by the burst time.

Figure 6.3.1 shows the measured velocity as a function of input frequency at a fixed voltage (7 V). The average of left and right velocities is shown: a minimum of twelve separate measurements (minimum six in each direction) were made for each data point: the plots show the mean, as well as one standard deviation. If the step size were independent of frequency then the velocity should be linearly proportional to frequency; as Hickey [47] showed, the thermal response of the actuators is reduced at higher frequencies where the actuator can no longer shed heat fast enough. The time constant (τ) is typically on the order of 100-200 μs for thermal actuators, leading to a cutoff frequency of approximately 1 kHz, where the step decreases to half its initial amplitude. The actuators in this study operated to beyond 10 kHz; this increase in operational frequency was due to the triangular lattice structure on the pushers, as seen in Figure 4.2.1 and Figure 4.2.2, which were added for purely mechanical reasons but also served as large and effective heat radiators. These structures meant that the thermal actuators have a relatively low temperature and require more voltage to operate, but have increased frequency range: only at 10 kHz do we begin to see and drop off from the linear relationship. At driving frequencies of 10 kHz, speeds of 17,000 μm/s were recorded; beyond 10 kHz, the actuators did not produce reliable motion. Past the 10 kHz mark, significant drift, variation in left/right speeds, as well as large standard deviation in average speed were observed.

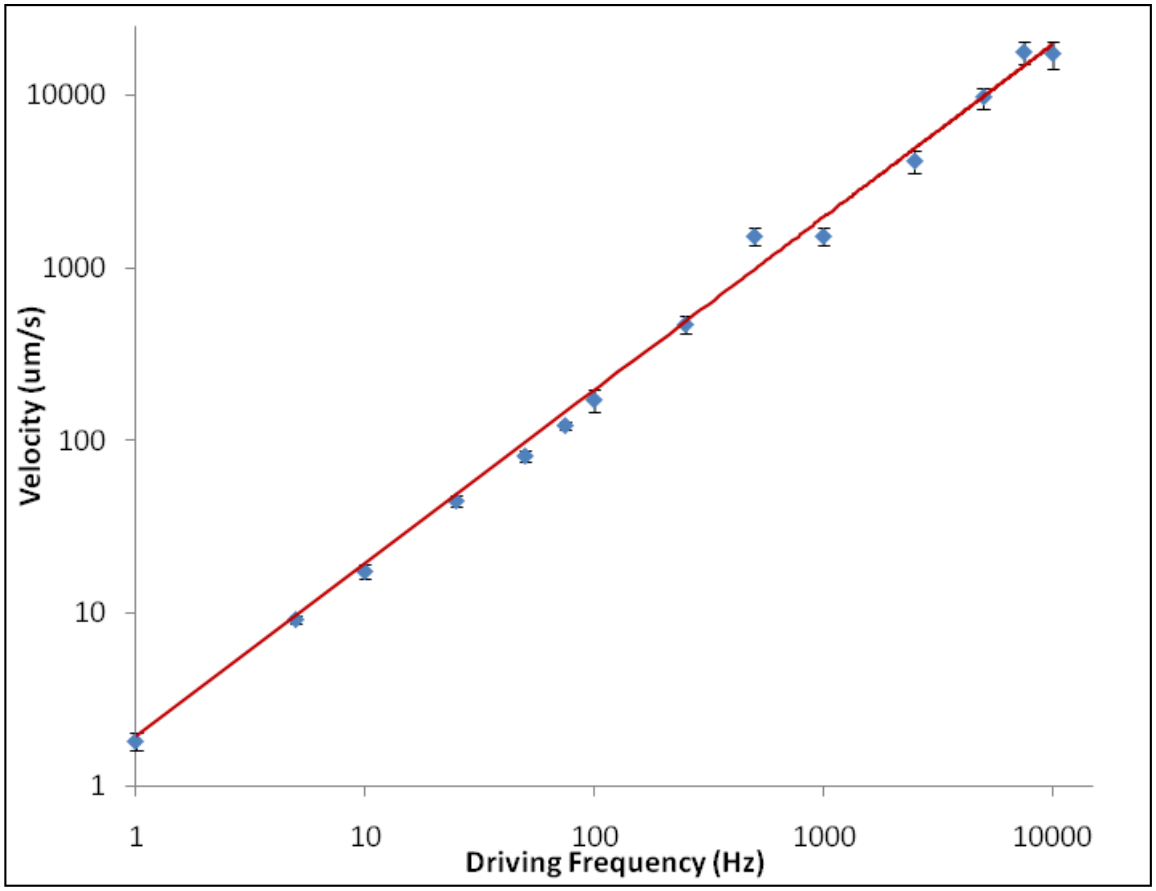

Figure 6.3.1 - Measured Shuttle Velocity vs. Frequency ($R^2 = 0.97$)

6.4 Shuttle Stall Force

For all force measurements, the shuttle was first assembled and aligned with the center of the chevrons (as described in Section 5.1). The device was then tested according to the procedures laid out in Section 5.3.

Figure 6.4.1 shows the maximum shuttle output force versus input voltage; the data points show the mean force and one standard deviation. Due to limitations on the number of chips available for testing and the problems encountered during force testing (as

described in Section 5.3.3), three experiments were conducted for each voltage, with the exception of 5 V and 9 V which only had one test each. The crawler produced a peak force of 80 μN at 9 V. While the velocity and force are both linear with voltage, the product of the two (the mechanical power produced) is proportional to voltage squared, or input electrical power. While the velocities from Figure 6.2.2 and Figure 6.3.1 are for no shuttle load speeds, the force from Figure 6.4.1 is the stall or slip force (no velocity). The peak producible power would occur at half the no load speed and at half the stall force. At 9 V, this would produce a peak output mechanical power of:

$$\left(\frac{1000\frac{\mu m}{s}}{2}\right)\left(\frac{80\mu N}{2}\right) = 20\ pico\ watts$$

Equation 6.4.1

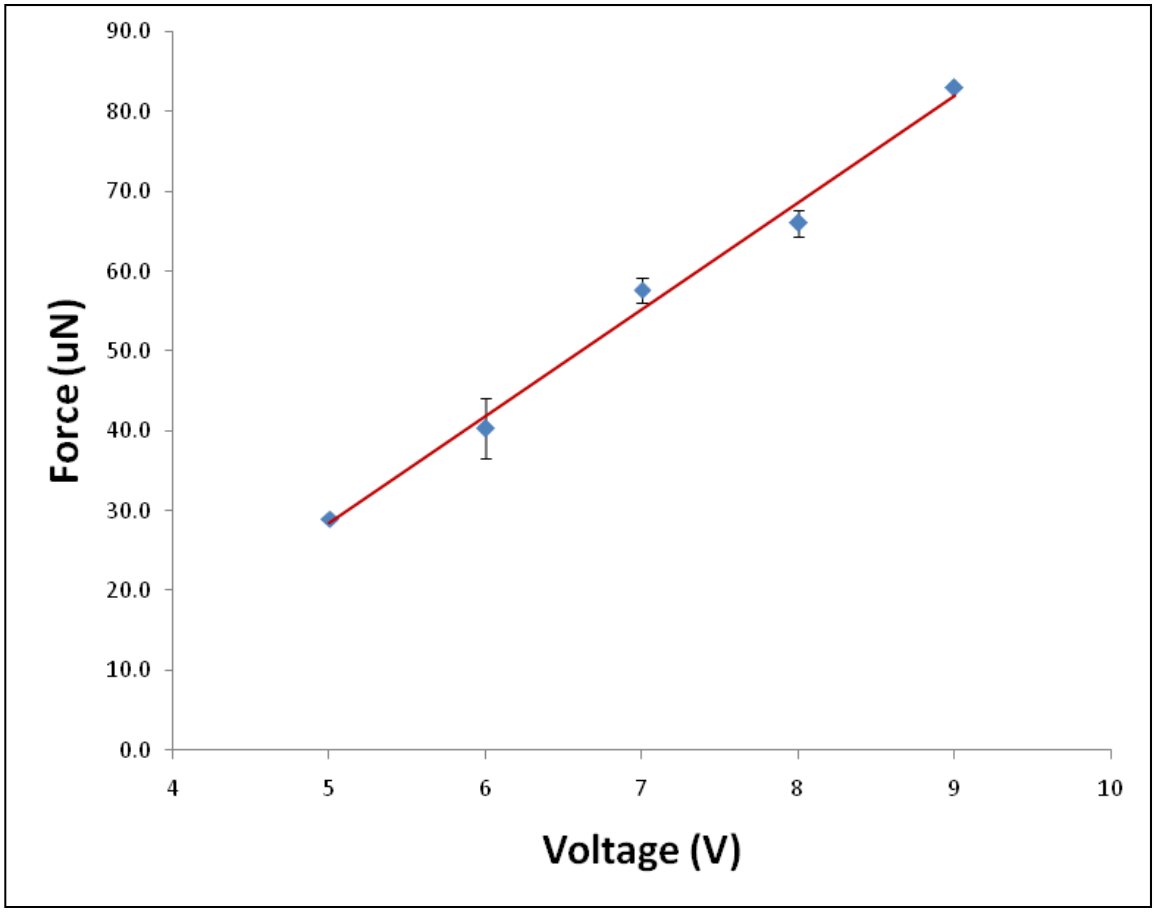

Figure 6.4.1 - Experimentally Measured Shuttle Force vs. DC Voltage ($R^2 = 0.99$)

Chapter 7: Future Work & Recommendations

There are a number of possible earthworm design variations that can still be investigated. As described in this chapter, changes in the micro-scale earthworm's design may allow higher efficiencies, increased force, range of motion, reduced assembly requirements, or the gain of an additional degree of freedom. Below, a number of possible variations are discussed:

1. The current design utilizes thermal actuators; a design using an alternate actuator type, such as electrostatic comb drives or Piezoelectrics, would offer higher efficiency and higher frequency response, albeit at the expense of higher voltage requirements or more complex manufacturing processes.

2. A crawler design using greater structure heights would allow larger shuttle forces. While crawlers were designed and tested using the SOIMUMPs process (see Appendix C), which offers 25 μm structure heights, this process was found to be unsuitable for this crawler design. MetalMUMPs, with its 20.5 μm structure heights offers another possible process for earthworm fabrication to be investigated.

3. With the existing crawler design, a shuttle that is slightly narrower than the gap between opposing sets of pushers is used to aide in crawler assembly. This means that there is a small gap between the pushers and shuttle that must first be closed, and thus is normally unclamped. A design utilizing shuttles slightly larger than the actuators, as shown in Figure 7.0.1, would produce a normally clamped design,

remaining clamped even when electrical power is removed. To assist with the device's assembly, the ends of the pushers should be sloped to allow the shuttle to compress as it is pushed to its final position.

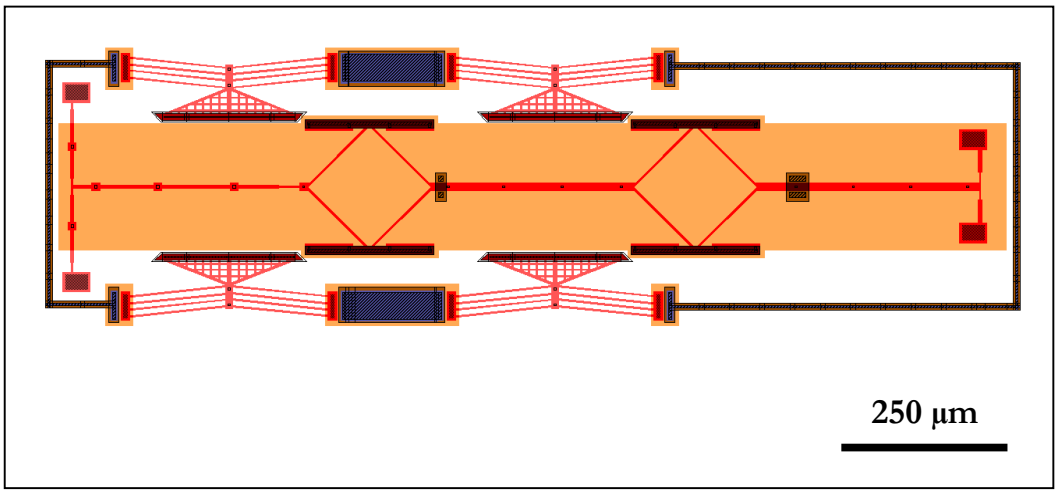

Figure 7.0.1 – Unassembled Normally Clamped Earthworm Crawler

4. To transport the devices after manufacturing, the shuttles must be affixed to the chip's surface to prevent damage. In the tested design, this was achieved using tethered shuttles, which had to be broken and assembled as described in Section 5.1. A design using shuttles attached to the chip's surface by long folded suspensions would eliminate the assembly step, allowing large arrays of crawlers to be used without post-processing; however, the suspensions would limit the overall range of such a design. A designed crawler implementing suspensions can be seen in Figure 7.0.2; it should be noted that this design still uses breakable tethers as an extra precaution, but these would not be required for production of the crawler.

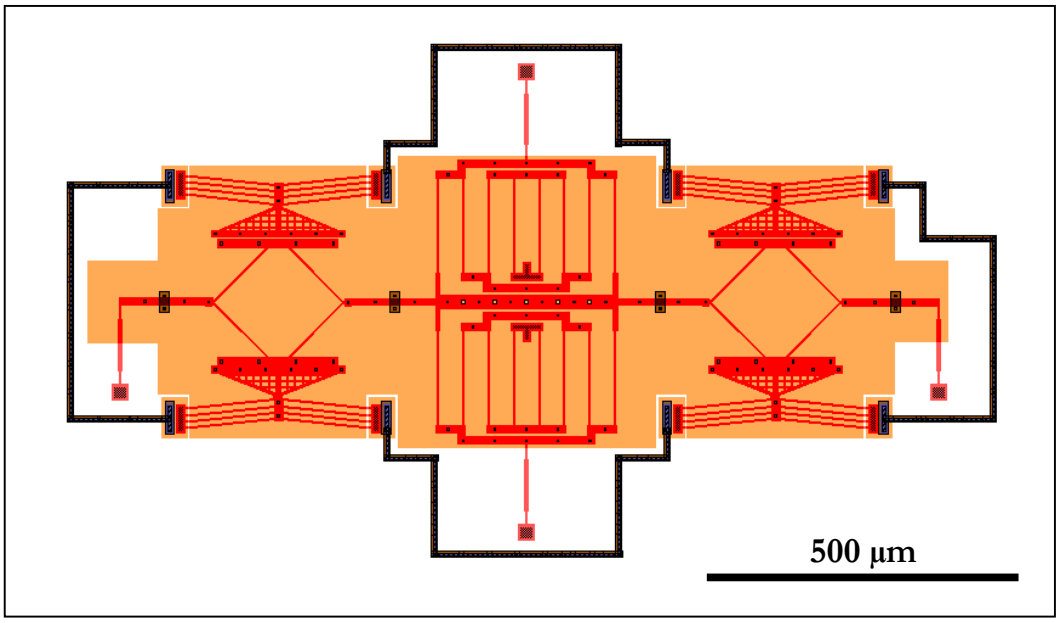

Figure 7.0.2 - Pre-Assembled Earthworm With Suspension

5. Currently, the earthworm crawler is only capable of lateral motion. To allow two degree-of-freedom (2DOF) motion, two sets of earthworm crawlers can be attached perpendicular to each other via a suspension that is selectively stiff. These suspensions must be extremely rigid when pushed parallel to the suspension, yet soft when pushed perpendicular to their orientation; they are used to allow motion of the center 'cross' section of the 2DOF earthworm, yet still allow the pushers and diamonds to remain parallel. An example of a designed 2DOF crawler can be seen in Figure 7.0.3.

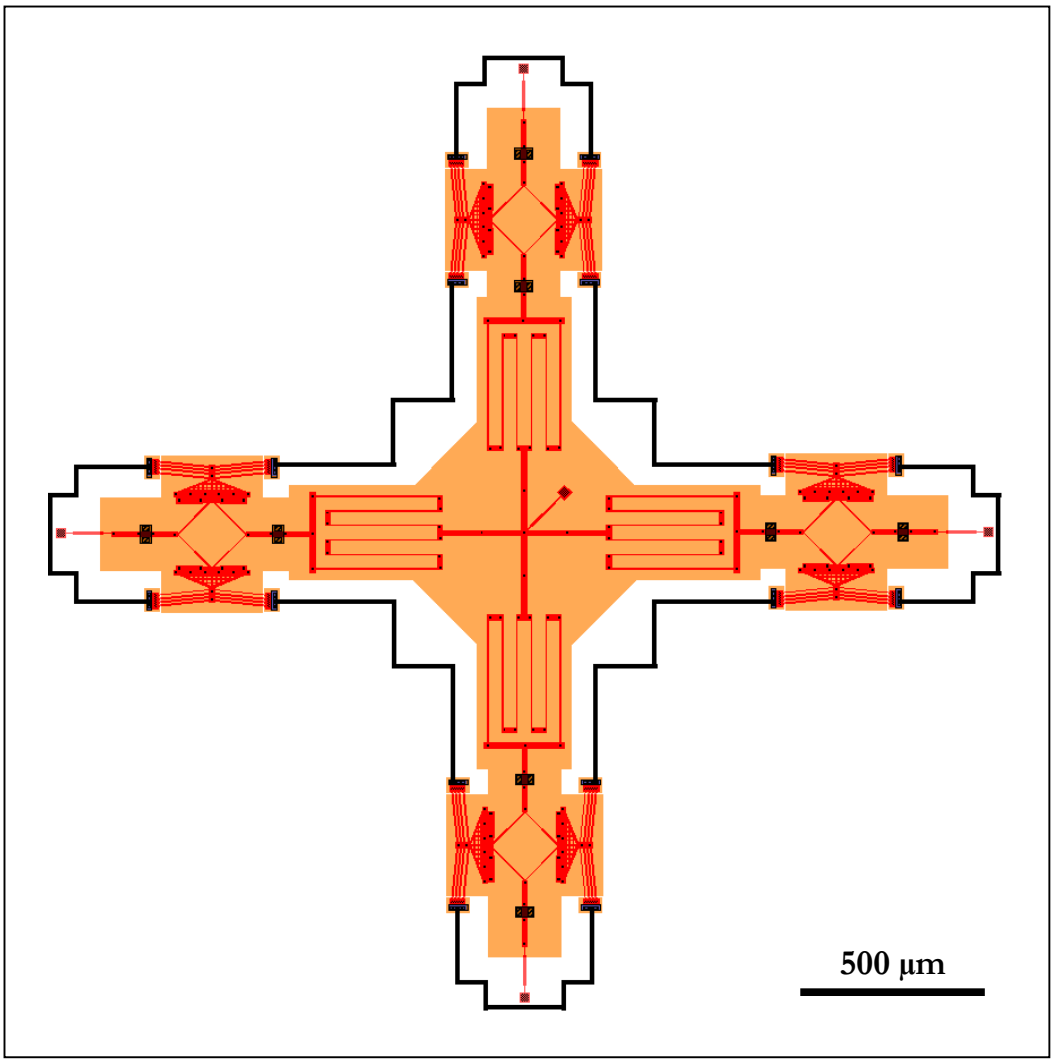

Figure 7.0.3 - 2DOF Earthworm

6. The implementation of a closed-loop optical control system allows the use of multiple sets of motors to be used to drive a two-diamond shuttle over an indefinite length of track; an example of one such track can be seen in Figure 7.0.4. This combination will allow extraordinarily long actuator motion, with the ability to precisely control the location of the shuttle. To simplify the multiple-motor crawler, breeched grounds (using the silicon substrate as a common ground) should be used;

these grounds appear as squares connected to the chevrons in Figure 7.0.4. Another option to allow indefinite motion that may be investigated would be the integration of the chevrons into the shuttle itself, with the shuttle pushing against a fixed track; this powered shuttle would require electrical contacts on the chip's surface, and would most likely have the greatest chance of success if manufactured in the MetalMUMPs process.

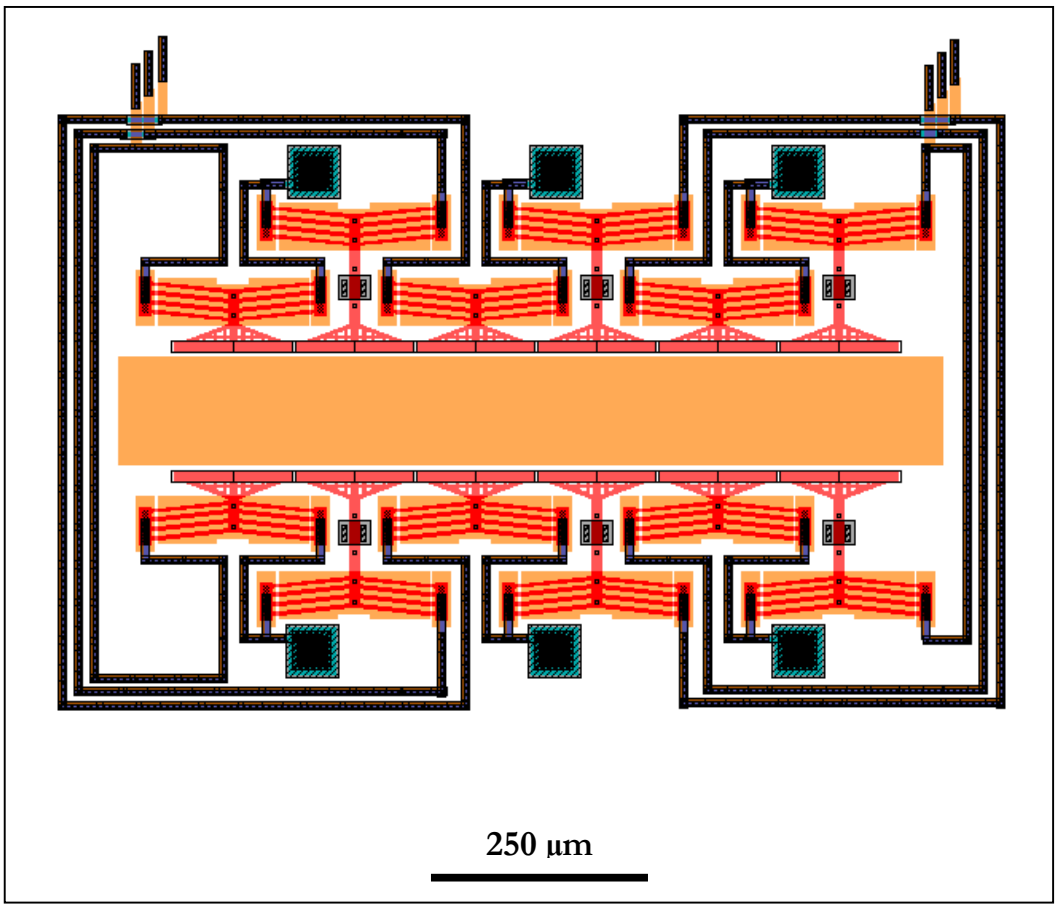

Figure 7.0.4 - Earthworm With Multiple Motors for Longer Distances

7. Another possible variant of the micro-scale earthworm crawler would be to investigate the feasibility of a milli-scale crawler, similar to that developed by Toda [11]. This crawler would be capable of exerting macro-scale displacements and forces, and could possibly be used as a high-precision linear actuator for future use as a substitute for the Zaber actuators currently used in the Dalhousie MEMS Lab.

Chapter 8: Conclusions

This section will cover final remarks for the reported design, including comparisons to existing crawler designs, experimental difficulties encountered, testing results, and thoughts on where this research could be heading next.

8.1 Comparison to Existing Crawlers

There are four main parameters that could be used to characterize a MEMS motor: footprint area, range of motion, output force, and maximum speed. Unfortunately, not all authors reporting motor performance list these parameters. It is often difficult to compare works that are similar in operation, but vary widely in size and shape. Therefore, in order to have a basis for comparison, the device properties can be first normalized by their footprint size.

Te motor developed in this work is compared against existing crawlers in Table 8.1.1, with the device's range per unit size plotted against the device's force per unit size and the device's speed per unit size being shown in Figure 8.1.1 and Figure 8.1.2 respectively. As shown in these figures, the earthworm crawler develops both relatively large force and large range for it size. In addition to high forces and ranges, the earthworm's maximum speed normalized by the device size was also high (note that speeds are less commonly reported than other parameters). While the MEMS earthworm crawler performed better in most areas than existing designs, its performance could be further improved through the use of multiple motors, as discussed in Section 7. It should be noted that in Table 8.1.1, Figure 8.1.1, and Figure 8.1.2, only the primary author's name is listed for each entry.

Paper	Voltage (V)	Range (µm)	Speed (µm/s)	Force (µN)	Length (µm)	Width (µm)	Area (mm^2)	Type	Range/ Area (m/m^2)	Force/ Area (N/m^2)	Speed/ Area ([m/s]/m^2)
Kwon [3]		50	400	50	1,750	1,750	3.06	ES	16.3	16	131
Brown [7]	3	140	700	138	1,500	500	0.75	ET	187	184	933
Erismis [9]	7	36		30	3,700	1,800	6.66		5.41	4.5	-
Erismis [9]	10	48		50	3,700	1,800	6.66		7.21	7.5	-
Erismis [9]	16	70	300	110	4,800	2,200	10.6		6.63	10	28
Pham [10]	4	225	190		600	800	0.48	ET	167	-	396
Toda [11]	200	600		16,000	20,000	6,000	120	PZ / ES	5.00	133	-
Yeh [12]	33	80		260	2,000	1,500	3.00	ES	26.7	87	-
Yeh [12]		52	4,000		1,500	1,000	1.50	ES	34.7	-	2,667
de Boer [13]	150	140	4,400	450	1,500	600	0.90	ES	156	500	4,889
Sarajlic [14]	55	140	3,600	1,700	412	286	0.12	ES	1,188	14,427	30,552
Tas [15]	40	15		3	500	400	0.20	ES	75.0	15	-
THIS WORK	9	350	17,000	80	800	400	0.32	ET	1,094	250	53,125

Table 8.1.1 - Comparison of Micro-Earthworm to Existing Crawlers

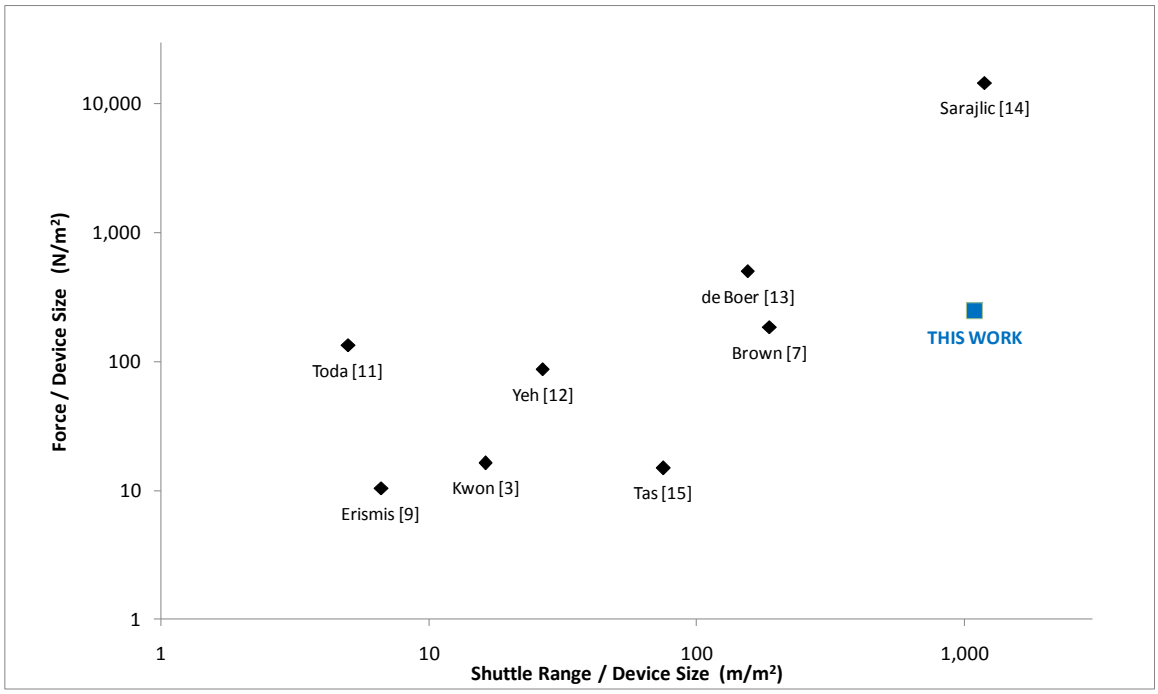

Figure 8.1.1 - Micro-Earthworm's Normalized Force Compared to Existing Crawlers

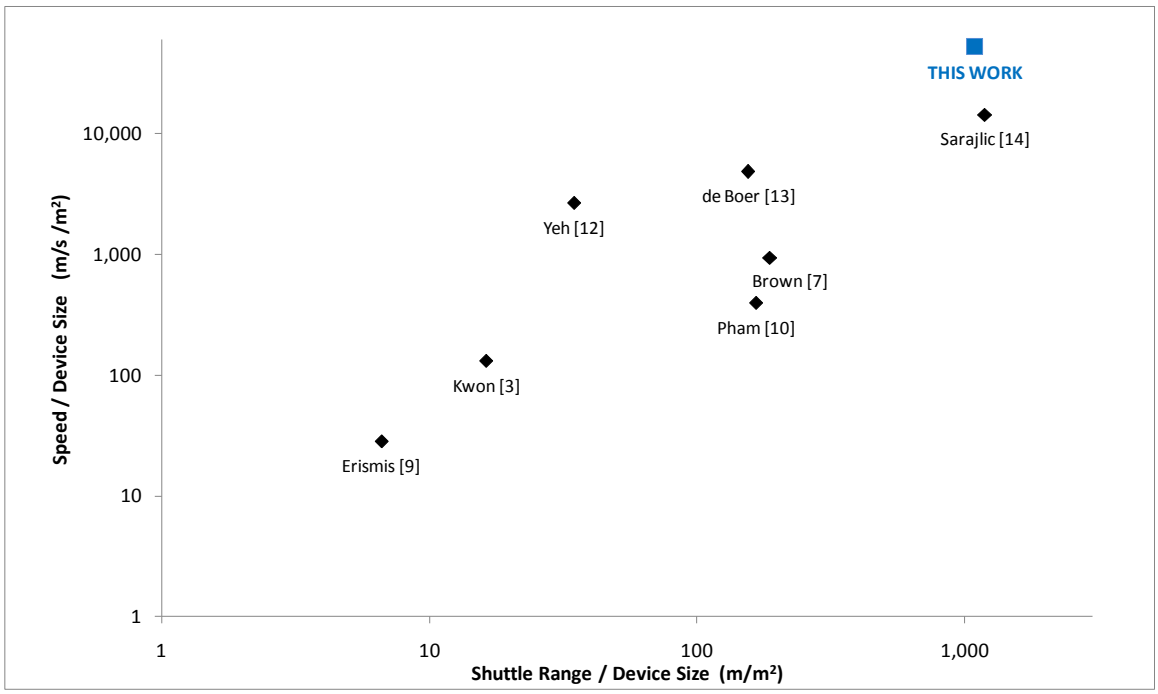

Figure 8.1.2 - Micro-Earthworm's Normalized Velocity Compared to Existing Crawlers

8.2 Conclusions

This work presented the design and testing of a functioning high precision, high speed, long range peristaltic micro-motor inspired by the motion of a common earthworm. This micro-scale earthworm crawler showed that biomimicry, specifically motion based on the motion of a common earthworm, is a feasible design basis for MEMS devices. This work satisfied the following objectives:

- Existing micro-crawler designs were researched.
- The motion of an earthworm was researched.

- A macro-scale model of a robotic crawler based on the motion of an earthworm was constructed and tested.
- A micro-scale earthworm was designed and constructed using a MUMPS process.
- The micro-earthworm's performance and was tested and compared to existing micro-crawler designs.

By using only clamping actuators to sequentially squeeze a flexible shuttle, the shuttle was peristaltically moved back and forth over long ranges. The design is capable of operating independently of the type of actuator used, and therefore capable of being operated by any type of MEMS actuator. Chevron actuators were chosen to power the micro-scale earthworm crawler based on their reliability, force, and displacement.

The most common difficulty encountered during experimentation was stiction, the most likely cause of which was high humidity levels during testing; a more efficient laboratory climate control system, or chips sealed from the surrounding conditions might help alleviate these issues.

The tested design, measuring 400 μm by 800 μm, provided a 350 μm range of motion, although the device's range is theoretically limited only by the number of motor pairs, allowing an unlimited range of motion. The micro-scale earthworm crawler used two pairs of thermal chevron-based squeezing motors operating from 4-9 V, and 0-10 kHz. Speeds in the range of 1000 μm/s at 1 kHz were measured, with peak speeds as high as 17,000 μm/s recorded at 10 kHz; the device's maximum stall force was measured at 80 μN. Relative to its size, this device offers a large range of motion, large force, and the capacity for high-speed travel.

Appendix A

The process flow for MEMSCAP's PolyMUMPs process can be seen from Figure A.1 to Figure A.15.

Step 1: The surface of the starting n-type (100) wafers are heavily doped with phosphorus in a standard diffusion furnace using a PSG film as the dopant source. After removal of this PSG film, a 600 nm blanket layer of low stress silicon nitride (Nitride) is deposited followed by a blanket layer of 500 nm polysilicon (Poly 0). The wafers are then coated with UV-sensitive photoresist.

Figure A.1 - PolyMUMPs Process-Flow Step 1 [51]

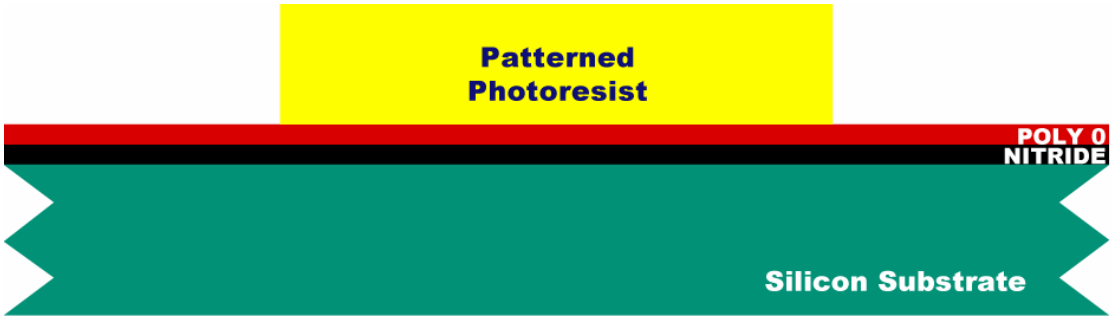

Step 2: The photoresist is lithographically patterned by exposing it to UV light through the first level mask (POLY0) and then developing it. The photoresist in exposed areas is removed leaving behind a patterned photoresist mask for etching.

Figure A.2 - PolyMUMPs Process-Flow Step 2 [51]

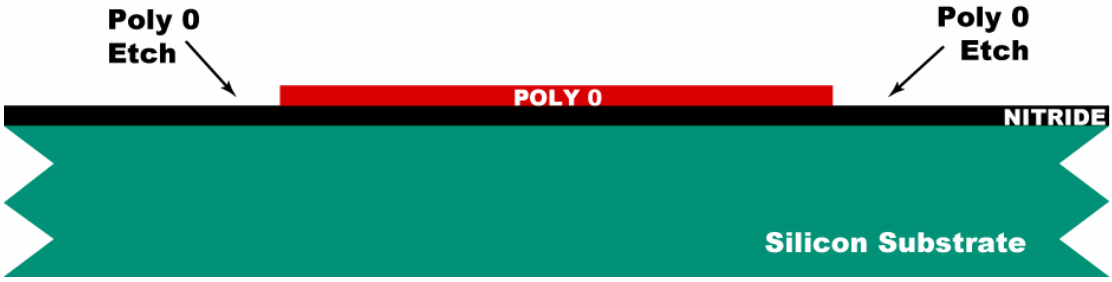

Step 3: Plasma etching is used to remove the unwanted polysilicon. After the etch, the photoresist is chemically stripped in a solvent bath. This method of patterning the wafers with photoresist, etching and stripping the remaining photoresist is used repeatedly in the PolyMUMPs process.

Figure A.3 - PolyMUMPs Process-Flow Step 3 [51]

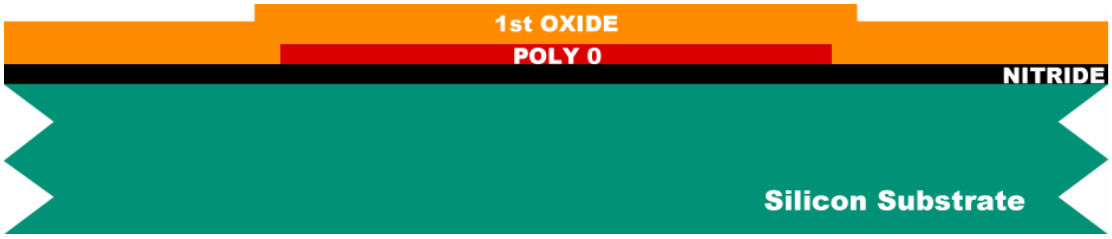

Step 4: A 2.0 µm layer of PSG is deposited on the wafers by low pressure chemical vapor deposition (LPCVD). This is the first sacrificial layer.

Figure A.4 - PolyMUMPs Process-Flow Step 4 [51]

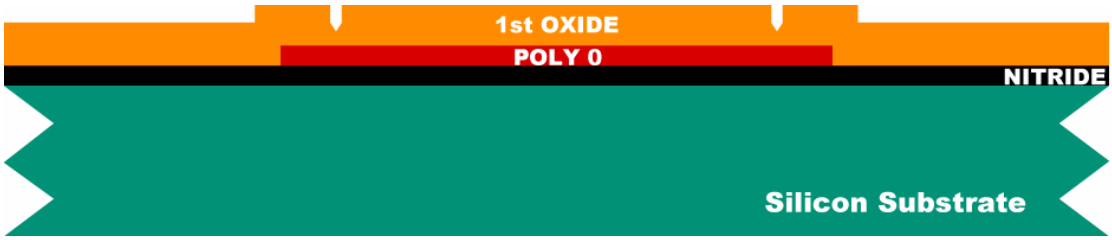

Step 5: The wafers are coated with photoresist and the second level (DIMPLE) is lithographically patterned. The dimples, 750 nm deep, are reactive ion etched (RIE) into the first oxide layer. After the etch, the photoresist is stripped.

Figure A.5 - PolyMUMPs Process-Flow Step 5 [51]

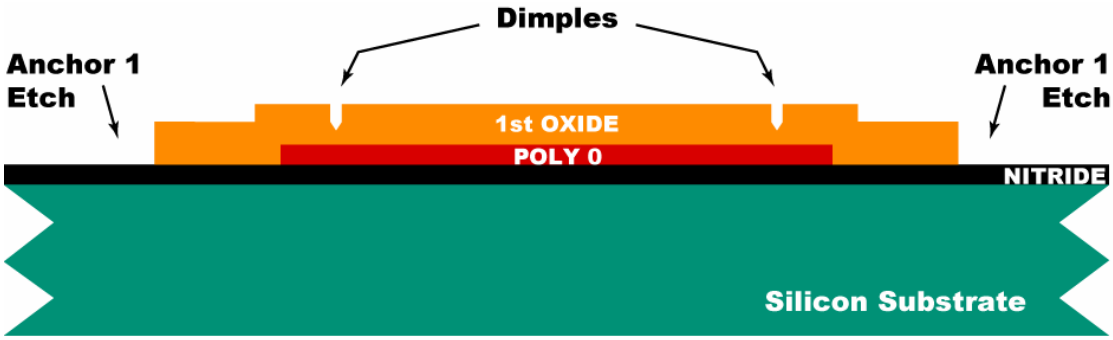

Step 6: The wafers are re-coated with photoresist and the third level (ANCHOR1) is lithographically patterned. The unwanted oxide is removed in an RIEprocess and the photoresist is stripped.

Figure A.6 - PolyMUMPs Process-Flow Step 6 [51]

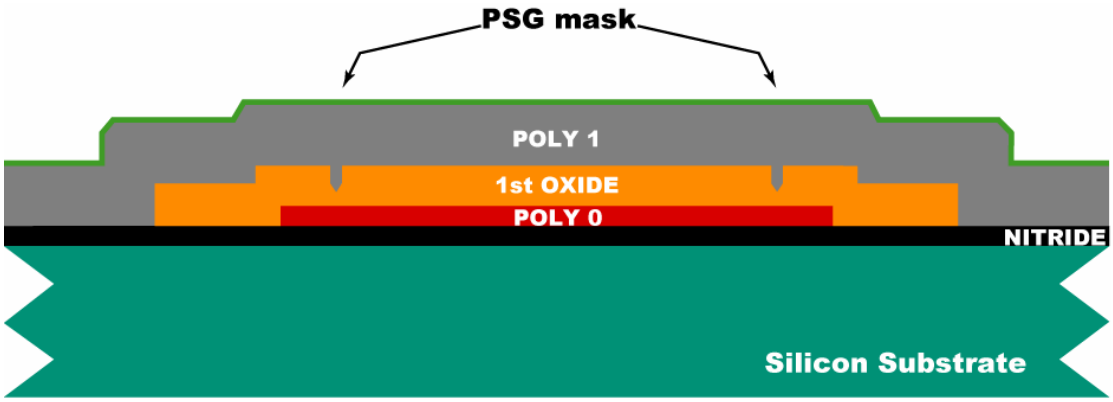

Step 7: A blanket 2.0 µm layer of un-doped polysilicon is deposited by LPCVD followed by the deposition of 200 nm PSG and a 1050°C/1 hour anneal. The anneal serves to both dope the polysilicon and reduce its residual stress.

Figure A.7 - PolyMUMPs Process-Flow Step 7 [51]

Step 8: The wafer is coated with photoresist and the fourth level (POLY1) is lithographically patterned. The PSG is first etched to create a hard mask and then Poly 1 is etched by plasma processing. After the etch is completed, the photoresist and PSG hard mask are removed.

Figure A.8 - PolyMUMPs Process-Flow Step 8 [51]

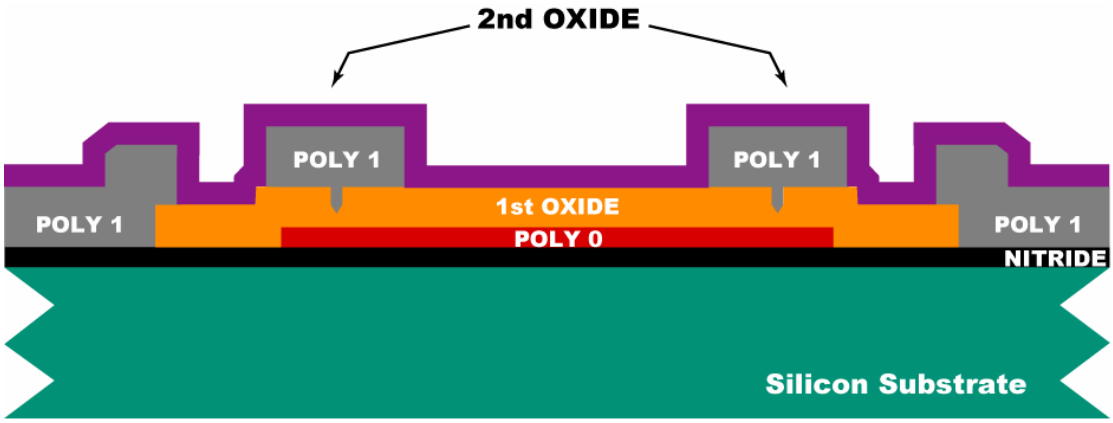

Step 9: The Second Oxide layer, 0.75 µm of PSG, is deposited on the wafer. This layer is patterned twice to allow contact to both Poly 1 and substrate layers.

Figure A.9 - PolyMUMPs Process-Flow Step 9 [51]

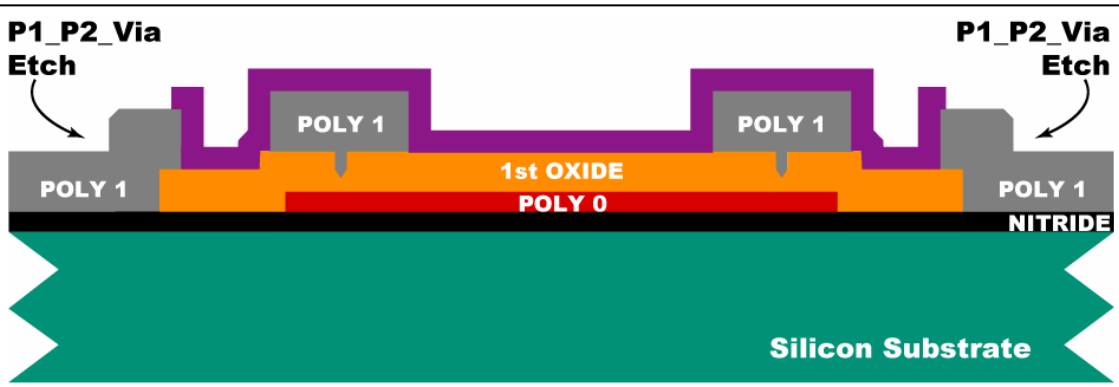

Step 10: The wafer is coated with photoresist and the fifth level (POLY1_POLY2_VIA) is lithographically patterned. The unwanted Second Oxide is RIE etched, stopping on Poly 1, and the photoresist is stripped.

Figure A.10 - PolyMUMPs Process-Flow Step 10 [51]

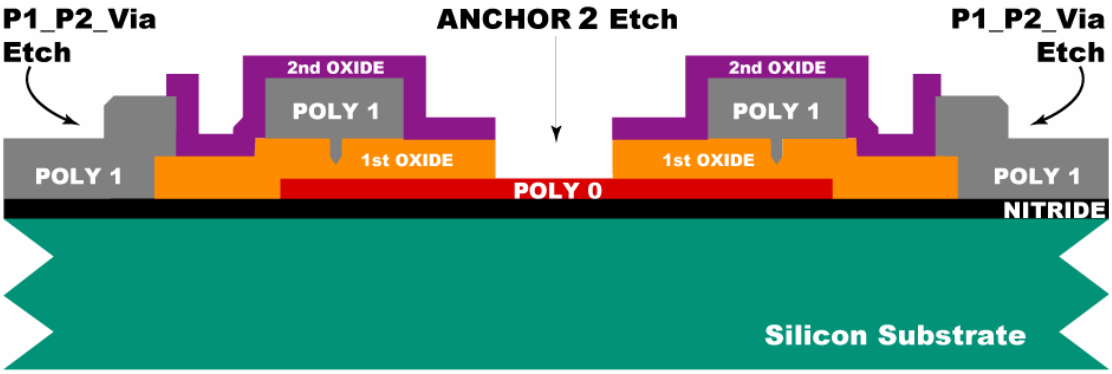

Step 11: The wafer is re-coated with photoresist and the sixth level (ANCHOR2) is lithographically patterned. The Second and First Oxides are RIE etched, stopping on either Nitride or Poly 0, and the photoresist is stripped. The ANCHOR2 level provides openings for Poly 2 to contact with Nitride or Poly 0.

Figure A.11 - PolyMUMPs Process-Flow Step 11 [51]

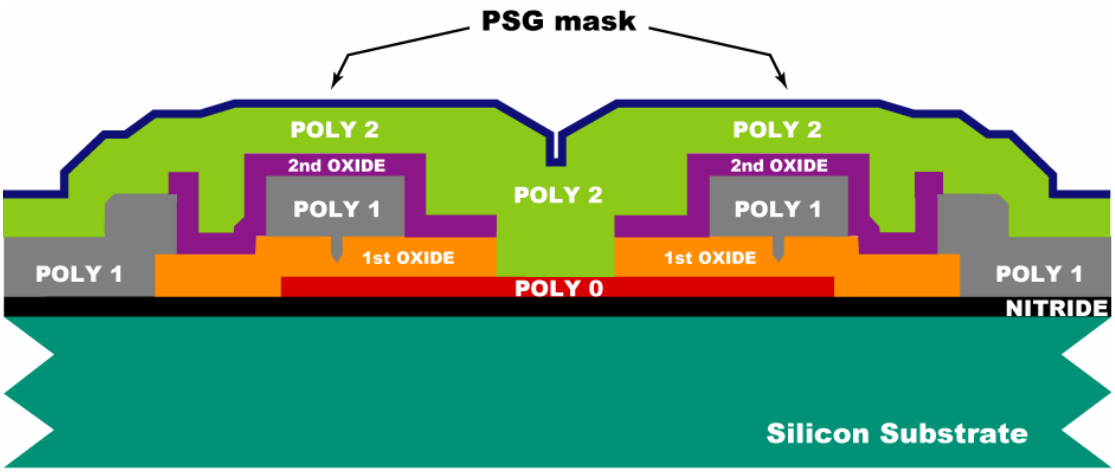

Step 12: A 1.5 µm un-doped polysilicon layer is deposited followed by a 200 nm PSG hardmask layer. The wafers are annealed at 1050°C for one hour to dope the polysilicon and reduce residual stress.

Figure A.12 - PolyMUMPs Process-Flow Step 12 [51]

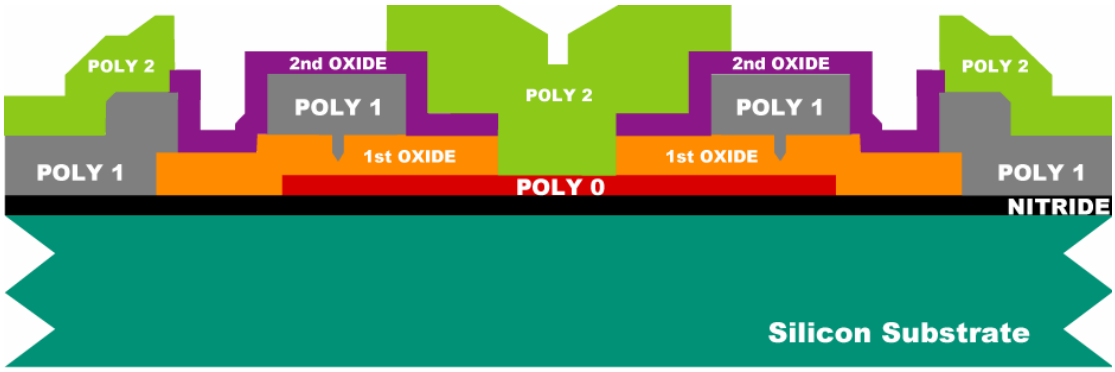

Step 13: The wafer is coated with photoresist and the seventh level (POLY2) is lithographically patterned. The PSG hard mask and Poly 2 layers are etched and the photoresist and hard mask are removed. All mechanical structures have now been fabricated. The remaining steps are to deposit the metal layer and remove the sacrificial oxides.

Figure A.13 - PolyMUMPs Process-Flow Step 13 [51]

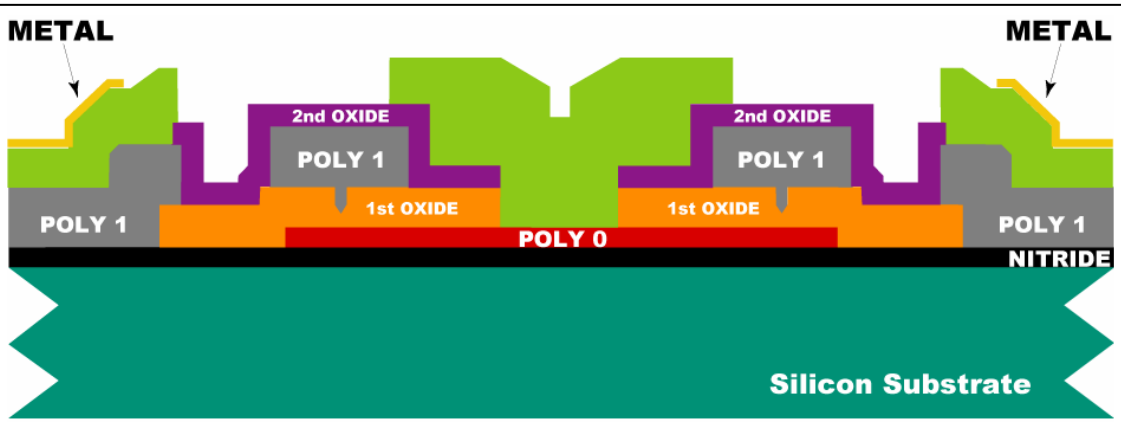

Step 14: The wafer is coated with photoresist and the eighth level (METAL) is lithographically patterned. The metal (gold with a thin adhesion layer) is deposited by lift-off patterning which does not require etching. The side wall of the photoresist is sloped at a reentrant angle, which allows the metal to be deposited on the surfaces of the wafer and the photoresist, but provides breaks in the continuity of the metal over the photoresist step. The photoresist and unwanted metal (atop the photoresist) are then removed in a solvent bath. The process is now complete and the wafers can be coated with a protective layer of photoresist and diced. The chips are sorted and shipped.

Figure A.14 - PolyMUMPs Process-Flow Step 14 [51]

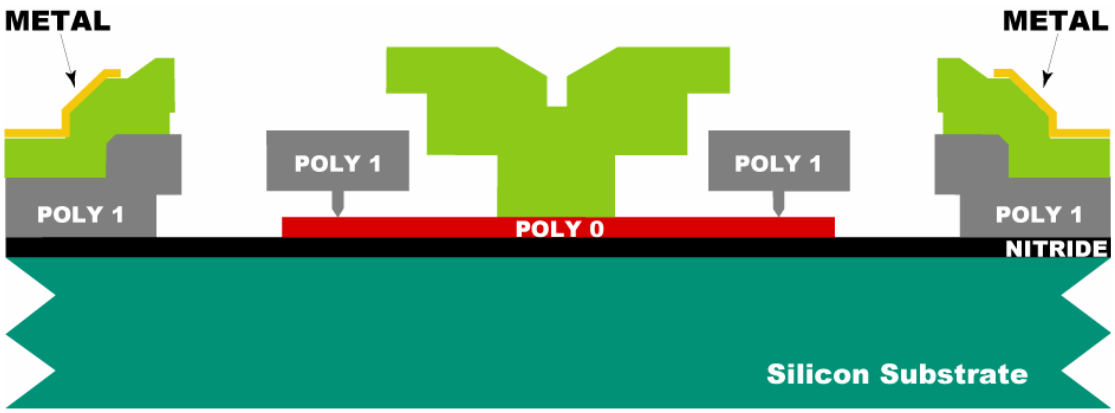

Step 15: The structures are released by immersing the chips in a 49% HF solution. The Poly 1 "rotor" can be seen around the fixed Poly 2 hub. The stacks of Poly 1, Poly 2 and Metal on the sides represent the stators used to drive the motor electrostatically.

Figure A.15 - PolyMUMPs Process-Flow Step 15 [51]

Appendix B

Figure B.1 shows the dimensions for the HiTEC servo used in the macro-scale earthworm crawler; the fabrication drawings for the macro model can be seen from Figure B.2 to Figure B.8.

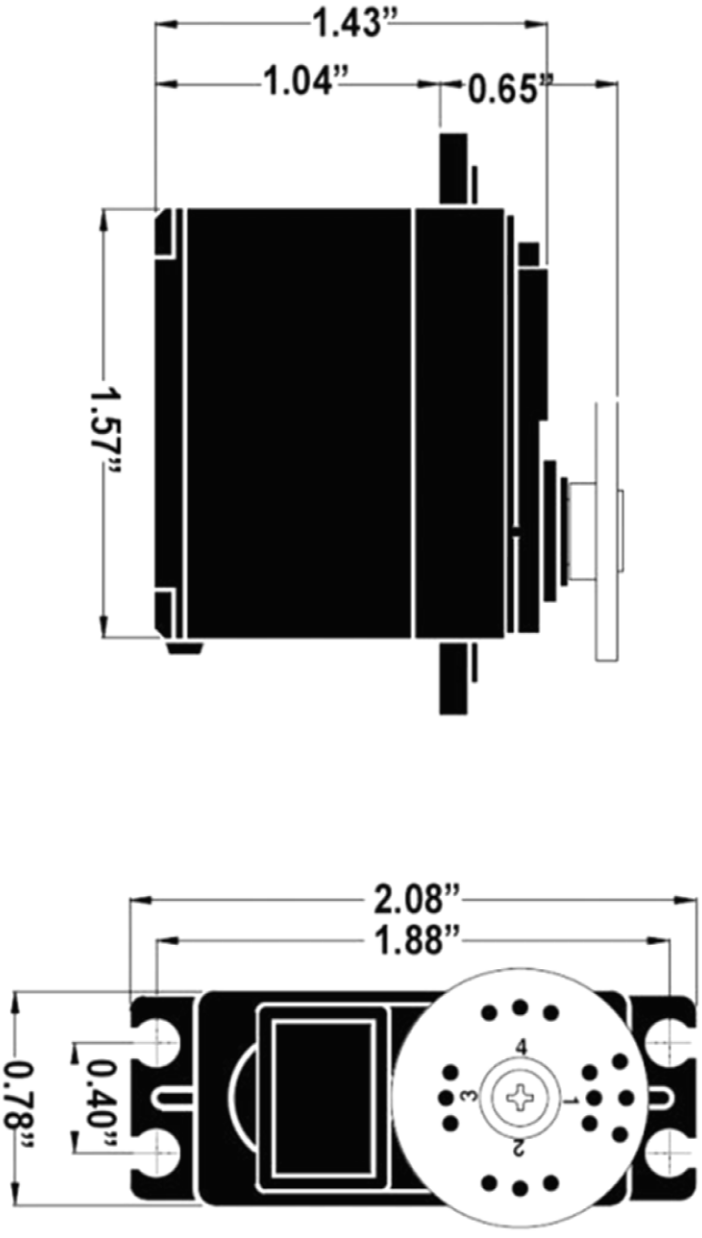

Figure B.1 - HiTEC Servo Dimensions [52]

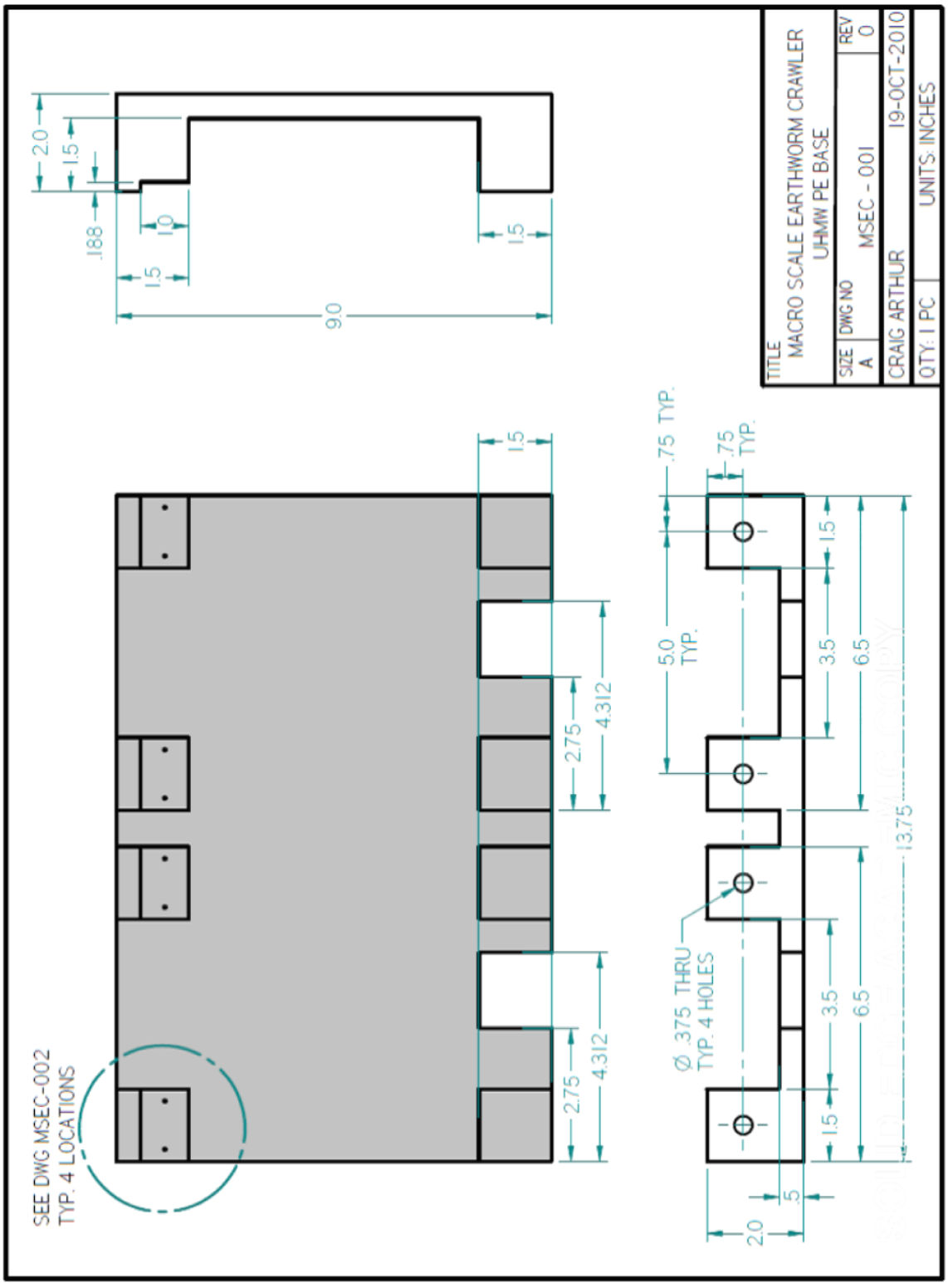

Figure B.2 – Drawing # MSEC-001

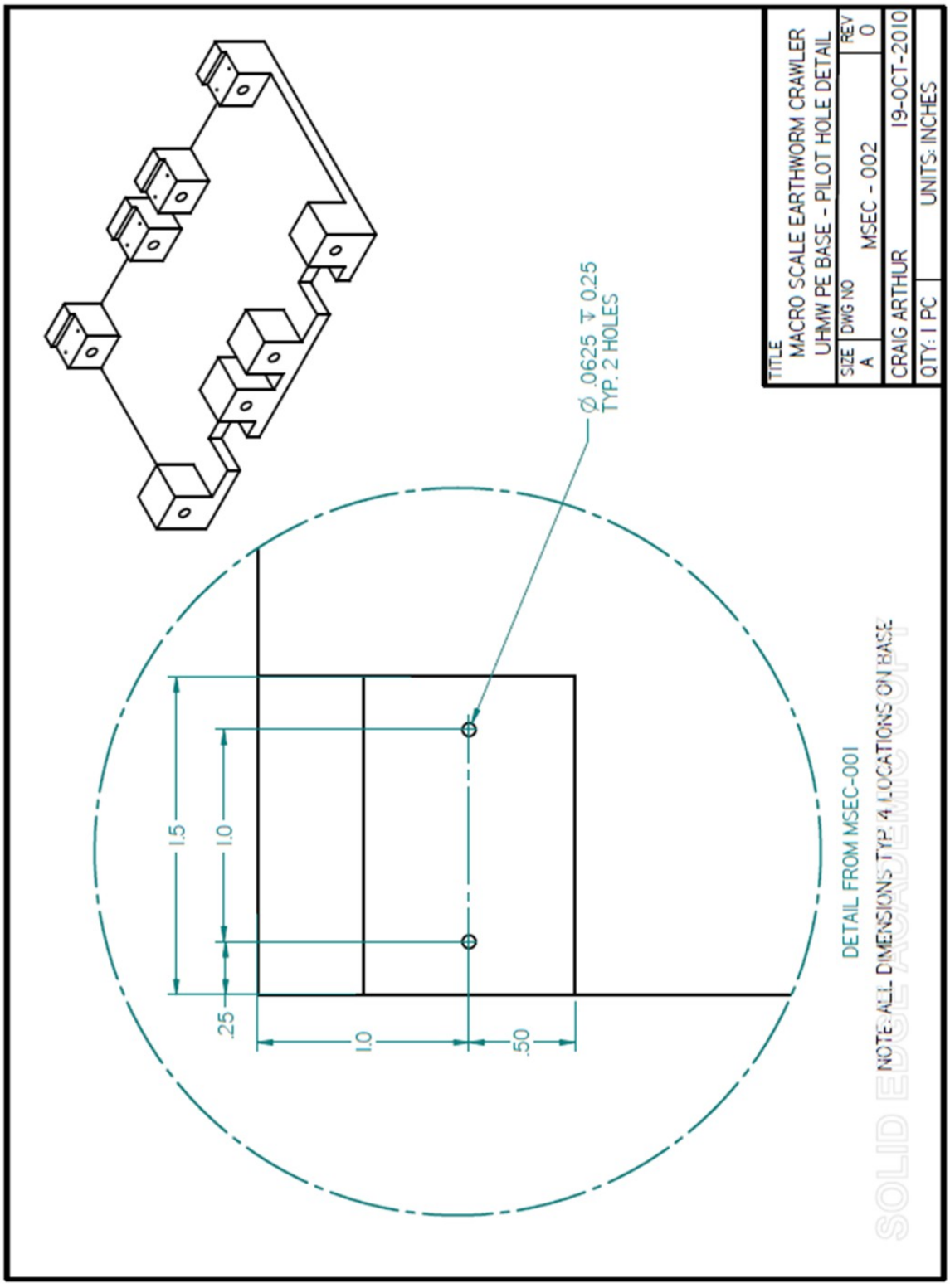

Figure B.3 - Drawing # MSEC-002

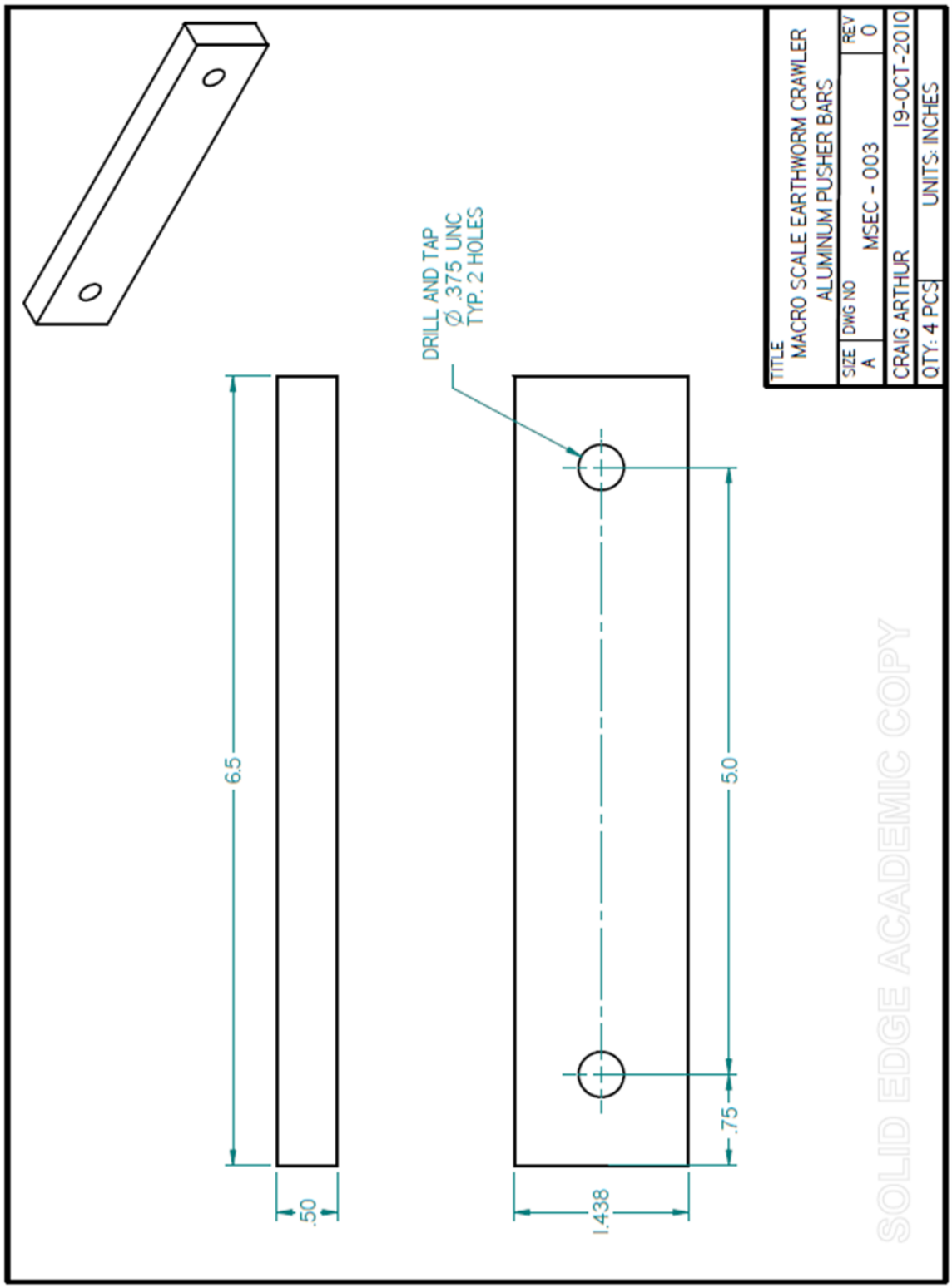

Figure B.4 - Drawing # MSEC-003

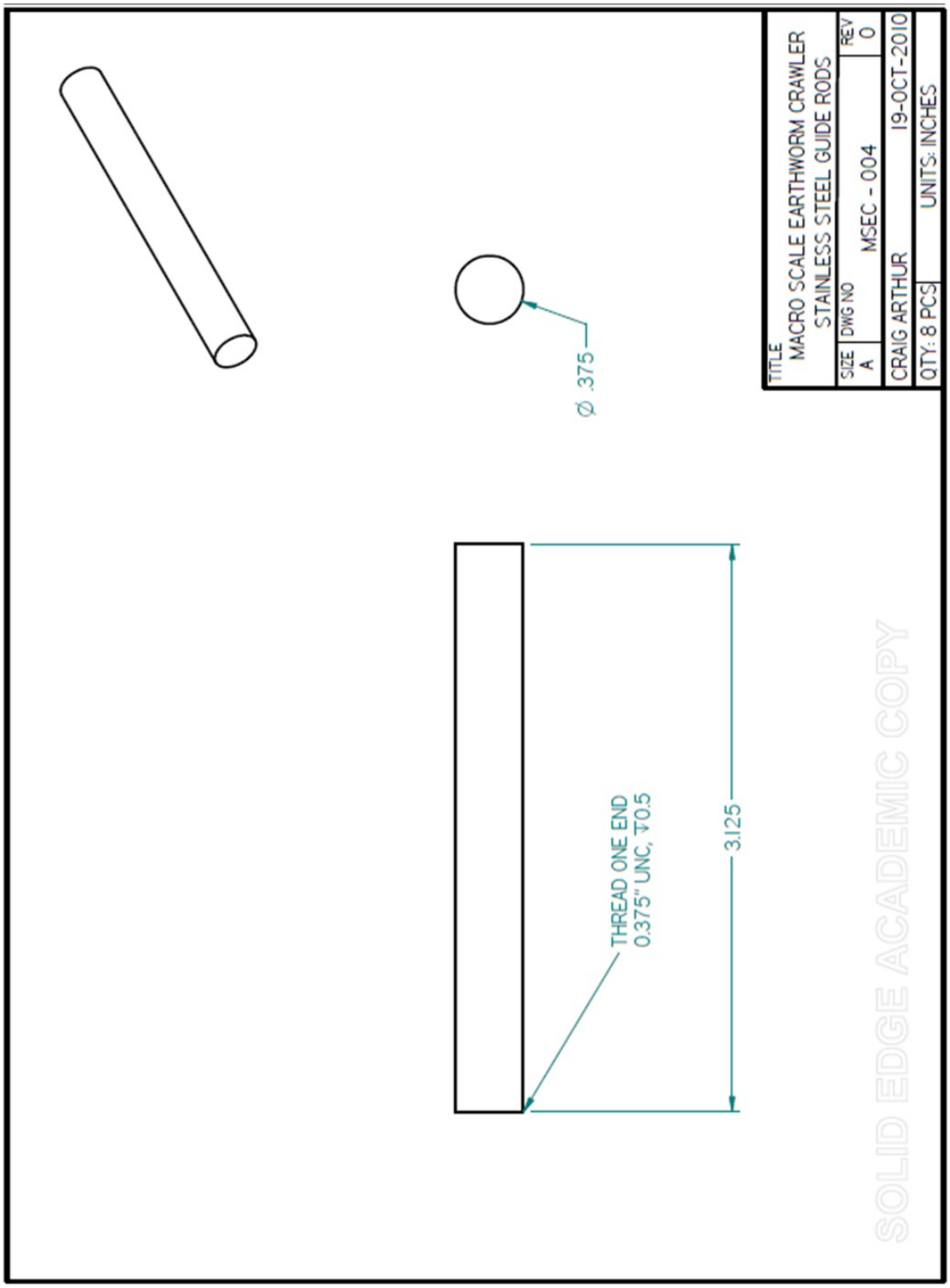

Figure B.5 - Drawing # MSEC-004

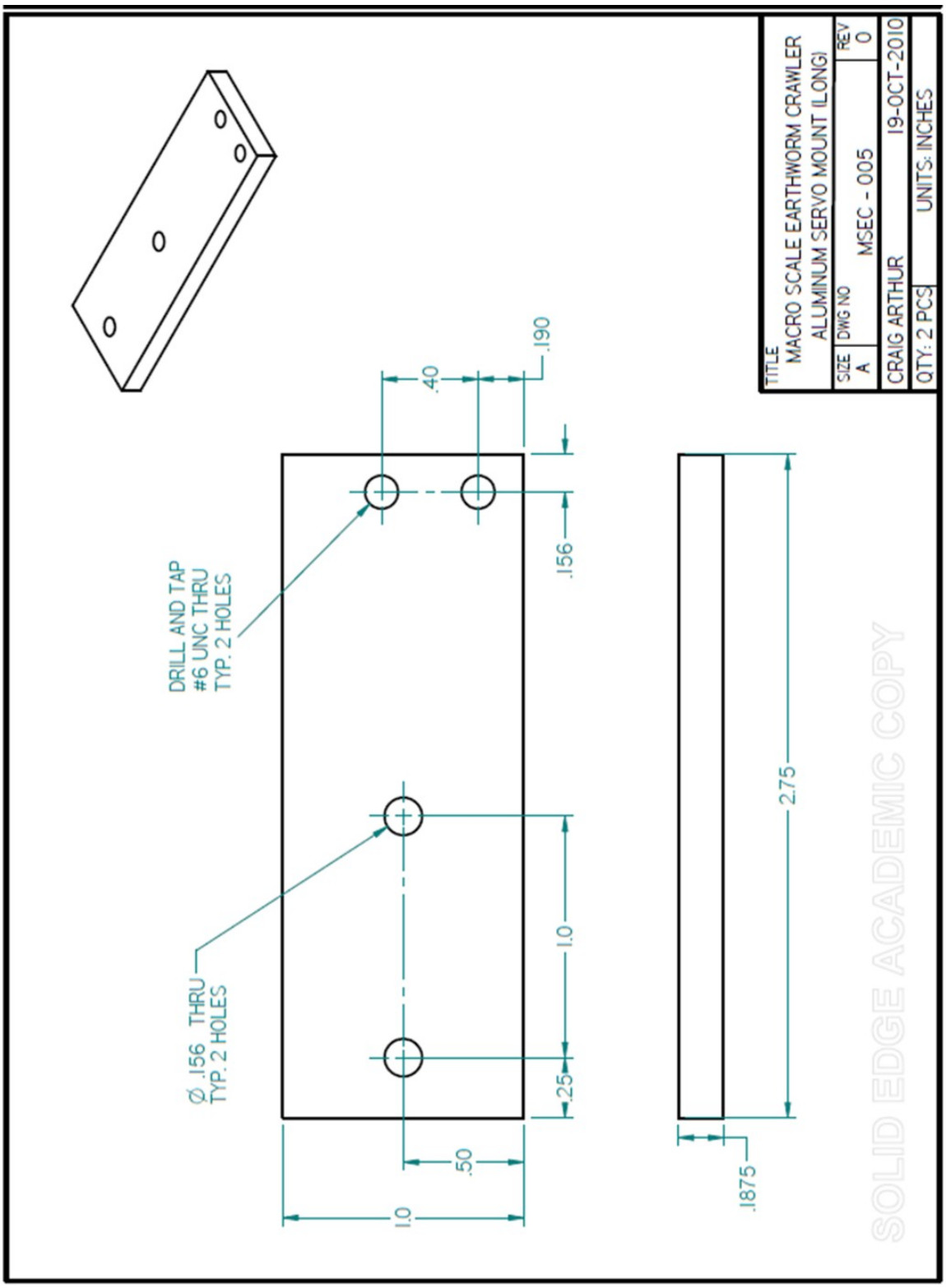

Figure B.6 - Drawing # MSEC-005

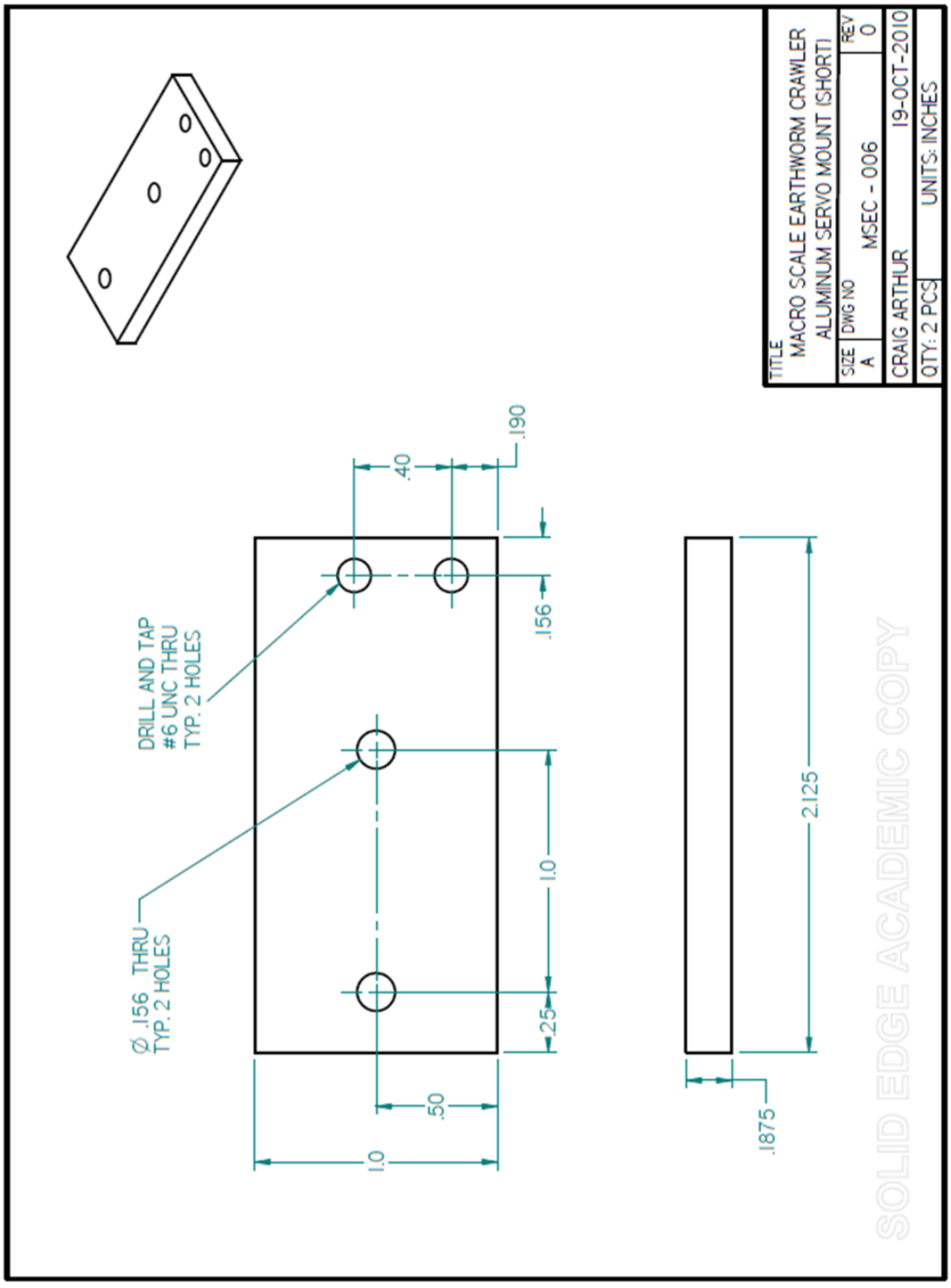

Figure B.7 - Drawing # MSEC-006

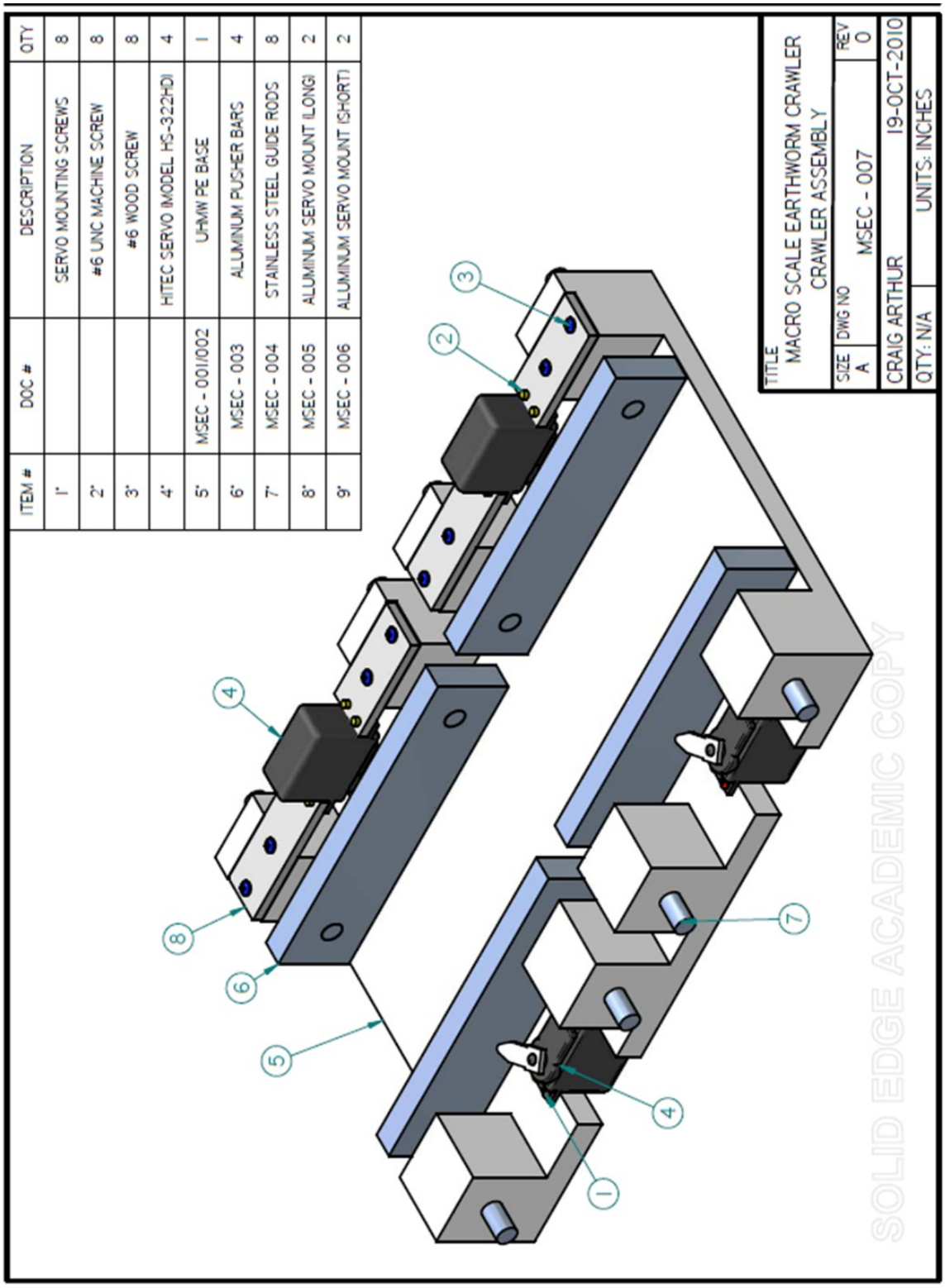

Figure B.8 - Drawing # MSEC-007

Appendix C

Four chips were designed and fabricated using the SOIMUMPS process. The first chip, IMODTMS1, was constructed to test the feasibility of the earthworm crawler at the micro-scale, and can be seen in Figure C.1. While IMODTMS1 included many different variations in shuttle geometry, due to the unfamiliarity with the SOIMUMPS process, the only shuttles that were not permanently affixed to the surface were those that sat over a trench (shown by a grey rectangle).

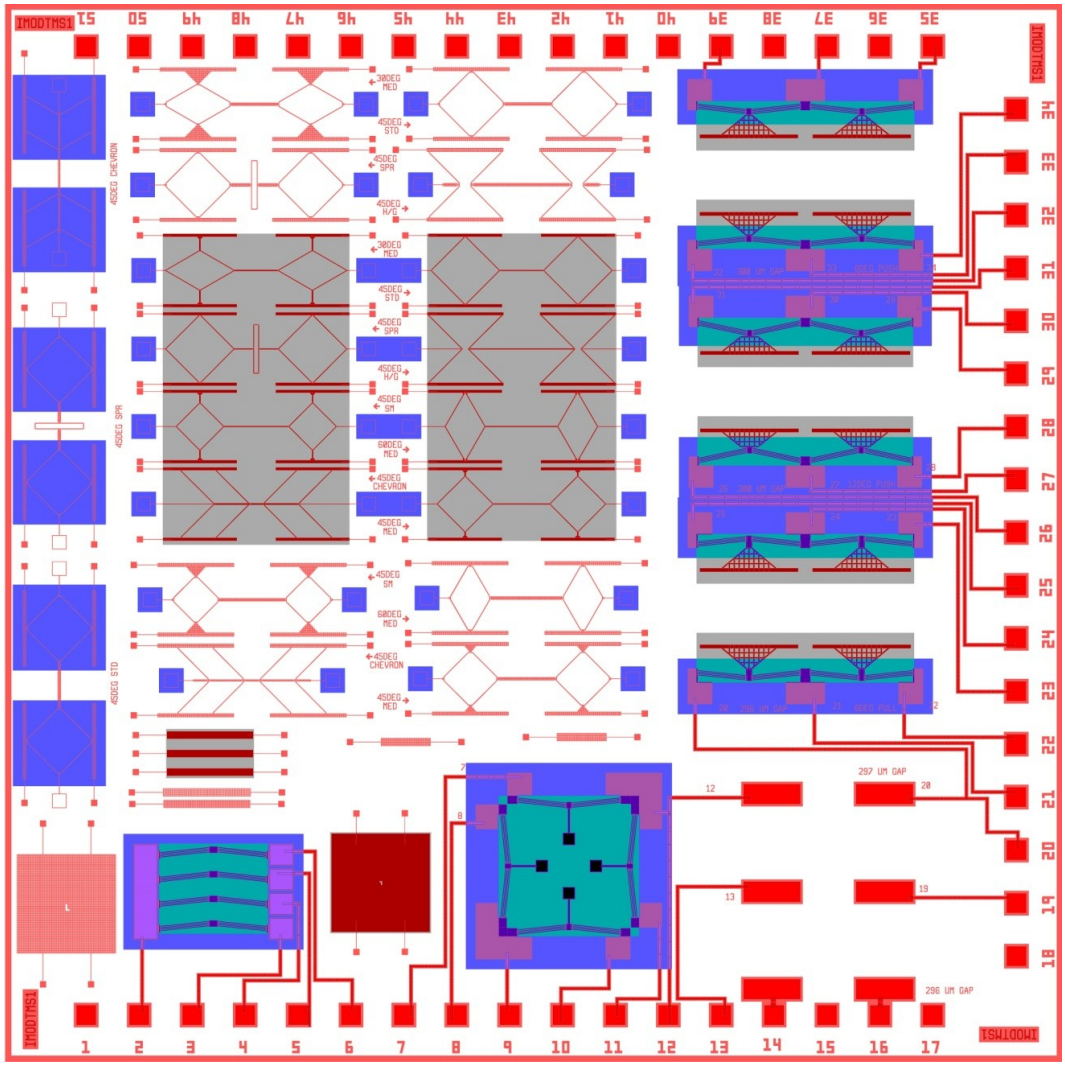

Figure C.1 – Overview of IMODTMS1 (4300 µm X 4300 µm)

Assembly of the micro-scale crawlers on this chip proved to be difficult due to the requirement of picking up a shuttle to place it in its final position. Figure C.2 shows a microscopic photograph of a typical post-assembly crawler that was tested on IMODTMS1.

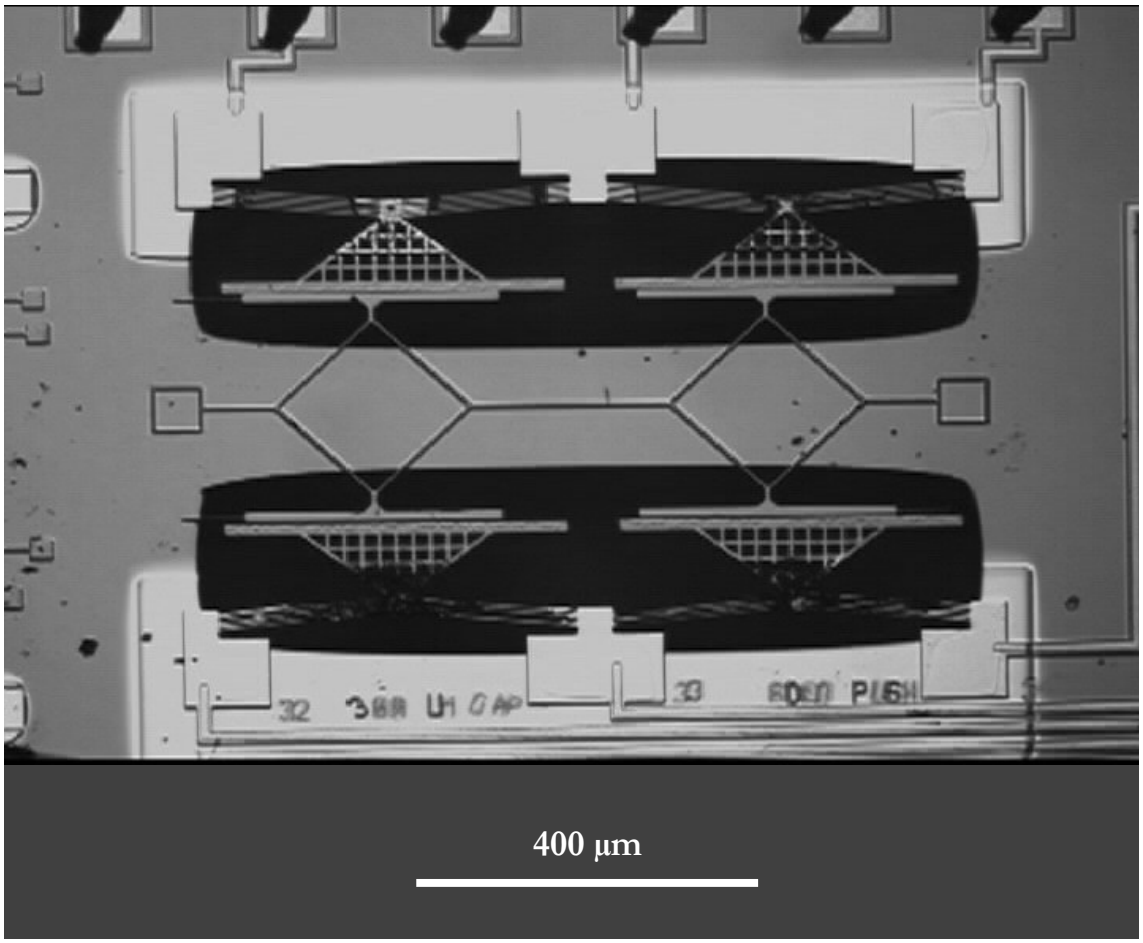

Figure C.2 – SOIMUMPs Earthworm on IMODTMS1

Once a shuttle was successfully placed between the crawlers, testing showed that the SOIMUMPs crawler would successfully move. Figure C.3 shows a graph of the motion during testing of one earthworm on IMODTMS1; the test was run with a driving voltage of 7 V, a frequency of 4 Hz, and used a burst of 50 steps in each direction. A large amount of drift was seen in the crawler's motion, the amount of which was dependant on the amount the centerline of shuttle's diamonds were offset from the centerline of the actuators; this is most likely caused by the shuttle's high stiffness in compression, in combination with the low rotational stiffness of the pushers.

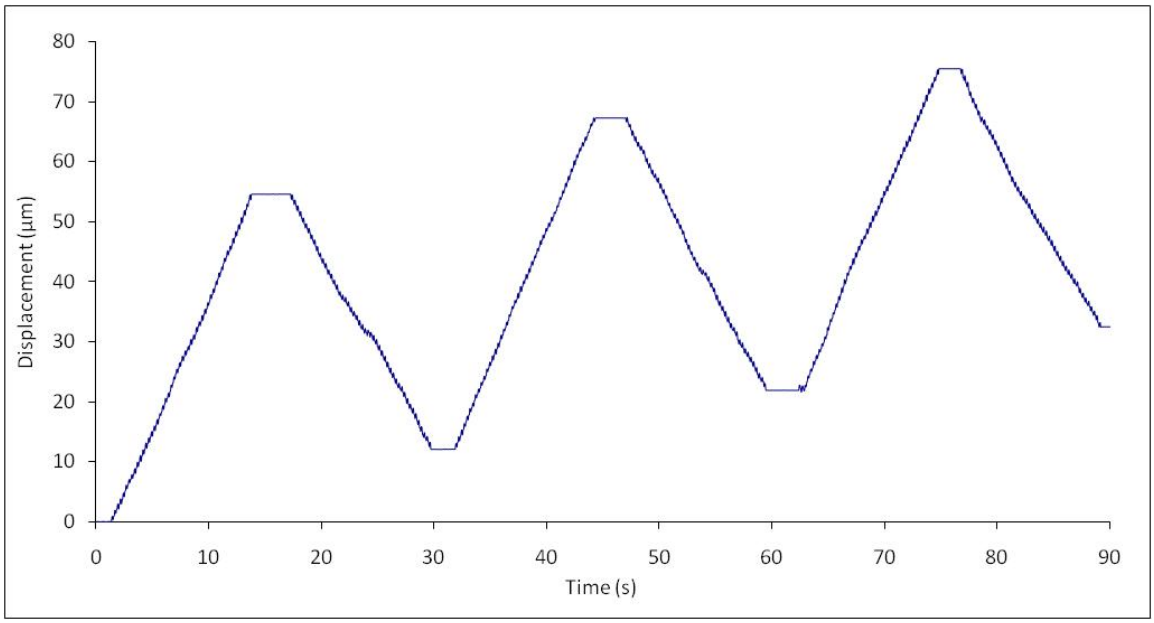

Figure C.3 – Graph of SOIMUMPs Crawler Motion

The second chip, IMODTEW2, can be seen in Figure C.4; it was designed with two crawlers that would require less assembly, which would allow testing after breaking two tethers and sliding the shuttle to its final position (similar to the assembly procedure used for the PolyMUMPs crawler). Due to a change in the process rules at the time of this chip's design, the amount of space without silicon that could be used was limited to no more than 33% of the chip's area; this severely limited what could be placed on the chip for testing, and is the reason for so much of the chip remaining empty on all future SOIMUMPs designs.

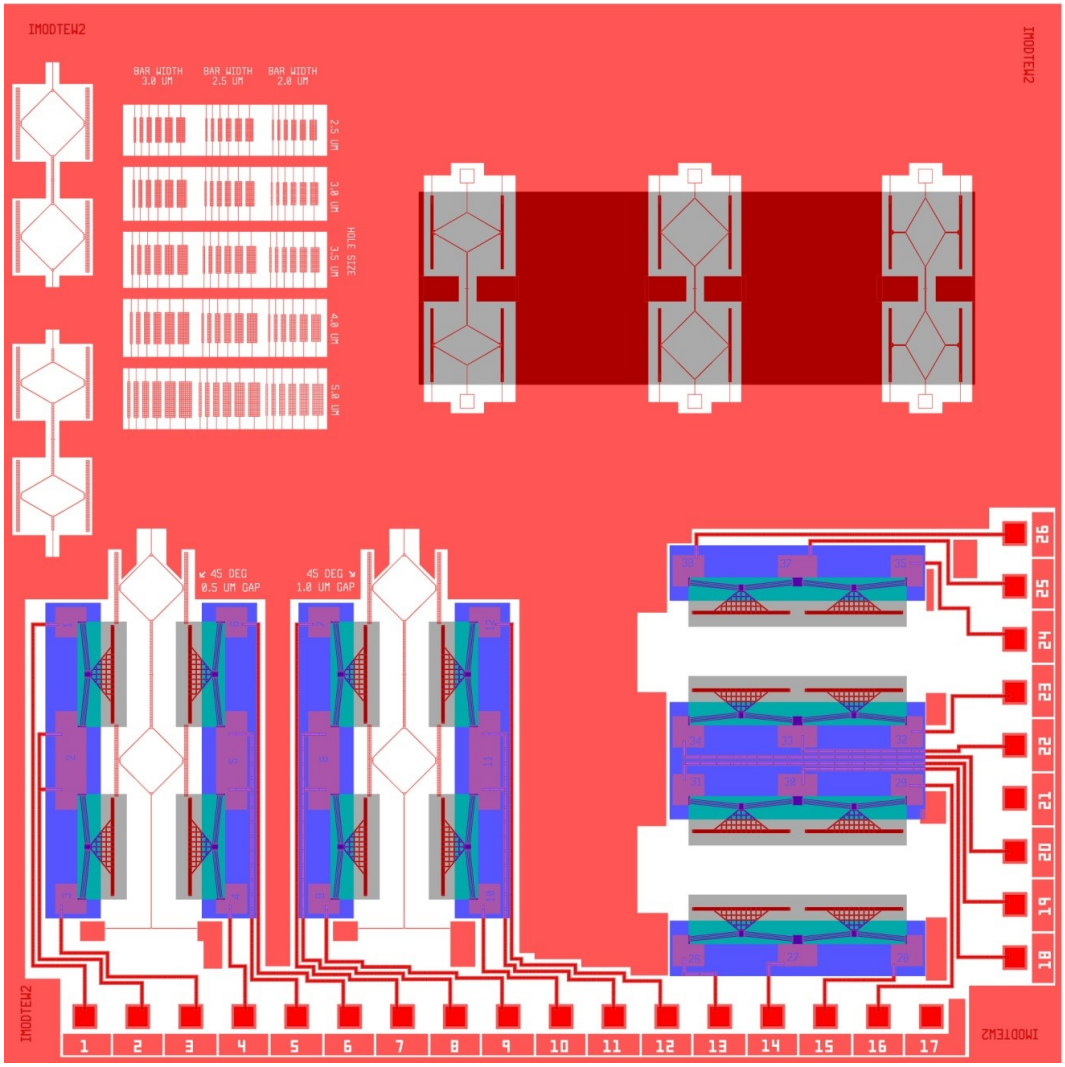

Figure C.4 – Overview of IMODTEW2 (4300 µm X 4300 µm)

Unfortunately, while the new crawler designs found on IMODTEW2 made device assembly much simpler, device testing was mostly unsuccessful. The difficulties found when testing the micro-crawlers on IMODTEW2 were mostly due to debris found in the area of the shuttles, as seen in Figure C.5. This manufacturing debris seemed to curl upwards from internal stresses, creating small 'hooks' that the shuttle would catch on and become stuck.

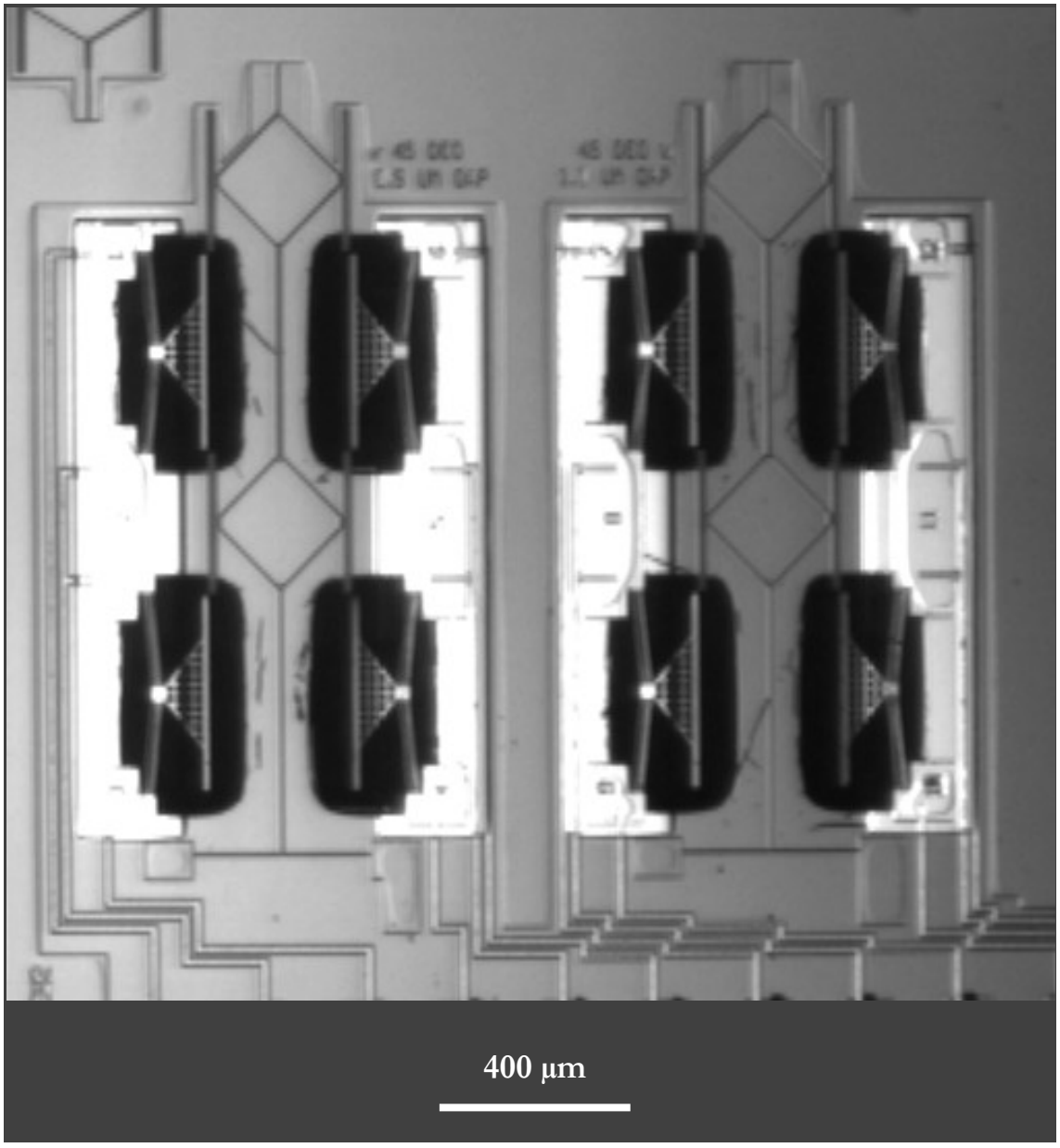

Figure C.5 - SOIMUMPs Earthworm on IMODTEW2

The third chip, IMODTEW3, had a very similar design to IMODTEW2; an image of IMODTEW3 can be seen in the Figure C.6. Unfortunately, IMODTEW3 suffered from the same debris issues as IMODTEW2, which caused testing to be unsuccessful.

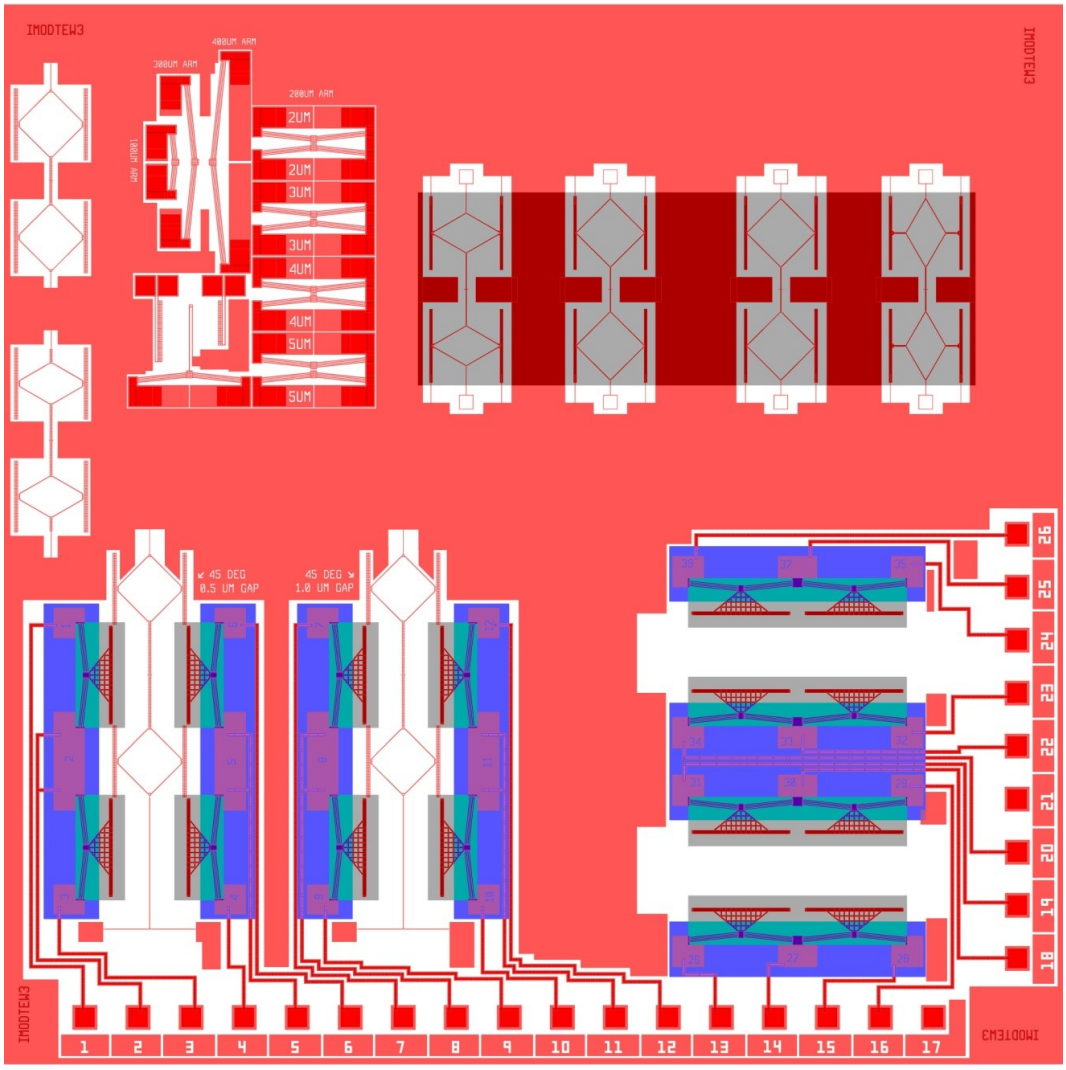

Figure C.6 - Overview of IMODTEW3 (4300 µm X 4300 µm)

An overview of the fourth chip, IMODTEW4, can be seen in Figure C.7. This chip contained two new crawler designs that were intended to eliminate the drifting issues found during the testing of previous SOIMUMPs earthworm crawlers, which can be seen on the right of the image. The new crawlers had wider pushers which would be more resistant to twisting; the version of this new crawler seen in the top-right of Figure C.7 also contained a suspension intended to eliminate the requirements for device assembly. Unfortunately, IMODTEW3 suffered from the same debris issues as previous SOIMUMPS chips.

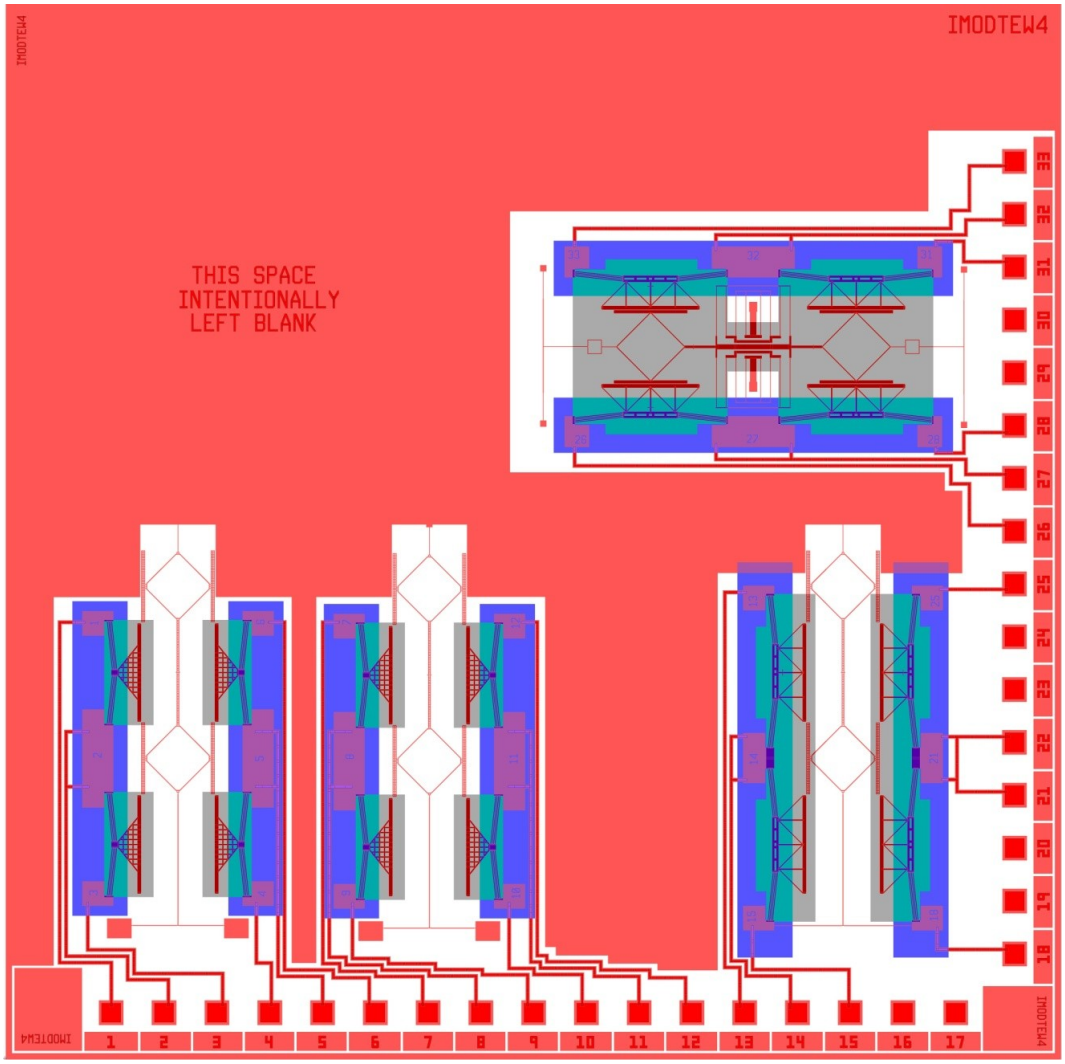

Figure C.7 - Overview of IMODTEW4 (4300 µm X 4300 µm)

References

1. **Hollar, Seth, et al.** Robot Leg Motion in a Planarized-SOI, Two-Layer Poly-Si Process. *Journal of Microelectromechanical Systems.* August 2005, Vol. 14, 4, pp. 725-740.

2. **Kim, Sang-Ho, et al.** High-Resolution Inchworm Motor Based on Electrostatic Twisting Microactuators. *Journal of Micromechanics and Microengineering.* 2005, Vol. 15, pp. 1674-1682.

3. **Kwon, Ho Nam, et al.** Design and Characterization of a Micromachined Inchworm Motor With Thermoelastic Linkage Actuators. *Sensors and Actuators A: Physical.* January 15, 2003, Vol. 103, 1-2, pp. 143-149.

4. **Tas, N R, et al.** Design, Fabrication and Testing of Laterally Driven Electrostatic Motors Employing Walking Motion and Mechanical Leverage. *Journal of Micromechanics and Microengineering.* 2003, Vol. 13, pp. N6-N15.

5. **Liu, Yung-Tien and Wang, Cheng-Wei.** A Self-Moving Precision Positioning Stage Utilizing Impact Force of Spring-Mounted Piezoelectric Actuator. *Sensors and Actuators A: Physical.* December 2002, Vol. 102, 1-2, pp. 83-92.

6. **Li, Lijie, Brown, Gordon and Uttamchandani, Deepak.** Study of Scratch Drive Actuator Force Characteristics. *Journal of Micromechanics and Microengineering.* 2002, 12, pp. 736-741.

7. **Brown, Matthew, Hubbard, Ted and Kujath, Marek.** Development of a Long-Range Untethered Frictional Microcrawler. *Journal of Micromechanics and Microengineering.* 2007, 17, pp. 1025-1033.

8. **Dai, Ching-Liang, Yen, Kaihsiang and CHang, Pei-Zen.** Applied Electrostatic Parallelogram Actuators for Microwave Switches Using the Standard CMOS Process. *Journal of Micromechanics and Microengineering.* 2001, Vol. 11, 6, pp. 697-702.

9. **Erismis, M A, et al.** A Low-Voltage Large-Displacement Large-Force Inchworm Actuator. *Journal of Microelectromechanical Systems.* December 2008, Vol. 17, 6, pp. 1294-1301.

10. **Pham, Phuc Hong, Dao, Dzung Viet and Sugiyama, Susumu.** A Micro Transportation System (MTS) With Large Movement of Containers Driven by Electrostatic Comb-Drive Actuators . *Journal of Micromechanics and Microengineering.* 2007, Vol. 17, 10.

11. **Toda, Risaku and Yang, Eui-Hyeok.** A Normally Latched, Large-Stroke, Inchworm Microactuator. *Journal of Micromechanics and Microengineering.* 2007, Vol. 17, pp. 1715-1720.

12. **Yeh, Richard, Hollar, Seth and Pister, Jristofer S J.** Single Mask, Large Force, and Large Displacement Electrostatic Linear Inchworm Motors. *Journal of Microelectromechancial Systems.* August 2002, Vol. 11, 4, pp. 330-336.

13. **de Boer, Maarten P, et al.** High-Performance Surface-Micromachined Inchworm Actuator. *The Journal of Microelectromechanical Systems.* February 2004, Vol. 13, 1, pp. 63-74.

14. *High Performance Bidirectional Electrostatic Inchworm Motor Fabricated by Trench Isolation Technology.* **Sarajlic, E, et al.** Seoul, Korea : Transducers Science and Technology (TST), 2005. 13th International Conference on Solid-State Sensors, Actuators and Microsystems.

15. **Tas, Niels, et al.** Modeling, Design and Testing of the Electrostatic Shuffle Motor. *Sensors and Actuators A.* 1998, Vol. 70, pp. 171-178.

16. **Velcro Canada.** History. *Velcro Canada.* [Online] http://www.velcro.ca/about-us/history.

17. **Peacock, Thomas and Bradley, Elizabeth.** Going With (or Against) the Flow. *Science.* June 2008, Vol. 320, 5881, pp. 1302-1303.

18. **Daimler Global.** Press Kit: The Mercedes-Benz bionic car as a concept vehicle. *Daimler Global Media Site.* [Online] [Cited: October 17, 2010.] http://media.daimler.com/dcmedia/0-921-885913-1-815003-1-0-0-0-0-1-11702-854934-0-1-0-0-0-0-0.html?TS=1284735422836.

19. **Lotus-Effect.** Fundamentals. *Lotus-Effect.* [Online] [Cited: October 07, 2010.] http://www.lotus-effekt.de/en/funktion/vorbild.php.

20. **Vogel, Steven.** *Cats' Paws and Catapults: Mechanical Worlds of Nature and People.* New York : Norton, 1999.

21. **Trivedi, Deepak, et al.** Soft Robotics: Biological Inspiration, State of the Art, and Future Research. *Applied Bionics and Biomechanics.* September 2008, Vol. 5, 3, pp. 99-117.

22. **Hinchey, Michael G, Sterritt, Roy and Rouff, Chris.** Swarms and Swarm Intelligence. *Computer.* April 2007, Vol. 40, 4, pp. 111-113.

23. **Chan, Brina, Balmforth, N J and Hosoi, A E.** Building a Better Snail: Lubrication and Adhesive Locomotion. *Physics of Fluids.* 2005, Vol. 17, 11.

24. **Chan, Brian, et al.** Mechanical Devices for Snail-like Locomotion. *Journal of Intelligent Material Systems and Structures.* February 2007, Vol. 18, 2, pp. 111-116.

25. **Shay, Byron, Hubbard, Ted and Kujath, Marek.** Planar Frictional Micro-Conveyors With Two Degrees of Freedom. *Journal of Micromechanics and Microengineering.* 2008, Vol. 18, 6.

26. **Jeong, OK Chan and Konishi, Satoshi.** The Self-Generated Peristaltic Motion of Cascaded Pneumatic Actuators for Micro Pumps . *Journal of Micromechanics and Microengineering.* 2008, Vol. 18, 8.

27. **Van Praagh, Beverly.** The biology and conservation of the giant gippsland earthworm MEGASCOLIDES AUSTRALIS mccoy, 1878. *Biology International.* 33, December 1992, Vol. 24, 12, pp. 1363-1367.

28. **National Geographic.** Common Earthworms. *National Geographic.* [Online] [Cited: August 23, 2010.] http://animals.nationalgeographic.com/animals/invertebrates/earthworm/.

29. **Darwin, Charles.** *The Formation of Vegtable Mould Through The Action of Worms, With Observations On Their Habits.* London : John Murray, 1881.

30. **Stewart, Amy.** *The Earth Moved: On the Remarkable Achievements of Earthworms.* Chapel Hill : Algonquin Books of Chapel Hill, 2004.

31. **Edwards, C. A. and Bohlen, P. J.** *Biology and Ecology of Earthworms.* 3rd. London : Chapman & Hall, 1996.

32. **Quillin, K. J.** Kinematic scaling of locomotion by hydrostatic animals: ontogeny of peristaltic crawling by the earthworm lumbricus terrestris. *Journal of Experimental Biology.* 1999, Vol. 202, 6, pp. 661-674.

33. **Bellarmine University.** Annelids. *Bellarmine University.* [Online] [Cited: September 20, 2010.] http://cas.bellarmine.edu/tietjen/images/annelids.htm.

34. **Baborowski, K.** Microfabrication of Piezoelectric MEMS. *Journal of Electroceramics.* 2004, Vol. 12, pp. 33-51.

35. **Bell, D J, et al.** MEMS Actuators and Sensors: Observations on Their Performance and Selection for Purpose. *Journal of Micromechanics and Microengineering.* 2005, 15, pp. S153-S164.

36. **Niarchos, D.** Magnetic MEMS: Key Issues and Some Applications. *Sensors and Actuators A.* 2003, 109, pp. 166-173.

37. **Ellerington, Neil, Hubbard, Ted and Kujath, Marek.** Electrokinetic Movement of Micro-Objects in Fluids Using Microelectromechanical System Electrode Arrays. *Journal of Vacuum Science and Technology A.* May 2004, Vol. 22, pp. 831-836.

38. **Bligh, Matthew, et al.** Sorting Microparticles Into Lateral Streams Using a Two-Phase Rectangular Electrokinetic Array. *Journal of Micromechanics and Microengineering.* 2008, Vol. 8, 4.

39. **Kholwadwala, Deepesh K, et al.** *MEMS Fluidic Actuator. 7,246,524* Unites States of America, July 24, 2007.

40. **Jeong, Ok Chan and Yang, Sang Sik.** Fabrication of a Thermopneumatic Microactuator With a Corrugated P + Silicon Diaphragm. *Sensors and Actuators A.* 2000, Vol. 80, pp. 62-67.

41. **Sameoto, Dan.** *Operation and Characterization of MUMPs Produced Microactuators in a Water Environment.* Mechanical Engineering, Dalhousie University. 2004. MASc Thesis.

42. *The Selection of Mechanical Actuators Based on Performance Indices.* **Huber, J E, Fleck, N A and Ashby, M F.** s.l. : The Royal Society, 1997. Proceedings: Mathamatical, Physical and Engineering Sciences. Vol. 453, pp. 2185-2205.

43. **Sameoto, Dan, Tsang, See-Ho and Parameswaran, M.** Polymer MEMS Processing for Multi-User Applications. *Sensors and Actuators A.* 2006, Vol. 134, pp. 457-464.

44. **Conway, Nicholas J, Traina, Zachary J and Kim, Sang-Gook.** A Strain Amplifying Piezoelectric MEMS Actuator. *Journal of Micromechanics and Microengineering.* 2007, Vol. 17, pp. 781-787.

45. *Shape Memory Alloy and Elastomer Composite MEMS Actuators.* **Fallon, P D, et al.** s.l. : Nano Science and Technology Institute, 2008. Nanotechnology 2008: Microsystems, Photonics, Sensors, Fluidics, Modeling, and Simulations - Technical Proceedings of the 2008 NSTI Nanotechnology Conference and Trade Show. Vol. 3. 978-1-4200-8505-1.

46. **Kahn, H, Huff, M A and Heuer, A H.** The TiNi Shape-Memory Alloy and Its Applications for MEMS. *Journal of Micromechanics and Microengineering.* 1998, Vol. 8, pp. 213-221.

47. **Hickey, Ryan, et al.** Time and Frequency Response of Two-Arm Micromachined Thermal Actuators. *Journal of Micromechanics and Microengineering.* 2003, Vol. 13, pp. 40-46.

48. **Lai, Yongjun, et al.** Force, Deflection, and Power Measurements of Toggled Microthermal Actuators. *Journal of Micromechanics and Microengineering.* 2004, Vol. 14, pp. 49-56.

49. **MEMSCAP.** SOIMUMPs Design Handbook (Revision 5.0). [Online] [Cited: September 28, 2010.] http://www.memscap.com/mumps/documents/SOIMUMPs.dr.v5.pdf.

50. —. MetalMUMPs Design Handbook (Revision 2.0). [Online] [Cited: September 27, 2010.] http://www.memscap.com/mumps/documents/MetalMUMPs.DR.2.0.pdf.

51. —. PolyMUMPs Design Handbook (Revision 11.0). [Online] [Cited: July 28, 2010.] http://www.memscap.com/mumps/documents/PolyMUMPs.DR.v11.pdf.

52. **HiTEC.** HS-322HD. *HiTEC.* [Online] [Cited: 10 01, 2010.] http://www.hitecrcd.com/products/servos/analog/standard-sport/hs-322hd.html#.

53. **d'Entremont, Rene.** *LabView Multiple Degree of Freedom Vision Control Program.* Dalhousie University. 2008. Report of Summer Work Term Project.

54. **Landry, Jason.** *Concept Validation and Feasability Study of Frictional Crawler for Novel Method of MEMS Locomotion.* Department of Mechanical Engineering, Dalhousie University. 2006. Report of Work Term Project.

55. **Sameoto, Dan, Hubbard, Ted and Kujath, Marek.** Operation of Electrothermal and Electrostatic MUMPs Microactuators Underwater. *Journal of Micromechanics and Microengineering.* 2004, Vol. 14, pp. 1359-1366.

56. **Kwon, Ho Nam, et al.** Design and Characterization of a Micromachined Inchworm Motor with Thermoelastic Linkage Actuators. *Sensors and Actuators A.* 2003, Vol. 103, pp. 143-149.

57. **Seymour, M K.** Locomotion and Coelomic Pressure in Lumbricus Terrestris L. *Journal of Experimental Biology.* 1969, Vol. 51, pp. 47-58.

58. **Kim, J and Lee, J H.** Self-Moving Cell Linear Motor Using Piezoelectric Stack Actuators. *Smart Materials and Structures.* 2005, Vol. 14, pp. 934-940.

59. *A SMA Actuated Artificial Earthworm.* **Menciassi, A, et al.** 2004. IEEE International Conference of Robotics and Automation. Vol. 4, pp. 3282-3287.